

Developing and Testing a Cost Effective Thermal Rock Bed Storage System

by

Hendrik Frederik Laubscher



*Thesis presented in partial fulfilment of the requirements for
the degree of Master of Engineering (Mechanical) in the
Faculty of Engineering at Stellenbosch University*

Supervisor: Prof. Frank Dinter

Co-supervisor: Prof. Theodor Willem von Backström

December 2017

Declaration

By submitting this thesis electronically, I declare that the entirety of the work contained therein is my own, original work, that I am the sole author thereof (save to the extent explicitly otherwise stated), that reproduction and publication thereof by Stellenbosch University will not infringe any third party rights and that I have not previously in its entirety or in part submitted it for obtaining any qualification.

Date: December 2017

Copyright © 2017 Stellenbosch University
All rights reserved.

Abstract

Developing and Testing a Cost Effective Thermal Rock Bed Storage System

H.F. Laubscher

*Department of Mechanical and Mechatronic Engineering,
University of Stellenbosch,
Private Bag X1, Matieland 7602, South Africa.*

Thesis: MEng (Mech)

December 2017

In the concentrating solar power industry, thermal energy storage is an attractive solution for storing excess energy for the periods with insufficient solar resource. Energy storage in the form of sensible heat is a mature and practical method of storing energy for later use. Current thermal energy storage technologies are expensive and alternative solutions are needed. The ultimate goal of a more cost effective thermal storage for concentrating solar power is to decrease the levelized cost of electricity. Other than the potential for capital cost reduction, it is also adding value to concentrating solar power in industry compared to other renewable technologies. With thermal energy storage, a renewable energy electricity production plant can deliver electricity on demand and support the national grid. Thermal energy storage is a well-proven concept that can meet the need for more cost effective alternatives.

The development of a novel cost effective thermal energy storage for air at 600 °C with a unique system layout is covered in this project. This novel thermal energy storage concept has potential to reduce the specific installation cost per kW_h installed. A test facility was constructed in this project for testing the feasibility of a specific concept of a packed bed thermal energy storage. The packed bed consist of a conical rock pile as a storage medium and air as the heat transfer fluid.

The test facility has a scalable design of a specific concept of a packed rock bed for thermal energy storage system. An inverted thermocline is implemented in this concept where the heat is stored at the bottom of the packed bed. A cost effective layout is presented, with each component and subsystem optimized to reduce the installation cost of the thermal energy storage test facility.

Design considerations focus on the constructability of the design, ease of assembling the structure on site and selection of the most suitable construction materials.

Operational strategies are developed to ensure that the outlet temperature, the temperature of the heat transfer fluid through the fan and also the temperature distribution through the rock pile do agree with the design specifications of the materials and the equipment used. Thermoclines defining the distribution of the temperature in the packed bed, round-the-clock cycle efficiency and characteristics of an idling storage system are investigated in this project. Commissioning and experimental testing of various operational strategies are conducted in this project in order to find a suitable operational strategy that can be used for this specific thermal energy storage that can make it feasible to use on a large scale.

The experimental results with the operation strategies implemented show that the thermal energy storage concept can be used for short term energy storage with a usable energy recovery efficiency of 60 %. The overall performance of the thermal energy storage system indicates that the concept under consideration in this project still needs to be improved to find an improved solution for a low-cost thermal energy storage that is a viable option to utilize in industry. Current challenges to improve the volume efficiency of the packed bed of rocks and the energy recovery efficiency are identified in this project for future research.

Uittreksel

Ontwikkeling en Toetsing van 'n Koste Effektiewe Termiese Rots Bed Energie Stoorstelsel

(“Developing and Testing a Cost Effective Thermal Rock Bed Storage System”)

H.F. Laubscher

*Departement Meganiese en Megatroniese Ingenieurswese,
Universiteit van Stellenbosch,
Privaatsak X1, Matieland 7602, Suid Afrika.*

Tesis: MIng (Meg)

Desember 2017

In die gekonsentreerende sonkragbedryf is 'n termiese energie stoorstelsel 'n aantreklike oplossing vir die berging van oortollige energie vir die periodes met onvoldoende sonkrag. Energie storing in die vorm van tasbare hitte is 'n gesoute en praktiese metode om energie te stoor vir latere gebruik. Huidige termiese energie stoor tegnologië is duur en alternatiewe oplossings word benodig. Die uiteindelijke doel van 'n meer koste-effektiewe termiese energie stoorstelsel vir gekonsentreerende sonkrag is om die gelykmatige koste van elektrisiteit te verminder. Behalwe die potensiaal vir kapitaalkostevermindering voeg dit ook waarde toe tot gekonsentreerende sonkrag in die industrie in vergelyking met ander hernubare tegnologieë. Met 'n termiese energie stoorstelsel kan 'n hernubare energie elektrisiteitsopwekkings aanleg op aanvraag lewer en die nasionale netwerk ondersteun. Termiese energie storing is 'n goed beproefde konsep wat die behoefte aan meer koste-effektiewe alternatiewe kan haal.

Die ontwikkeling van 'n nuwe koste-effektiewe termiese energie stoorstelsel vir lug by 600 °C met 'n unieke stelsel uitleg word in hierdie projek gedek. Hierdie nuwe termiese energie stoorstelsel konsep het die potensiaal om die spesifieke installasiekoste per kW_h te verminder. 'n Toetsfasiliteit is in hierdie projek gebou om die uitvoerbaarheid van 'n spesifieke konsep van 'n termiese energie stoorstelsel met vol bed te toets. Die gepakte bed bestaan uit 'n koniese rotsstapel as 'n opbergmedium en lug as die warmte-oordragloeistof.

Die toetsfasiliteit bestaan uit 'n skaalbare ontwerp van 'n spesifieke konsep van 'n gepakte rots bed vir 'n termiese energie stoorstelsel. 'n Omgekeerde temperatuurgradiënt word geïmplementeer in hierdie konsep waar die hitte

onder in die gepakte bed gestoor word. 'n Kostedoeltreffende uitleg word aangebied, met elke komponent en substelsel geoptimaliseer om die installasiekoste van die termiese energie stoorstelsel fasiliteit te verminder. Ontwerp oorwegings fokus op die konstruksie van die ontwerp, gemak van die samestelling van die struktuur op die terrein en die keuse van die mees geskikte konstruksiemateriaal.

Operasionele strategieë is ontwikkel om te verseker dat die uitlaat temperatuur, die temperatuur van die warmte-oordragvloeistof deur die waaier asook die temperatuurverspreiding deur die rots bed ooreenstem met die ontwerp-spesifikasies van die materiaal en die toerusting wat gebruik word. Temperatuurgradiënte wat die verdeling van die temperatuur in die gepakte bed definieer, die siklus doeltreffendheid en karaktereenskappe van 'n ledige bergingstelsel word ondersoek in hierdie projek. In hierdie projek word eksperimentele toetsing van verskeie operasionele strategieë gedoen om 'n geskikte operasionele strategie te vind wat gebruik kan word vir hierdie spesifieke termiese energie berging wat dit op groot skaal moontlik maak.

Die eksperimentele resultate verkry deur die geïmplementeerde operasionele strategieë, toon dat die termiese energie berging konsep gebruik kan word vir korttermyn energie berging met 'n bruikbare energie herwinningsdoeltreffendheid van 60%. Die algehele prestasie van die termiese energie bergingstelsel dui daarop dat die konsep wat in hierdie projek oorweeg word, nog verbeter moet word om 'n beter oplossing te vind vir 'n lae-koste termiese energie stoorstelsel wat 'n lewensvatbare opsie is om in die bedryf te gebruik. Huidige uitdagings om die volume-doeltreffendheid van die gepakte rots bed te verbeter en die doeltreffendheid van energieherwinning is in hierdie projek vir toekomstige navorsing geïdentifiseer.

Acknowledgements

I would like to thank all the people that helped me the past 2 years with execution on my project. My supervisors Prof. Frank Dinter and Prof. Theo von Backström for believing in me and trusting my engineering capabilities and intuition. STERG and the NRF for funding and Stellenbosch University for providing me the opportunity to grow as a potential engineer.

The workshop at the Mechanical Engineering Department for all their support and Cobus Zietsman and Juliun Stanfiet for all their assistance.

The list of students that helped me during construction: Brad da Silva, Emile Rossouw, Tom Moschides, Stefaans Erasmus and JC Nel.

I would like to give special thanks to Aléta Bruwer and Niël Marais for all their support and patience when I needed someone. Rudolph Botha for helping with the final editing of my dissertation and being there as a friend.

Thank you very much for my parents for making it possible for me to study and to enrich my knowledge to become an individual that can contribute to a brighter future.

I would also like to thank my late grandfather for all the skills he taught me and all the experience that he shared with me. Also for making me believe in myself and teaching me that everything is impossible until you try to do it yourself.

Dedications

"Nature's laws are the invisible government of the earth..."
Alfred A. Montapert

Contents

Declaration	ii
Abstract	iii
Uittreksel	v
Acknowledgements	vii
Dedications	viii
Contents	ix
List of Figures	xiii
List of Tables	xvi
Nomenclature	xvii
1 Introduction	1
1.1 General Introduction	1
1.1.1 Solar Resource	1
1.1.2 Thermal Energy Storage	1
1.2 Research Methodology	3
1.2.1 Research Problem Statement	3
1.2.2 Research Aims	3
1.3 Motivation and Objectives	4
1.3.1 Motivation	4
1.3.2 Objectives	4
1.4 Scope of Research	5
1.4.1 Scope Description	5
1.4.2 Experimental Design Scope	6
1.4.3 Experimental Testing Scope	6
1.4.4 Thermal Energy Storage Test Facility	7
2 Literature Review	8

2.1	History of Thermal Energy Storage Research at Stellenbosch University	8
2.1.1	SUNSPOT cycle	8
2.1.2	Experimental Work on Numerical Correlations	8
2.1.3	Porous Media CFD, Conceptual Simulation	10
2.1.4	Techno-Economic Study: Costs	11
2.2	Cost Effective Rock Bed Concepts	12
2.2.1	Concept 1	13
2.2.2	Concept 2	13
2.3	Ait Baha Facility: Morocco	14
3	Experimental Setup Development	17
3.1	Concept Generation	17
3.1.1	Conical Shape Geometry	17
3.1.2	Ducting Layout	17
3.1.3	Cost Effective System Options	20
3.1.4	Airtight Containment Structure	21
3.2	Design Specifications	21
3.2.1	Material Selection	22
3.2.2	Thermodynamics	22
3.2.3	Flow Characteristics	24
3.2.4	Pressure Drop Characteristics	24
3.3	Experimental Method Design: Measuring Equipment and Control	25
3.3.1	Mass Flow Measurement	25
3.3.2	Temperature Measurement	26
3.3.3	Simple Burner Control Design	26
3.4	Experimental Facility Layout	29
3.4.1	Containment Structure: Walls	29
3.4.2	Containment Structure: Cover	29
3.4.3	Gas Burner Description	30
3.4.4	Fan	30
3.4.5	Ducting	31
3.4.6	Air Outlet Distribution	31
3.5	Experimental Procedure and Results	31
3.5.1	Gas Burner Operation during Testing	31
3.5.2	Fan Operation during Testing	32
3.5.3	Commissioning	33
3.5.4	Full Charge — Discharge Test	33
3.5.5	Uncertainty Analysis	34
3.5.6	Experimental Results	36
3.6	Observations during Testing	39
4	Construction of Experimental TES Facility	40
4.1	Methodology	40

4.2	Installation Progress Record	41
4.3	Subsystem Installation	42
4.3.1	Insulation and Base	42
4.3.2	Air Distribution Box	43
4.3.3	Hot Air Ducting	44
4.3.4	Wall Installation	44
4.3.5	Stacking of Rocks	44
4.3.6	Cover and Accumulator Installation	45
4.4	Safety During Construction	46
4.5	Safety During Operation	46
5	Numerical Simulation of TES Performance	48
5.1	Introduction	48
5.2	Heat Transfer	48
5.2.1	Governing Equations For Heat Transfer	50
5.2.2	Dimensionless Parameters	51
5.2.3	Biot Number Description	52
5.2.4	Energy Calculation	52
5.2.5	Energy Efficiency Definition	54
5.3	Pressure Drop through Porous Media	55
5.3.1	Velocity and Density Dependence on Pressure Drop	56
5.3.2	Pressure Drop Profile Over Test Section	57
5.4	Numerical Simulation Results	58
5.4.1	Heat Transfer Dimensionless Parameters	58
5.4.2	Temperature Distribution	60
5.4.3	Simulation Results Summary	60
6	Results and Discussion	63
6.1	Results	63
6.1.1	HTF Pumping Power	63
6.1.2	Thermal Energy Distribution	64
6.1.3	Mass Flow and Continuity	65
6.2	Energy Recovery	66
6.2.1	Simulation and Experimental Results Comparison	66
6.2.2	Environmental Energy Losses	66
6.2.3	Volume Efficiency	67
6.3	System Performance Observations	68
6.3.1	Idling Characteristics	68
6.3.2	Cost Effectiveness	68
7	Conclusion	70
7.1	Conclusions	70
7.2	Future Recommendations	71
7.3	Proposed Future Design Changes	72

Appendices	73
A Official documents	74
B Material Specification	76
B.1 Roof Tarpaulin	76
B.2 Tarpaulin Cover Drawing	77
B.3 Ducting Stainless Steel Specification	78
B.4 High Temperature Gasket Material	80
B.5 Wall Sections	81
C Ducting Pressure Drop Calculations	82
D Equipment	86
D.1 Burner Combustion Chamber Sizing	86
D.2 Burner Heating Capacity	87
D.3 Burner Control Diagram	88
D.4 Flame Containing Nozzle Design	89
D.5 Fan Specifications	90
E Pressure Transducer Calibration	92
E.1 Calibration Procedure	92
E.2 Calibration Results	92
F Computational Fluid Dynamics	94
F.1 Introduction to Numerical Analysis	94
F.2 Process of Numerical Simulation	95
F.2.1 Geometry Definition	95
F.2.2 Mesh	97
F.2.3 Solution Setup	97
F.2.4 Cell Zone Conditions	98
F.2.5 Boundary Conditions	98
F.3 Porous Media Models	99
F.3.1 Built-in Porous Model	99
F.3.2 Porous Media Geometry	99
F.4 CFD Results	99
G Experimental Facility Capital Expenditure	101
List of References	103

List of Figures

1.1	DNI resource map of Africa and the Middle East	2
1.2	Experimental test facility during the commissioning test	7
2.1	SUNSPOT cycle system diagram	9
2.2	Large scale CFD simulation results for a 150 m footprint diameter, showing the temperature distribution after 8 hours of charging . . .	11
2.3	Rock reconstruction using automatic clump generator in CAD . . .	11
2.4	Rock bed TES concepts cost comparison	12
2.5	Packed bed TES concept showing the air flow ducting and hot region	14
2.6	Inverted thermal energy storage concept	14
2.7	Schematic layout of the pilot-scale thermal storage configuration and experimental setup	15
2.8	Ait Baha CSP pilot plant photos in the Agadir region, Morocco . .	15
3.1	Flow diagram of the system when operating in charging mode . . .	18
3.2	Flow diagram of the system when operating in discharging mode . .	19
3.3	Hot ducting drawing layout	19
3.4	Base insulation beneath the thermal storage facility under construction	20
3.5	Airtight tarpaulin cover deflated with no flow present, and inflated during charging mode	21
3.6	Thermocouple placement frame and air distribution box on the thermal energy storage base	27
3.7	Placement of thermocouples on the stainless steel pipe frame	27
3.8	Cover-to-wall flange connection details	29
3.9	Burner installation in the air flow line	30
3.10	Inner view of the air outlet distribution structure	32
3.11	Thermal image taken during commissioning test while in idling mode	35
3.12	Radial air temperature comparison between measured thermoclines for the West-plane and South-plane at a charged state during the commissioning test	36
3.13	Thermal image taken during commissioning test while in idling mode, 8 hours after end of charging cycle	38

3.14	Thermal image taken during commissioning test while charging at 642 °C	38
3.15	Temperature distribution of the system in idling mode	39
4.1	Rock bed Construction Progress Photos	41
4.2	Rock bed heating system construction progress photos	42
4.3	Operating TES in a charging state	43
4.4	Air distribution box and insulated ducting	43
4.5	Installation of the walls in trenches	44
4.6	Stacking of the rocks by using a conveyor belt and a small excavator	45
4.7	Accumulator box connected to the cover	45
5.1	Diagram of the computational domain for the 1 D numerical model showing half the section of a cone	49
5.2	Diagram of the computational domain for the 1 D numerical model showing half the section of the hemisphere	50
5.3	Energy distribution graph of energy stored in the rock bed over time	55
5.4	Flow diagram of the packed bed layout showing the flow direction of the fluid and the geometry of the rock bed	57
5.5	Radial pressure drop plotted for each segment at a charged state	58
5.6	Surface heat transfer coefficient	59
5.7	Nusselt numbers for the start and end of the charging cycle	59
5.8	Air and rock temperatures through the rock bed	60
6.1	Radial air temperature; comparison between simulated and measured thermocline for the West-plane and South-plane at a charged state	64
6.2	Temperature distribution contour plots for comparison of CFD and experimental results	65
6.3	Temperature distribution of the system in idling mode	68
B.1	Tarpaulin cover material specifications	76
B.2	Tarpaulin cover drawing indicating the position of the ventilation holes	77
B.3	Stainless steel 409 engineering specifications	78
B.4	Stainless steel 409 engineering specifications, continued	79
B.5	Ceramic fibre board specifications	80
B.6	CAD drawing of a sheet metal wall section	81
D.1	Combustion chamber sizing specification sheet	86
D.2	Riello burner technical data	87
D.3	Burner control circuit diagram	88
D.4	Air cooled flame containing nozzle layout	89
D.5	Fan specification sheet with rated values	90
D.6	Fan performance curve	91

E.1	Name plate of the Endress and Hauser pressure transducer	93
E.2	Calibration curve showing the pressure for the corresponding mADC reading	93
F.1	Dimensions of the porous medium geometry	95
F.2	Geometry of the rock conical rock pile with a cut-out to expose the detail	96
F.3	Computational domain section showing a 30 vector of the real geometry	96
F.4	Cross-sectional plane showing meshing in the computational domain	97
F.5	Temperature distribution of the simulated TES after 4.5 hours of charging (Results reworked in Matlab to have same colour contour scale as the measured temperature distribution results)	100
F.6	Temperature distribution of CFD simulated TES results after 4.5 hours of charging	100

List of Tables

3.1	Design parameters of the prototype, rated values	23
3.2	Mechanical properties of steels at elevated temperatures	23
3.3	Rated air flow parameters summary	24
3.4	Rated pressure drop over various flow sections in the system	25
3.5	Design parameters of the prototype, rated values and commissioning values	33
3.6	Storage material volume efficiency	35
3.7	Thermal performance and efficiencies of the TES calculated from experimental measurements	37
3.8	Pressure performance characteristics of the fan during experimental testing	39
5.1	Summary of simulation results for the commissioning test	61
5.2	Summary of simulation results for a full charge-discharge test	62
6.1	Pressure performance characteristics of the fan during experimental testing	64
6.2	Results summary of the simulation and experimental results for full charge-discharge test	67
6.3	Storage material volume efficiency	69
F.1	Physical properties of packed bed of rocks	95
F.2	Mesh statistics for simulation	97
G.1	Capital asset items	102

Nomenclature

Constants

g 9.7962 [m/s²]

Variables

A_{bm} Bellmouth throat area [m²]
 A_{cs} Rock bed computational domain cross-sectional area . . [m²]
 A_{cone} Cone area [m²]
 A_{sph} Hemispherical area [m²]
 C_d Discharge coefficient [–]
 $c_{\text{p,r}}$ Rock heat capacity [J/kg·K]
 $c_{\text{p,a}}$ Air heat capacity [J/kg·K]
 D_v Volume equivalent spherical diameter [m]
 D Ducting diameter [m]
 D_{bm} Ducting diameter for bellmouth [m]
 d_l Change in length, thermal expansion [m]
 E_{in} Energy input [kWh_{th}]
 E_{out} Energy output [kWh_{th}]
 E_{stored} Energy stored in the rocks [kWh_{th}]
 e_k Elemental uncertainty factor [%]
 f_v Apparent friction factor (for D_v) [–]
 f Darcy friction factor for internal pipe pressure losses . . [–]
 G Mass flux of air [kg/m²·s]
 H Cone height [m]
 h Enthalpy [J/kg·K]
 h_s Surface to air heat transfer coefficient [W/m²·K]
 h_v Volumetric heat transfer coefficient [W/m³·K]
 k_r Particle (rock) thermal conductivity [W/m·K]
 k_a Fluid (air) thermal conductivity [W/m·K]
 L Length of the packed bed [m]

L_0	Original length, thermal expansion	[m]
\dot{m}	Air mass flow rate	[kg/s]
Nu_v	Nusselt number (for D_v)	[-]
NTU	Number of transfer units	[-]
P	Calibration pressure	[Pa]
Δp	Pressure drop per segment	[Pa]
ΔP	Pressure drop over rock bed (total)	[Pa]
ΔP_{bm}	Pressure difference at bellmouth throat	[Pa]
Pr	Air Prandtl number	[-]
\dot{Q}	Heat rate	[kW _{th}]
r	Cone radius	[m]
Re_{pv}	Particle Reynolds number (for D_v)	[-]
Re_v	Duct Reynolds number (for D_v)	[-]
Re	General Reynolds number	[-]
R	Coefficient of Determination	[-]
S	Average rock size	[m]
T_{amb}	Ambient (air) temperature	[°C]
T_f	Fluid (air) temperature	[°C]
T_p	Particle (rock) temperature	[°C]
ΔT	General temperature difference	[°C]
Δt	Time step period	[s]
v_s	Superficial velocity	[m/s]
x	Rock bed radial distance	[m]
Δx	Discrete segment length	[m]
y	Output signal	[mADC]

Subscripts

a	Air
bm	Bellmouth
cs	Cross-sectional
f	Fluid
i	Iteration index
k	Elemental error factor index
p	Particle
r	Rock
sr	Surface roughness
v	Volumetric

sph Spherical
cone Cone

Greek Alphabet

α_s	Thermal expansion coefficient stainless steel 409	$[\mu\text{m}/\text{m} \cdot \text{K}]$
β	diameter ratio	$[-]$
ε	Rock void fraction	$[-]$
ε_{sr}	Surface roughness for use in Colebrook equation	$[-]$
η	E-NTU constant	$[-]$
η_{ht}	Heat transfer efficiency	$[-]$
$\eta_{\text{th,usable}}$	Usable heat recovery efficiency	$[-]$
$\eta_{\text{th,total}}$	Total heat recovery efficiency	$[-]$
θ	Natural angle of repose	$[\circ]$
μ	Viscosity of air	$[\text{kg}/\text{m}\cdot\text{s}]$
ρ_a	Air density	$[\text{kg}/\text{m}^3]$
ρ_r	Rock density	$[\text{kg}/\text{m}^3]$
τ	Time constant	$[\text{s}]$

Glossary

Control mass: Constant rock mass in the porous region
Control volume: The fluid volume within the porous region
Control porous volume: The bulk volume of the fluid and the solid
Inverted thermocline: Hot region located at the bottom
Equivalent spherical diameter: Diameter of a sphere which has a corresponding volume to the volume of a non-uniform particle
Volume efficiency: Amount of rocks in the TES above 50°C at a charged state

Abbreviations

CSP Concentrating Solar Power
LCOE Levelized Cost Of Electricity
HTF Heat Transfer Fluid
TES Thermal Energy Storage
DNI Direct Normal Irradiation

Chapter 1

Introduction

1.1 General Introduction

Energy demand in the world keeps growing as the human population grows. With production of food and consumable products to meet the demand of a growing population, industry needs to keep up with delivering to the need. An increase in industry, a larger number of households and more production lines require more energy in the form of electricity and process heat to thrive. Renewable energy offers a number of solutions to the electricity supply issue, but many renewable energies generate electricity intermittently. The concentrated solar power (CSP) field of renewable energy opens up the possibility for storing energy directly in the form of heat. The capability of storing thermal energy gained from renewable resources, such as the sun, adds value and production flexibility to CSP that other renewable energy technologies cannot offer at an affordable rate at the moment.

1.1.1 Solar Resource

The abundant solar energy in the world is currently under-utilized in most developing countries in the world. In the Southern parts of Africa, the solar resource has great potential and the high direct normal irradiation (DNI) figures show a viable option for concentrated solar power (CSP) (Solargis, 2013). Southern Africa has the best DNI in Africa and this is a good reason why there is great potential in CSP in this region. Refer to Figure 1.1 for an illustration of the DNI distribution over Africa.

1.1.2 Thermal Energy Storage

Thermal energy storage (TES) is the main advantage that distinguishes CSP from other forms of renewable energy. Storing of the energy in the form of sensible- or latent heat enables the plant operator to produce electricity on demand. The initial installation cost for a CSP plant is currently higher than

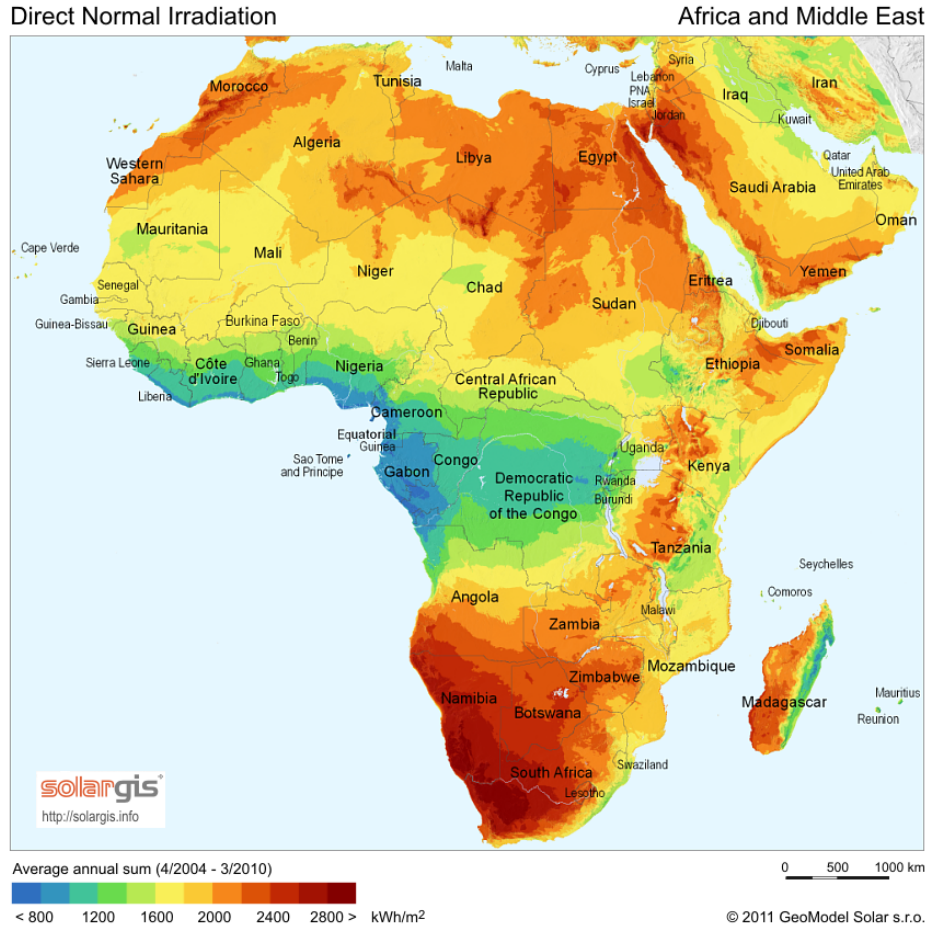


Figure 1.1: DNI resource map of Africa and the Middle East (Solargis, 2011)

other alternative renewable energy sources however, the value of producing electricity on demand must be considered in comparing the value of different renewable energies. The period of peak solar resource and the time of peak electricity demand do not coincide in the case of the South African national power grid. Volatility in the demand for electricity requires the producer to be able to produce electricity when there is a peak in demand. Cheaper alternative options for TES at high temperature (600 °C) are being investigated to find an alternative material type, heat transfer fluid and system layout that would be more cost effective than the existing state-of-the-art molten salt TES used in the CSP industry (Kolb *et al.*, 2011).

Various materials for storing thermal energy in the form of sensible heat at high temperatures have been considered including molten salt, concrete and steam. Alternative storage of thermal energy in concrete and in saturated steam is also used in the minority in industry today. The state-of-the-art two tank molten salt system is widely used in the CSP industry today (Kolb *et al.*, 2011). The packed bed concept has proved to be successful on a conceptual level as well as in experimental testing. A packed bed of rocks as a storage

medium and air as a heat transfer fluid has shown great potential in the field of high temperature TES (Allen *et al.*, 2016).

1.2 Research Methodology

1.2.1 Research Problem Statement

Thermal energy storage is the key capability that distinguishes CSP from other renewable energy technologies. The need for cost effective energy storage in general is an issue that is investigated in other forms apart from TES (DiOrion *et al.*, 2015).

Development of a cost effective TES system is the research problem that needs to be addressed. In order to achieve a cost effective TES, the applicable aspects that make TES expensive must be addressed like insulation, cost of construction and cost of the storage medium. Developing a system layout with an optimized design for each sub system, ensures a cost effective design.

A TES system has potential to decrease the cost only if it has a high enough useful energy recovery efficiency. The energy efficiency can be defined in two main ways, a) total energy input compared with total energy output and b) exergy efficiency. Exergy efficiency is the most applicable definition of the efficiency of this particular TES concept prototype, as it describes the useful energy that is recovered. Exergy is a thermodynamic term that describes the useful energy recoverable in the system. The usable recoverable energy definition is best described in literature: "*Exergy is a property and is associated with the state of the system and the environment. A system that is in equilibrium with its surroundings has zero exergy and is said to be at the dead state. The exergy of heat supplied by thermal energy reservoirs is equivalent to the work output of a Carnot heat engine operating between the reservoir and the environment.*" (Cengel and Boles, 2011).

1.2.2 Research Aims

The main research aim for this project is the experimental testing and validation of the feasibility for a prototype test facility for TES. Research questions include the following: (i) Can an energy recovery of 65% be achieved? (ii) Would the inverted thermocline be sufficiently stable to efficiently store thermal energy in excess of 24 hours (iii) Is an uninsulated thermal energy storage system feasible for utility scale energy storage? Specific objectives are described in depth and is covered in section 1.3.

Commissioning of the test facility to produce experimental results together with numerical simulation of the same concept will be discussed and a conclusion on the feasibility of the concept under investigation will be the outcome of this research project. The numerical model developed in parallel with the

test facility will be validated according to the experimental results to have a model that can represent the system performance of this specific geometry of a packed rock bed. Consequently, this numerical model can be used to simulate a large scale (utility scale) TES of the same geometry in future studies. Ideas for an improved design of this concept can be proposed in the end of this project, depending on how successful the concept under investigation proves to be.

1.3 Motivation and Objectives

1.3.1 Motivation

- Thermal energy storage currently used in industry is effective but is also expensive and can contribute up to 11 % of the levelized cost of electricity (LCOE) of a CSP plant (Kolb *et al.*, 2011). Thermal energy storage is thus an integral factor in the drive for low-cost CSP.
- TES with a packed bed of rocks could be cost effective and well suited to the environment in South Africa, because of the availability of the suitable rock type. Dolerite, a rock suitable for thermal storage at high temperatures, is abundantly available in the Northern Cape province of South Africa, which coincides with one of the highest solar resource spots in South Africa (Allen, 2014). This is an advantage, because long distance transportation costs of the storage medium could be reduced or eliminated if the storage facility is located close to the source of the rocks.
- The Stellenbosch UNiversity Solar POver and Thermodynamic (SUNSPOT) cycle that is described in more detail in Chapter 2 consists of various components of which one is the TES. A packed bed TES system for this application is designed to be heated by air, thus an effective air receiver is a component that is integral to the operation of a packed rock bed TES in the SUNSPOT cycle. The concept developed in this project was proposed by Gauché and Louw (2014) while they were active at the Solar Thermal Energy Research Group (STERG).

1.3.2 Objectives

The main research objective is to develop a TES that is more cost effective than the existing TES used in industry today. Design, construction and testing of a TES test facility describe this research objective. This objective can be divided into a few components that describe how the objective can be reached.

1. Development of a TES without thermal insulation on the bulk storage material. It should reach a charging temperature of up to 600 °C. Ther-

mal energy storage without insulation will eliminate the high cost of thermal insulation. A system layout should be designed and constructed which stores the heat in the center of the packed bed to maintain a cool temperature on the outside of the packed bed.

2. Development of a low-cost containment for the TES that does not support or constrict the bulk packed bed which reduces the effect of ratcheting in the packed bed. A containment which is airtight should be designed and constructed to contain the packed bed.
3. Numerical simulation of the overall TES performance with the focus on round-the-clock cycle efficiency, temperature distribution, and pressure drop over the porous medium. The simulated performance parameters should be compared with the experimental results for validation of the numerical model.
4. Experimental measurement of the thermal losses to the immediate environment, the volume efficiency of the rocks in the TES, and calculation of the afore mentioned numerically simulated parameters.
5. Characterization of the storage capability for an idling TES over an extended period of time (24-hour time period). Temperature distribution through the packed bed of rocks for the idling period and identification of the stability of the thermocline in a charged rock bed are the results which should physically be measured.

1.4 Scope of Research

1.4.1 Scope Description

The scope of this research is defined by the development and experimental testing of a cost effective thermal rock bed storage system. Design, construction and experimental testing of a prototype TES facility defines the practical segment of the scope of this research. All the detail design, managing and supervising the purchasing, construction and logistics of the built facility was executed by Mr H.F. Laubscher. The theoretical part of this research project involves the development of a 1 D numerical model. The numerical model covers the fundamentals of heat transfer in a porous medium (Allen *et al.*, 2015). Simplified computational fluid dynamics (CFD) modelling in a porous medium of this specific packed bed geometry was only used as a design tool and was not validated by the experimental results or the numerical results. Determining if the concept under investigation is feasible to implement on a large scale in the industry will be the greater outcome of this research project.

1.4.2 Experimental Design Scope

An initial engineering design was proposed based on the available materials to construct the test facility. An iterative design process was followed to find the suitable materials and equipment for the construction. Locally available materials and equipment were used as far as practically possible to minimize the cost. Unique component costs are greatly dependent on manufacturability. Therefore, the system design is simplified to reduce the number of specialized components and specialized components have been simplified for manufacturing. On-site assembly has also been considered throughout the design phase.

For engineering specification of the built facility, a one dimensional (1D) numerical model was developed to identify some key design specifications of the TES prototype. The charging time, temperature distribution, pressure drop over the porous rock bed, flow characterisation and an approximate thermocline gradient are identified with the use of the 1D numerical model. The limitation of the 1D model is that it only provides a solution in one dimension and the effects of buoyancy cannot be fully incorporated in the calculation of the flow characterisation. The varying cross-sectional area in the rock bed can be accounted for in the 1D model and be incorporated in the heat transfer calculations only in one dimension. The process followed to develop the numerical model is covered in Chapter 5.

Simplified CFD of the packed bed was done to obtain a prediction of the temperature distribution in 3D. This elementary CFD model was only used as a design tool in the specification of the TES system. The effect of gravity and temperature dependent density can be activated in the CFD model to observe the effect of buoyancy when the TES is in an idling mode. A preliminary prediction of the heat distribution in 3D was used to specify the cover material and the area of insulation at the base of the TES. The effectiveness of any long term thermal energy storage requires that the TES system do not lose significant amounts of energy to the immediate environment when in idle mode.

1.4.3 Experimental Testing Scope

Conducting experiments on the built TES facility was required to produce experimental results. Operational strategies were designed based on the small scale high temperature TES facility that does exist at Stellenbosch University. Experimental procedures and the system operation of the prototype built during this project is similar to the existing test facility experimental procedures (Allen, 2014). Identification of different strategies to optimize the energy recovery from the TES and to store thermal energy for long periods were covered in this project.

A test facility which replicates practical operational conditions was required to perform tests to mimic how the TES would perform in an industry-like environment. The test facility constructed in this project was built with mi-



Figure 1.2: Experimental test facility during the commissioning test

nimum alterations to the natural environment. No major soil preparation was done to accommodate the bulk material of the packed rock bed. The test facility was built on the existing soil profile that is not level. A cost effective design incorporates the natural condition of the soil profile to minimize the preparation costs.

1.4.4 Thermal Energy Storage Test Facility

Design and construction of an experimental facility which is a scaled down version of what could potentially be used in industry, yet is still large compared to experimental test facilities in the academic environment, was constructed for this project. A photo of the test facility under construction can be observed in Figure 1.2. Testing and evaluating the feasibility of an experimental scale of this concept on a system level are part of this study. Commissioning of the experimental test facility as well as conducting various experimental tests in order to gather experimental data on the performance of the system will give an indication of the feasibility of this system layout. Lessons learnt from the experimental data generated by use of the prototype TES test facility can be used as a guideline for future research in this field of study. The feasibility of a utility scale system of this particular concept (conical geometry) must still be validated on a system level and is not covered in the scope of this research.

Chapter 2

Literature Review

2.1 History of Thermal Energy Storage Research at Stellenbosch University

2.1.1 SUNSPOT cycle

Applicability of rock bed TES with air as a heat transfer fluid originates from the initial novel concept proposed by the late Professor Kröger. The SUNSPOT cycle was first proposed in 2008 and consists of an air cycle where the packed rock bed TES fits in (Kröger, 2012). Research in renewable energy has been conducted at Stellenbosch University in recent years with a larger focus on solar thermal energy. The main respective components of this proposed concept have been developed in parallel at Stellenbosch University with the goal to develop a locally developed system that is cost effective and also environmentally friendly. A layout of the SUNSPOT cycle is illustrated in Figure 2.1. The main components of the cycle can be identified and the location of the TES in the system is indicated with 'Storage Rock Bed'.

The main goal of this project is to achieve a simple engineering solution which is sustainable and cheaper than the existing state-of-the-art methods of TES that are used in the industry today. By making use of a simple, non-complex design, the technical feasibility of the proposed concepts must be determined.

2.1.2 Experimental Work on Numerical Correlations

In a study done on the design considerations for a large scale TES method, there are a few technical aspects which were highlighted for future research on the topic of high temperature thermal storage in power plants (Allen *et al.*, 2014). Molten salt storage that is currently used in a TES can reach temperatures up to 565 °C in tower receivers operating with steam. The temperature limitation is based on the containment structure and molten salt material

2.1. HISTORY OF THERMAL ENERGY STORAGE RESEARCH AT STELLENBOSCH UNIVERSITY

9

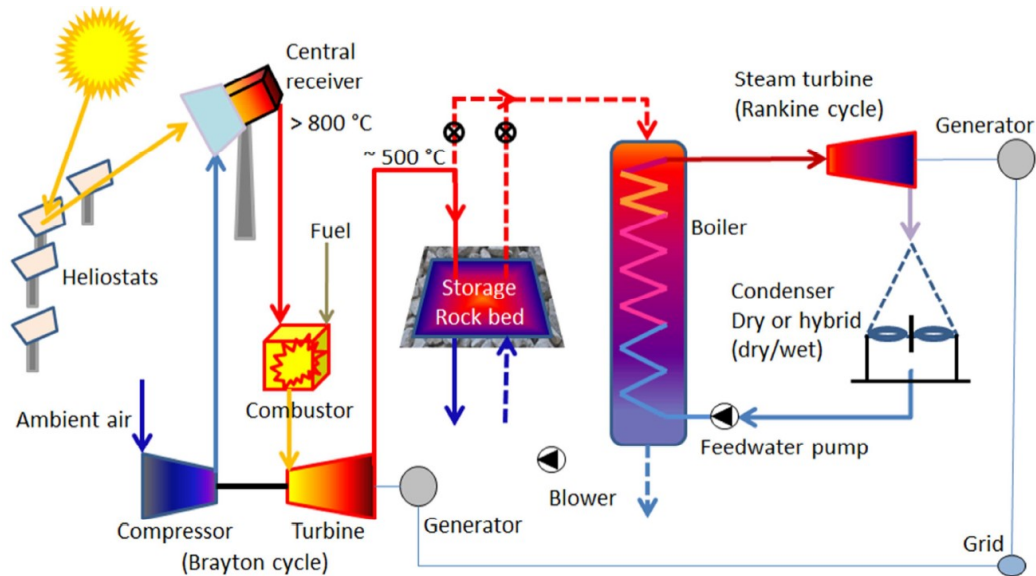


Figure 2.1: SUNSPOT cycle system diagram (Kröger, 2012) (Diagram by Allen, 2011)

compatibility at high temperatures (Bradshaw and Goods, 2009). This is already a fairly high temperature for thermal storage, but with the central receiver technology, higher temperatures can be reached which enables thermal storage at elevated temperatures between $600\text{ }^{\circ}\text{C}$ and $800\text{ }^{\circ}\text{C}$ (Allen, 2014). Higher high-temperature limits contribute positively to the overall efficiency of the power generation cycle according to the Chambadal-Novikov equation (Bejan, 1996).

Flow characterisation of the heated air flowing through a packed bed of rocks has been done and tested experimentally at the University of Stellenbosch. In the experiments conducted, the pressure drop over a packed bed was characterized by a variety of shapes and pack formations. Equations describing the pressure drop for the different void fractions and particle sizes have been developed in order to obtain the required pumping power of the air flow to overcome the frictional losses (Allen *et al.*, 2013).

Experimental simulation of the packed bed storage below $100\text{ }^{\circ}\text{C}$ suggests that the heat transfer characteristics may be predicted with existing correlations. Data on the heat transfer characteristics for a packed bed with an inverted thermocline at high temperatures (up to $600\text{ }^{\circ}\text{C}$) is a big unknown factor that must be investigated. An overall heat transfer coefficient at a certain design point for the storage system is necessary to make a feasible decision in designing a large scale thermal storage system. High temperature heat transfer and pressure drop correlations for a packed rock bed has been developed and is presented by Allen *et al.* (2015). The rock bed configuration investigated by Allen (2014), on which the high temperature correlations are based, is a small scale test facility at Stellenbosch University where the heat is stored in the top

part of the packed bed.

With the thermal expansion and contraction of the packed bed of rocks, a phenomenon called ratcheting, described below, may cause problems by fracturing the rocks. By designing the thermal energy storage for a life time of approximately 40 years, failure or breakdown of the storage medium can become an issue and design should accommodate easy replacement of the packed rock bed thermal storage material. An alternative would be to design the packed bed to prevent the potential fracturing of the rocks, by placing a constraint on the maximum height of the bed, hereby reducing the pressure on the rocks in its lower regions. Adding some sand on the base of the packed bed can also help to absorb and distribute the dynamic loading induced by the thermal cycling. The movement due to ratcheting of the rocks while experiencing thermal cycling can also put additional stress on the containment structure of the rock pile. A system design with the pile of rocks having an unconstrained free surface can contribute to a low-cost containment structure and also minimize the stress experienced by the wall that does come into contact with the rocks.

In previous studies, the most suitable rocks for thermal energy storage were identified as metamorphic and igneous rocks. Dolerite, a metamorphic rock type, was identified to have the best thermal properties to use in this thermal energy storage application. Hornfels and Schist are used in the project, because they are the only locally available rocks that is the most cost effective option for construction of an experimental test facility. The cost of transport and logistics made it an unattractive option to make use of dolerite in the construction of the TES facility in this project (Allen, 2014).

2.1.3 Porous Media CFD, Conceptual Simulation

Numerical modelling of a conical shaped rock bed with an inverted thermocline has previously been conducted by Louw (2014). Discrete and porous computational fluid dynamics were used to define the model of the TES. Modelling of a large scale system by Louw (2014), and the potential low-cost of implementing a rock bed as thermal energy storage, contributed to the desirability of building the experimental prototype described in this project.

A porous CFD model was validated against experimental measurements in the study conducted by Louw (2014). Experimental measurements that were used to validate the porous CFD model done by Louw, were based on the experimental test facility described by Allen (2014). The porous CFD model was used to predict the thermal behaviour of a large scale TES with a similar conical packed bed geometry as the test facility built in this project. A thermal distribution from the CFD results is shown in Figure 2.2

Irregular particle shapes of rocks have been modelled in discrete element modelling by representing the irregular rock as a combination of a clustered grouping of different sized spheres (Nel, 2013). Appropriate geometric models such as the developed model in Figure 2.3 can be used for detailed CFD

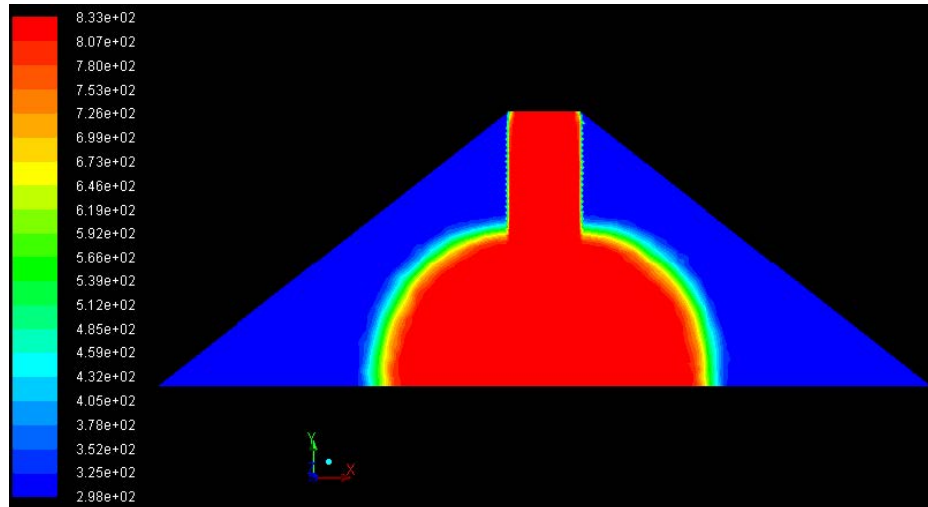


Figure 2.2: Large scale CFD simulation results for a 150 m footprint diameter by Louw (2014), showing the temperature distribution after 8 hours of charging

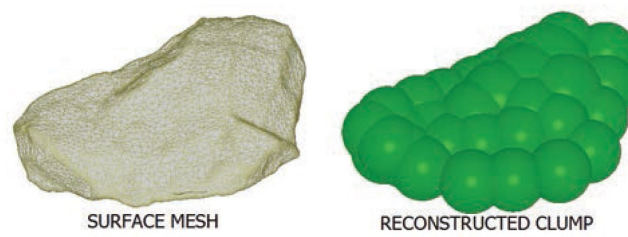


Figure 2.3: Rock reconstruction using automatic clump generator in CAD (Nel, 2013)

studies. Discrete element modelling of pressure drop over a packed rock bed for TES were investigated in the study conducted by Nel. Investigation on self-supporting tunnels for air flow within packed beds was done and it was found that self-supporting tunnels can be formed if the appropriate steps are followed (Nel, 2013).

2.1.4 Techno-Economic Study: Costs

Due to the abundance of numerical models available in the literature for flow in porous media, an experimental setup for the most promising concept is required to validate which packed bed concepts could be technically feasible and which concepts would only be feasible in theory. The techno-economic feasibility of the concept on a system level needs to be investigated and experimentally validated to convince potential investors that the rock bed TES is an option to consider in the construction of future solar power plants. From an economic perspective, the rock bed storage concept seems promising for

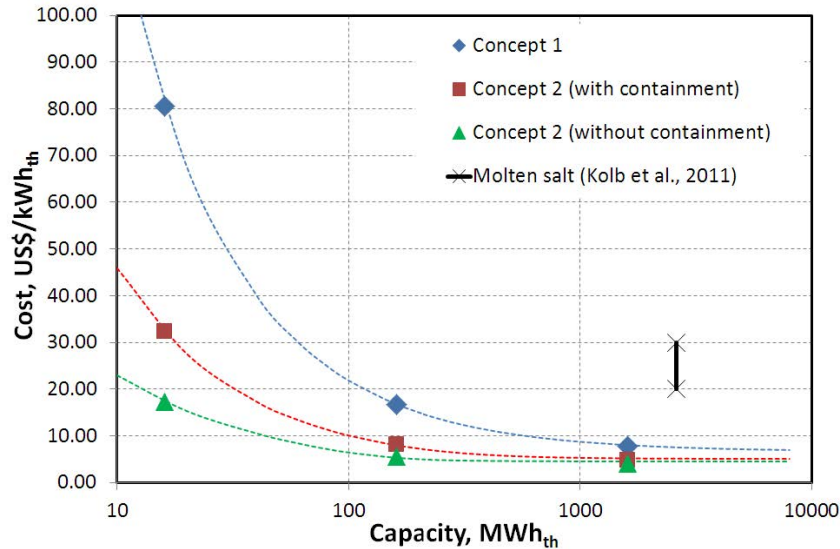


Figure 2.4: Rock bed TES concepts cost comparison (Allen *et al.*, 2016)

use in industrial scale power plants (100 MW) in terms of the cost of the whole system. The preliminary installation cost for a 1600 MWh_{th} rock bed thermal storage can be below 10 USD/kWh_{th} while a corresponding capacity molten salt storage system installation cost is in the range of 20 USD/kWh_{th} to 30 USD/kWh_{th} (Allen *et al.*, 2016). Predicted specific installation cost for different cost effective alternative TES concepts are given in Figure 2.4. The trend of capital expenditure on TES indicates the financial advantage of constructing a large scale TES.

2.2 Cost Effective Rock Bed Concepts

Thermal energy storage in a packed bed of rocks can be achieved in many ways. Different concepts were proposed to meet the requirements for a TES system that can be used with a Rankine cycle, combined cycle and that can be incorporated at the outlet side of a gas turbine. A conceptual proposal should make provision for high temperature TES (600 °C) and a layout that is practically feasible. To generate a cost effective concept, a simple yet effective system layout is required that can deliver heat for an extended period to match demand.

Two different conceptual versions of this type of TES are available in the literature. One of the concepts is developed into a tangible test facility during the course of this project, see subsection 2.2.2. The alternative concept has a similar system layout, but the heat is stored in the top part of the TES. The concept with the inverted thermocline as described in subsection 2.2.2 has an optional roof or containment structure. Two variations on this concept exist, one with a containment and the other without a containment.

2.2.1 Concept 1

The first cost effective concept consists of a packed bed of rocks which is covered with an airtight roof structure that is well insulated. Heat stored in the fully insulated top part of the containment structure and low temperatures at the bottom part of the TES medium, minimize the thermal losses to the environment and the soil below the TES. A TES as described in Figure 2.5 is typically charged from the top with hot air blowing through the rocks, transferring the energy to the storage medium and cool air exiting the TES at the bottom. Air ducting and channels below the packed bed can be seen Figure 2.5(a). The idea is to construct the air ways below the rock pile of stainless steel gabion walls by using the storage material as the construction material to install perforated air ways in the rock bed.

The rock pile on the inside of the TES is piled up at the natural angle of repose with little to no physical constraint of the packed bed. The reason for having a rock pile that is not in a confined space is to prevent any form of ratcheting when the storage medium undergoes thermal cycling. A simple and cost effective design for the containment structure is acceptable when the containment structure does not experience mechanical load from internal pressure of the packed bed. As shown in Figure 2.5(a), the sand or rock foundation of the wall structures is supporting the wall from both inside and outside. To scale the up the TES, the geometry can be extended as shown in Figure 2.5(b). The cost estimate for the first concept as proposed by Kröger (2013) is given in Figure 2.4.

2.2.2 Concept 2

A second concept for packed bed TES as proposed by Gauché and Louw (2014) is depicted in Figure 2.6. The bulk of the storage material is packed at the natural angle of repose and a roof structure or cover is optional for this concept. In this study however, the version of this concept with the containment is investigated due to equipment limitations. Refer to subsection 3.1.2 for the reason the option with the containment (cover) is chosen. By storing thermal energy at the bottom of the packed bed, no significant thermal insulation is required on the roof side of the TES. Thermal losses to the soil, which acts as an infinite heat sink, requires proper thermal insulation at the center base of the TES to minimize thermal losses to the soil beneath the hot region. Concept 2 is discussed in depth in this thesis via simulation, experimental testing and documented observations of the system performance during operation of a test facility. A variation on Concept 2 without the optional containment is not covered in this project.

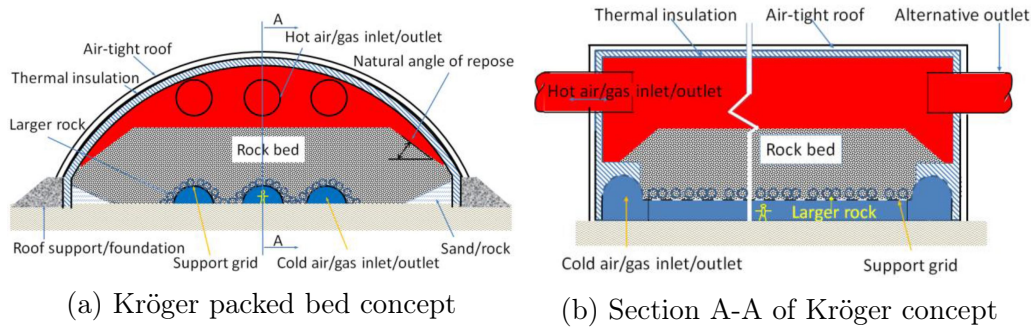


Figure 2.5: Packed bed TES concept showing the air flow ducting and hot region (Allen *et al.*, 2016)

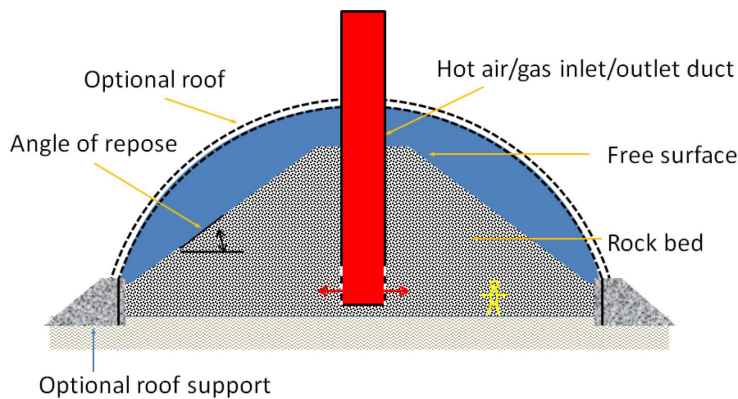


Figure 2.6: Inverted thermal energy storage concept proposed by Gauché (2014)

2.3 Ait Baha Facility: Morocco

The Ait Baha CSP pilot plant in Morocco is the first pilot scale TES pilot facility that has been built and tested for high temperature thermal storage in a packed bed of rocks (570°C). The storage medium is a packed bed of rocks with air as a heat transfer fluid. The stored thermal energy is used for electricity production through a steam-based Rankine cycle. Heat for the system is captured with a unique parabolic trough design that feeds $1/3$ of the heat for electricity production and $2/3$ of the heat for two individual TES systems. A truncated geometry to store the thermal energy was used in this design. The truncated, conical under-ground design, was chosen to minimise the effect of ratcheting to extend the life span of the rocks. A schematic layout of this TES is described in Figure 2.7 (Zanganeh *et al.*, 2012).

The system was commissioned in the year of 2014 and tests results show that the concept to store high temperature thermal energy in the top part of a packed rock bed is successful. Commissioning of the pilot facility showed that air as a heat transfer fluid can be successful to heat up a packed bed of rocks. The pilot plant is shown in Figure 2.8, where Figure 2.8(a) shows the roof dome

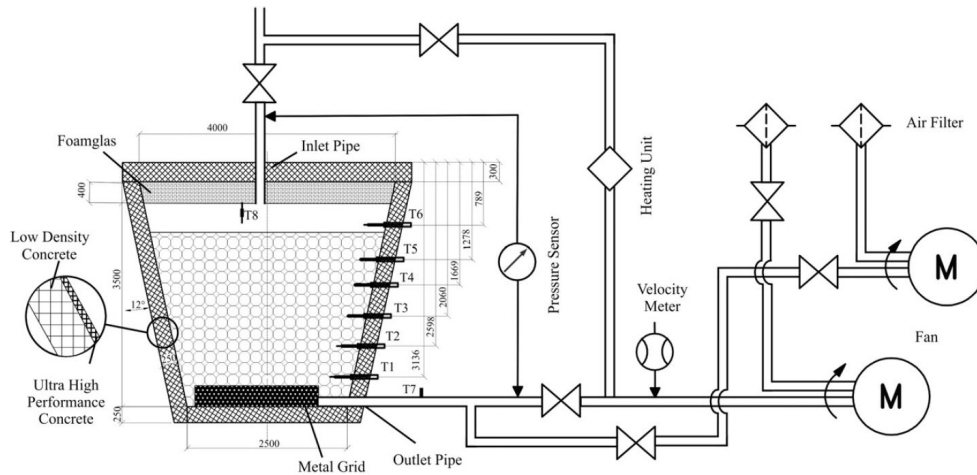
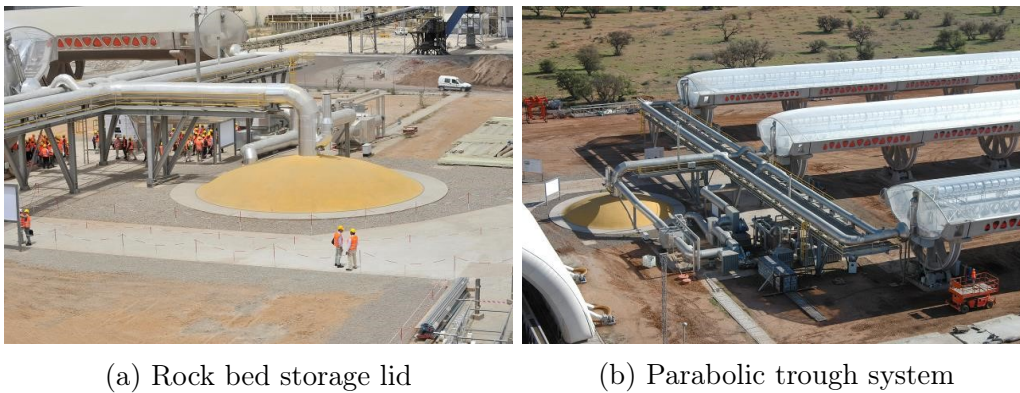


Figure 2.7: Schematic layout of the pilot-scale thermal storage configuration and experimental setup (Airlight Energy, 2014)



(a) Rock bed storage lid

(b) Parabolic trough system

Figure 2.8: Ait Baha CSP pilot plant photos in the Agadir region, Morocco (Airlight Energy, 2014)

of the underground TES system and Figure 2.8(b) indicates the location of the parabolic troughs and the piping layout. The outlet temperature of air for this specific TES at the Ait-Baha pilot plant in Morocco is in the range of 150°C (Airlight Energy, 2014). Testing of the TES showed that after a certain number of cycles, a steady state was reached. This steady state was only reached after sufficient number of thermal heating and cooling cycles. Stratification of the thermocline can be observed in the publication by Zanganeh *et al.* (2012). The thermocline approaches a constant gradient profile as the thermal storage reaches quasi equilibrium. The thermal gradient profile in the packed rock bed proves to be stable after 20 – 30 cycles.

Advantages of the TES layout that was constructed at the Ait Baha CSP pilot plant are such that no rigid containment structure is required to contain the TES material. The natural ground formation is used as supportive structure to contain the rocks. Refer to Figure 2.7 for the layout of the underground

storage. Disadvantages of this concept of TES includes the large construction preparation and location of the instrumentation. A large hole would need to be dug in the ground in preparation for the TES system. Removal of rocks from below the ground would be tedious if the storage material must be replaced after some time. All instrumentation for measuring the temperature and equipment located beneath the ground are difficult to replace or repair in case of failure.

Valuable lessons learnt from this pilot test facility can be implemented in TES research for the CSP application. This is the only pilot thermal energy storage that has been constructed and is available in the literature which consists of a packed bed of rocks. The TES at the Ait Baha facility was experimentally tested in the temperature range of 20 °C to 650 °C. Multiple charge discharge tests were performed experimentally with an 8 h charging time and a 16 h discharging time. An overall thermal efficiency of up to 95 % was achieved for this specific TES design. The Ait Baha facility achieves this efficiency with insulation while the design in this thesis considers an uninsulated design, the charge and discharge times give a good indication on the charging and discharging capabilities of a packed rock bed as a TES.

Chapter 3

Experimental Setup Development

3.1 Concept Generation

The concept under consideration is based on a cost effective design of a TES for potential use in the CSP, combined cycle power plants and process heat application. An introduction to the description of the concept investigated in this study is given in subsection 2.2.2. This concept consists of a conical shaped packed rock bed with air as a heat transfer fluid in an airtight containment structure that is uninsulated. Heat is stored in the bottom center of the conical rock bed referred to in this project as an inverted thermocline.

3.1.1 Conical Shape Geometry

The concept under investigation consists of a bulk material piled up in a conical pile above the ground. A fixed conical geometry of the rock pile is set variable in this project. A prototype of the concept proposed by Gauché and Louw (2014) is the main motivation for the construction of the test facility in this study (Allen *et al.*, 2016). The proposed concept has a conical shape to avoid a heavy containment structure for the packed bed. The natural angle of repose of the rocks used in this project is the design specification for the slope of the free surface of the conical rock pile. The concept on which the experimental facility built in this study is based on the conceptual drawing in Figure 2.6. Advantages of this particular concept include the easy removal of the rocks from the TES when the storage medium reaches a point where there needs to be replacing, and easy stacking of the rocks upon initial installation. The outer regions of the conical rock bed serve as insulation, thus no expensive insulation is required to be installed on the TES.

3.1.2 Ducting Layout

The system layout for this study was specifically chosen to accommodate the fan on the cold side. Therefore an airtight containment structure (cover) is

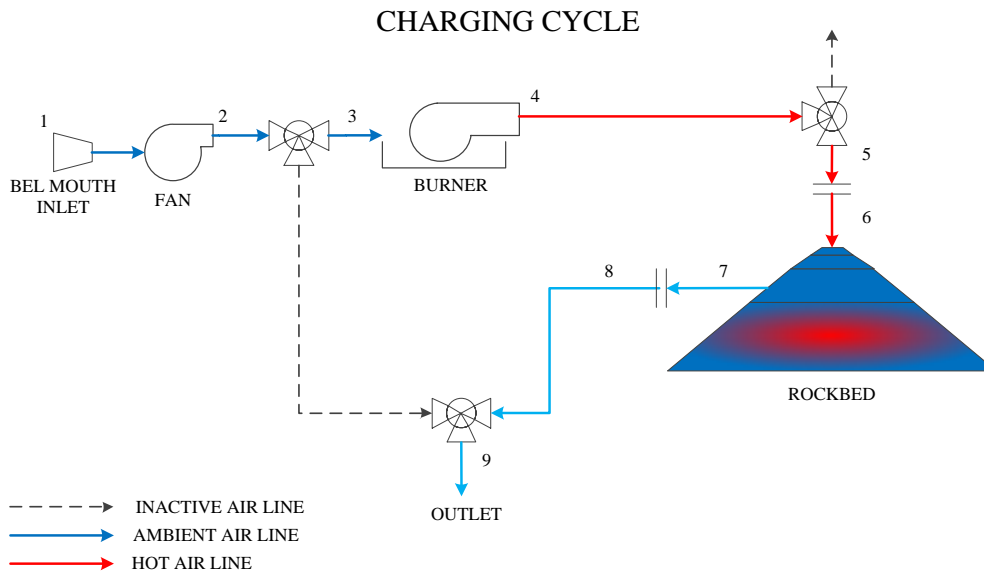


Figure 3.1: Flow diagram of the system when operating in charging mode

required to discharge the system with the fan located on the cold side of the cycle. Discharging of the TES is achieved by creating a positive pressure inside the airtight cover which induces flow of air downwards through the rock bed and out at the bottom of the center pipe. The charging pipe is equipped with an inspection hole that also serves the purpose of a hot air outlet. No air sealing valves are thus required on the hot side of the TES cycles. Cost of a potential high temperature capable fan is too high for the application of an experimental test facility.

Figures 3.1 and 3.2 illustrates where the main equipment is located in the system layout and also indicates the hot air and the cold air flow regions. In theory, a blower can be installed to draw the hot air out of the storage, but there must be heat exchangers between the blower and the TES to remove the energy from the fluid before it enters the blower. This is not covered in the scope of this project. Subsequently, the heat is only dumped into the environment.

The layout of the hot air ducting is described in Figure 3.3. A gas burner is located on the side marked with the combustion chamber. A dual purpose elliptical inspection hole is indicated on the stainless steel tubing. This hole is sealed off with a lid and insulation box to minimize heat losses to the environment while the system is in charging mode. The lid is opened when the TES system is in discharging mode and the hot air is directed outward at this position. Insulation is installed over the full length of the hot air ducting to keep thermal losses to the environment to a minimum. Air outlet into the rock bed is at the lower end of the vertical pipe. An air expansion chamber is installed at the bottom of the vertical ducting to decrease the flow velocity of the air blown into the porous rock bed.

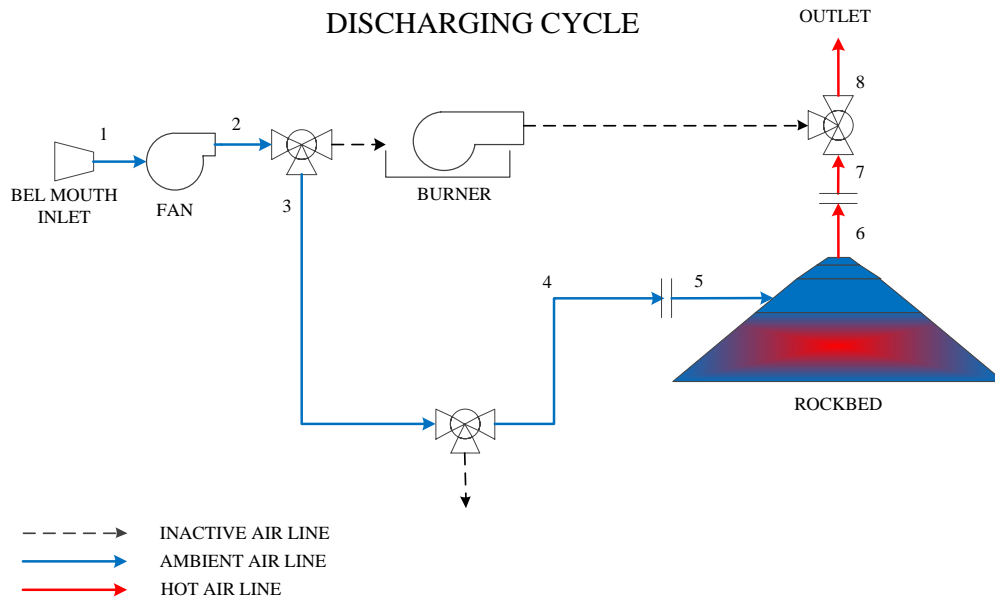


Figure 3.2: Flow diagram of the system when operating in discharging mode

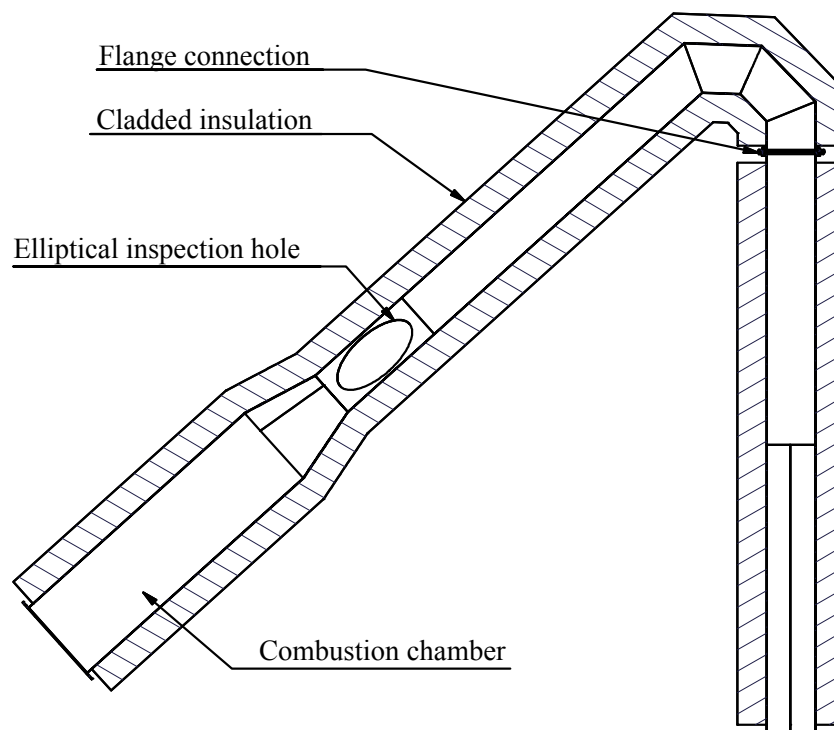


Figure 3.3: Hot ducting drawing layout



Figure 3.4: Base insulation beneath the thermal storage facility under construction

3.1.3 Cost Effective System Options

No insulation is installed on the wall or cover of the containment structure, however, the base of the thermal storage is thermally insulated from the soil where the hot region is identified by simulating the heat distribution in the TES. The base insulation under construction can be seen in Figure 3.4. Insulation boards that are made of calcium silicate are installed on a level sand base with two layers of clay brick pavement on top of them. The calcium silicate insulation boards and a single layer of clay bricks can be seen in the image.

An airtight containment structure remains challenging on this scale for a low-cost experimental test facility. An inflated and deflated tarpaulin cover can be seen in Figure 3.5. A set of steel cables were installed above and below the tarpaulin cover to provide extra support to the sheet metal wall structures. The tensioned cables help carry the load of the inflated cover by indenting the surface of the tarpaulin canvass when it is pressurized. The radius of curvature of the inflated material is thus shortened and results in reduced in-plane stress developing in the tarpaulin cover. Tensioned cabling is a cost effective option that provides structural integrity to the containment and it is easy to install.

Material selection for the containment structure, ducting, diverse construction materials and equipment are all based on the most cost-effective combination. Another important engineering requirement is material selection that is resistant to high temperatures. High temperature air requires the use of ducting that should withstand temperatures up to 650 °C for extended periods. All the hot ducting is insulated to minimize thermal losses to the environment.

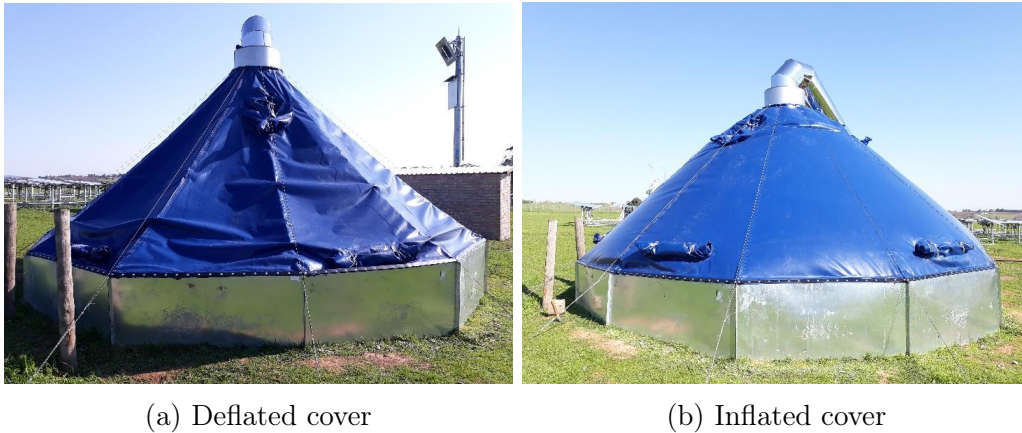


Figure 3.5: Airtight tarpaulin cover deflated with no flow present, and inflated during charging mode

3.1.4 Airtight Containment Structure

Airtight containment is achieved by sealing the low-temperature joints with rubber gaskets and silicone adhesive. All joints in the containment structure (wall-to-cover and wall-to-wall) are flange bolted connections which can be tightened evenly to accomplish a smooth seal. A low-cost, light weight cover is installed that is both airtight and easy to assemble. The lightweight nature of the tarpaulin cover does not require heavy and strong support structures to hold it in position. A tarpaulin canvas material is used for the cover and is applicable for the airtight application. Provision is made in the scenario of a power outage. Ventilation holes located in the cover can be opened to induce a natural flow of fresh air to cool down the air gap beneath the tarpaulin cover and the free surface of the rocks.

The airtight seal between the walls and the soil is achieved by submerging the base of the wall into the soil. Bent up design of the wall sections ensures that the compacted surrounding soil contributes to an airtight seal between the sheet metal wall structures and the surrounding soil. A drawing of a wall section can be seen in Figure B.6 in Appendix B.

3.2 Design Specifications

Design specifications based on the most cost-effective equipment and materials for this test facility are taken into consideration. The thermodynamics of the system operations were taken into account while detailed design was done on the structure and the system layout. Flow characteristics of hot air at 650°C as well as cold air at ambient temperature is investigated to specify the design conditions for the system. See Table 3.1 for the rated specifications of the system.

Pressure drop over a porous medium was calculated to specify what pumping power is required to overcome the pressure drop in the packed bed of rocks. The pressure drop in the rest of the system is also taken into account for specifying the size of the blower. For this specific flow rate as well as pressure required for the application, a closed impeller blower is identified as the most suitable option. See specifications of the fan in Appendix D.5 where the type of fan as well as the rating of the fan is indicated.

3.2.1 Material Selection

Construction materials for the various parts in the experimental facility were chosen based on the specification of the material at high temperature. Elements such as wind, sun and rain have an influence on the selection of the materials that are exposed. The material that the canvas cover is made of is UV-resistant for up to 5 years and can be used in wet conditions as well. A PVC coated polyester tarpaulin is the description of the material the cover is made of. Specification of the tarpaulin cover can be seen in Appendix B.1.

Ducting for the hot air is made of stainless steel grade 409. This stainless steel grade is widely used in industry for exhaust pipe manufacturing and is a stable material to use at high temperatures. The flame containing pipe, located in the combustion chamber, is made of a higher, more expensive grade stainless steel 316. Combustion of a gas burner can easily reach temperatures up to 1200 °C. High temperature resistant ceramic fibre gasket material is used to manufacture the gaskets for sealing between the high temperature flange connections. See Appendix B.4 for the thermal properties of the high temperature resistant gasket material. The expansion chamber for the air at the outlet of the hot ducting is made of structural steel. Structural steel has sufficient strength left at elevated temperatures compared to stainless steel grades at the same temperature. Mechanical properties of structural steel at elevated temperatures can be found in literature and compare well with the mechanical properties of applicable stainless steel grades (Antonio *et al.*, 2012; Columbus Stainless, 2007). The applicable mechanical properties of the steels are listed in Table 3.2. Construction steel was chosen for this application because of the high strength at elevated temperatures and the low cost of the raw material.

3.2.2 Thermodynamics

The alternative heat source in the form of a LPG gas burner was chosen for the heating up the TES test facility. The burner was specified according to the heating capacity of the existing Helio100 facility at Stellenbosch University mentioned in section 1.3 of Chapter 1. Expansion of the test facility for future research in CSP is potentially a project for the STERG at Stellenbosch University. Rating the heating capacity and the storage time of the current

Table 3.1: Design parameters of the prototype, rated values

Design parameter	Rated	Units
Heating capacity	400	kW _{th}
Charging time	5 – 8	hours
Total energy storage	1.5 – 2.5	MWh _{th}
Fan power	5.5	kW _e
Fan pressure	6	kPa
Rocks weight	70 000	kg
Maximum charging temperature	550 – 650	°C
Maximum outlet air temperature	40 – 60	°C

Table 3.2: Mechanical properties of steels at elevated temperatures

Material	Yield strength at 500 °C [MPa]
Ferritic stainless 3CR12	236
Structural steel S355-NL	265

built TES is based on a proposed expansion of three times the existing heat capacity of the solar field. Preliminary calculations were done to determine the total mass of the packed bed TES for this project.

Selection of the gas burner and the specifications of the installed burner can be seen in Appendix D.2 under the burner type RS 44 MZ. The flame size of this specific burner is the design guideline for the size and shape of the combustion chamber. Maximum flame size calculation is done according to the table given in Appendix D.1. A flame temperature in excess of 1200 °C usually requires refractory material for the flame containing pipe. Alternative design for the flame containing pipe is developed and a low-cost design is implemented to protect the thin walled ducting and the flame containing nozzle. A staggered design for the flame containing pipe was pursued to enable the flame nozzle to be constantly cooled down during the operation of a charging cycle. A drawing of the staggered nozzle is documented in Appedix D.4. The flame containing pipe is connected on the Riello burner nozzle at the small end of the flame containing pipe. Cool air flow from the burner side constantly cools down the flame containing pipe to prevent it from overheating. Annular air openings at each step in the pipe diameter allows for cooling air to enter the combustion chamber from an upstream direction.

Flame operating conditions require a combustion chamber size as described above with a diameter of 450 mm, but the rest of the hot air ducting is manufactured at 250 mm diameter to save material and keep the cost low. Insulation installed on the hot ducting is specified to be 150 mm thick mineral wool which is covered with a 0.8 mm stainless steel cladding. Thermal losses through the insulation is approximately 549 W/m for an internal temperature of 500 °C and a cladding temperature of 36 °C as stated by the manufacturer.

Table 3.3: Rated air flow parameters summary

Flow parameter	Value	Units
Cold side pipe diameter	200	mm
Hot side pipe diameter	250	mm
Cold side flow velocity	16	m/s
Hot side flow velocity	30	m/s
Cold side volumetric flow rate	0.5	m ³ /s
Hot side volumetric flow rate	1.5	m ³ /s
Overall mass flow rate	0.6	kg/s
Combustion chamber pipe diameter	450	mm
Expansion chamber outlet area	1.43	m ²
Air entry velocity	1.05	m/s
Actual velocity (porous rock bed)	2.33	m/s

3.2.3 Flow Characteristics

Airflow in the ducting is rated to be 0.5 m³/s on the cold side and 1.5 m³/s on the hot side of the air flow cycle. A design limit for the internal flow velocity in the ducting is set to be 35 m/s. Calculation of the maximum air flow velocity in the hot ducting shows that for a 250 mm pipe diameter, the flow velocity is 30 m/s. Flow velocity on the cold side is calculated to be a maximum of 16 m/s for a pipe diameter of 200 mm. The system is designed to handle a maximum mass flow rate of 0.6 kg/s. See Table 3.3 for a summary of the flow parameters specified for the system.

3.2.4 Pressure Drop Characteristics

A fan to overcome the pressure losses of the piping system, the pressure drop over the packed rock bed and to deliver the volumetric flow rate required, was specified for the system. A design point for fan operation was specified for a volumetric flow rate of 0.5 m³/s at a maximum pressure of 6 kPa. See the specifications sheet with the pump curve of the fan in section D.5 in Appendix D.

Pressure drop over the respective ducting sections were calculated according to correlations available in literature. The implicit relation between the ducting geometry, surface roughness, and the friction factor for turbulent flow is given by the Colebrook equation as defined in equation 3.1 (Cengel and Cimbala, 2010). Example calculations for the pressure drop in the system are given in Appendix C. A total pressure drop of 1577 Pa was calculated for the system at the rated volumetric flow rate of 0.5 m³/s. The fan is over specified for the application of this project, because the future use of the test facility was taken into account during the purchasing of expensive capital equipment.

$$\frac{1}{\sqrt{f}} = -2.0 \log \left(\frac{\varepsilon_{sr}/D}{3.7} + \frac{2.51}{Re\sqrt{f}} \right) \quad (3.1)$$

Table 3.4: Rated pressure drop over various flow sections in the system

Flow region	Pressure drop [Pa]
Cold duct	335
Hot ducting	878
Packed bed	364
Total pressure drop	1577

3.3 Experimental Method Design: Measuring Equipment and Control

The experimental setup is used for gathering experimental data to use as validation of the results produced by numerical simulation in Chapter 5. The volumetric flow rate of the heat transfer fluid (air) through the porous medium is monitored and recorded during each test. The volumetric measurement along with the temperature of the air at the point of measurement is used to calculate the mass flow rate of the air. The amount of energy that is put into the storage medium (rocks) is calculated by the amount of enthalpy that is transferred to the rocks. Temperature measurement of the heat distribution is only measured by measuring the air temperature in the packed bed. No particle temperature measurement instrumentation has been installed for measurements during experiments in this study. The placement of thermocouples inside rock specimens was not done during this project, because the physical stacking process of the rocks made it practically challenging to install thermocouples inside rocks without them being destroyed in the bulk handling process. Broken thermocouples cannot be replaced without moving tons of rocks, which would not be practically possible when the TES facility is fully assembled.

3.3.1 Mass Flow Measurement

Mass flow measurement is achieved by means of a long radius nozzle (bellmouth) at the inlet of the fan. Pressure drop measurement at the throat of the bellmouth was used to calculate the volumetric and mass flow rate at the inlet of the fan. Calculation of the mass flow rate is done by using equation 3.2. The discharge coefficient C_d is calculated as shown in equation 3.3 and is assumed to be equal to 0.9975. The diameter ratio β is defined in equation 3.4 where the D defined as the ducting diameter and d is the throat diameter. Due to the bellmouth open to atmosphere and not in a ducting, D_{bm} is assumed to be infinitely large (Cengel and Cimbala, 2010).

Two different pressure measurement taps were installed to measure pressure drop over packed bed during the operational cycles. A pressure reading on the inside center of the packed bed and a pressure tap installed close to the free

surface of the packed bed are used for pressure drop measurements over the packed bed.

$$\dot{m} = A_{\text{bm}} C_d \sqrt{2\Delta P_{\text{bm}} \rho_a} \quad (3.2)$$

$$C_d = 0.9975 - \frac{6.53\beta^{0.5}}{Re^{0.5}} \approx 0.9975 \quad (3.3)$$

$$\beta = d/D_{\text{bm}} \approx 0 \quad (3.4)$$

3.3.2 Temperature Measurement

Measured air temperature at the outlet side of the TES is logged to calculate the enthalpy of the air that is blown through the rock bed. A measured temperature distribution of the air in the rock bed gives an indication of the amount of energy stored in the rocks. The stored energy in the rock bed is used to calculate the efficiency of the heat recovery on a charge-discharge-cycle basis. Refer to Chapter 5 for the thermal efficiency definitions of the TES system.

The thermocline in the storage medium is measured with type-K thermocouples. Two vertical temperature measurement planes in the conical pile are installed perpendicular to each other for testing the repeatability of the measuring equipment. The potential axis-symmetric nature of the TES can be identified by having two sets of temperature readings in the conical rock bed. A photo of the actual thermocouple frame in the drawing in Figure 3.7 can be seen in Figure 3.6. A drawing indicating the placement of the thermocouples on a typical plane can be seen in Figure 3.7. The position of the thermocouples on the stainless steel frame is indicated with the round red dots on the drawing. Each position where the thermocouple tips are stationed is perforated to be exposed to the air in the immediate environment.

Placement of the experimental temperature measurement equipment was based on the predicted temperature profile obtained through the simulation of the TES. Thermocouples were placed more densely in the region where the high temperature air in the storage material had been identified in simulated results.

3.3.3 Simple Burner Control Design

The control system of a two stage gas burner was implemented to have temperature control at a maximum charging temperature. Modulating gas burners can be controlled to have a specific flame size to match the wanted heat requirement, but this is not used in this project because of the high cost of the control system for the burner. A charging curve that resembles a saw tooth profile is a good description of the heat input curve achieved during a charging

3.3. EXPERIMENTAL METHOD DESIGN: MEASURING EQUIPMENT AND CONTROL

27



Figure 3.6: Thermocouple placement frame and air distribution box on the thermal energy storage base

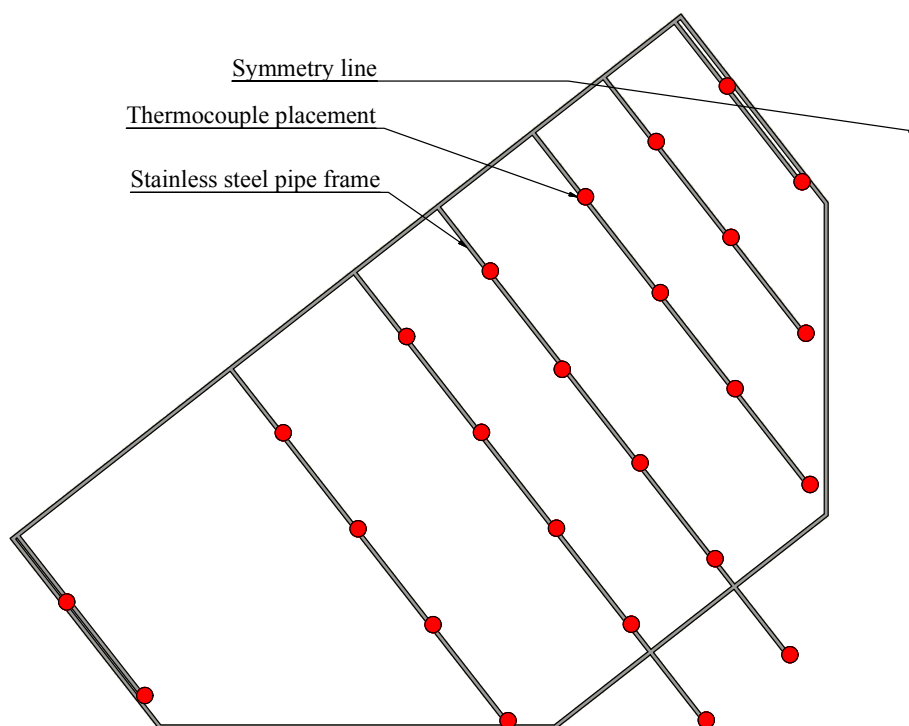


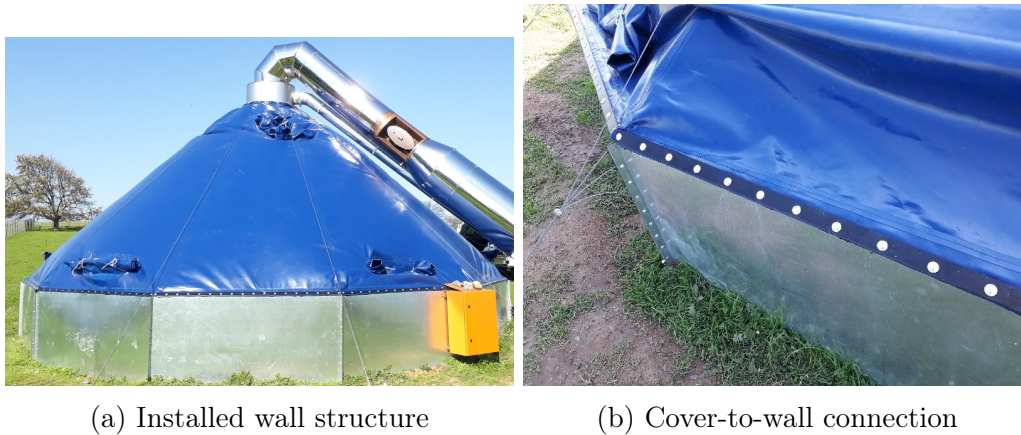
Figure 3.7: Placement of thermocouples on the stainless steel pipe frame

cycle in this study. A two stage flame setting allows a heat input curve that is much smoother than that of a burner with only one flame setting (single stage).

During a control cycle when the burner is active, the burner operates at high firing rate, with both stages active until the temperature threshold is reached. The controller then sends a signal to the burner to switch to low fire (first stage only). The flame does not switch off completely during a control cycle, it only switches from high fire to low fire to achieve the correct heating value. The burner is on high fire (first and second stage on) for 21 seconds, and on low fire (only first stage on) for 7 seconds. Thermal inertia in the insulated hot ducting also contributes to a smoother charging curve. A steady state average charging temperature of 642 °C was achieved during the first full charge of the commissioning test.

In addition to the main controller of the burner, there is a safety controller installed to ensure safe system operation. The main controller is connected to a temperature probe installed approximately 4.5 m downstream of the burner in the middle of the hot air ducting. A feedback signal from the main controller is fed into a Shinko controller that has direct control over the burner (Shinko, 2005). A secondary safety controller is connected in series with the main controller to ensure safe operating conditions of the burner in the burner box. A thermocouple placed in the burner box monitors the immediate temperature in the housing of the burner. In the rare case where the temperature in the burner box enclosure might go beyond 60 °C, the safety controller will immediately switch off the burner. The burner control circuit can be seen in Appendix D section D.3.

Inherent safety features are built into the internal control system of the burner. The gas burner goes through an automated purging process each time before it starts up for the first time. Purging of the burner happens in a certain sequence. The burner flow control fan is started up at full speed where after the camshaft for the air fuel mixture opens up all the way and closes again. This step is done in order to clean out any unburned gas potentially left in the system and to test if the cam-shaft for the air fuel mixture is fully operational. Gas is introduced by opening the main solenoid gas supply valves and an electrical spark ignition is activated to start the flame of the burner. If the flame fails to start after the purging sequence, the gas supply is immediately cut and the burner goes into a lockout mode. This is achieved by a flame detector installed near the nozzle of the burner. In case of abnormal burner operation, the flame detector tests if the flame is on after the burner is signalled to start up normally. If no flame is detected, a lock out signal will cause the burner to switch off completely. In case of normal burner operation, the flame detector recognises that there is a flame present and the burner operation will continue normally.



(a) Installed wall structure

(b) Cover-to-wall connection

Figure 3.8: Cover-to-wall flange connection details

3.4 Experimental Facility Layout

A thermal energy storage test facility can have different system layouts. The specific TES investigated in this study is an experimental test facility designed and built for a specific set of objectives as described in Chapter 1. A thermal storage medium that is a packed bed of rocks with the heat stored at the bottom center is a unique and distinctive characteristic of the concept described in this project. Unlike other conventional TES systems, this TES is completely without insulation for the bulk storage medium. An overview of the experimental facility subsystems and components is given in this section.

3.4.1 Containment Structure: Walls

Walls that mainly confine the lower edge of the rock bed are bent galvanized sheet plates. Thin material is sufficient for the manufacturing of the wall structures, since it does not see significant dynamic loading from the rock pile. An average height of 250 mm of rocks is in contact with the wall sections, the top part is exposed to the the air gap between the cover and the free surface of the rocks. All walls are bolted in a 12 sided ring to form a dodecagon shaped ring. Due to the uneven soil, the wall structure is submerged in a trench in the soil to obtain a level installed wall assembly structure. The wall sections are submerged in the soil below to achieve an airtight joint to the ground as described in subsection 3.1.4. The installed walls can be seen in Figure 3.8(a). The top part of the wall sections are also reinforced with steel cables that supports the roof as shown if Figure 3.8(b).

3.4.2 Containment Structure: Cover

An airtight and watertight tarpaulin cover had been installed on the TES facility that covers the rocks and serves as an inflatable structure for the purpose

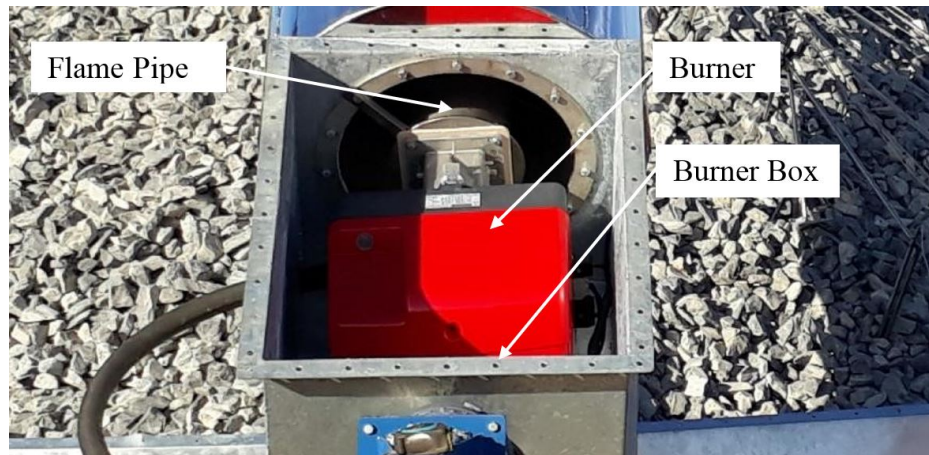


Figure 3.9: Burner installation in the air flow line

of discharging the energy from the system. The cover-to-wall connection can be seen in Figure 3.8(b). The cover is equipped with ventilation holes that could act as cooling mechanism in case of power or fan failure.

3.4.3 Gas Burner Description

A gas burner running on LPG has been selected as the most applicable heat source for the application of this project. As the immediate surroundings are in the agricultural environment, a clean burning fuel had to be selected to minimize pollution to the air, soil and plants. A gas storage and an accompanying gas train was installed for fuel delivery to the gas burner. Storage of the fuel is in the form of 48 kg LPG cylinders. A double-10 gas manifold is installed to accommodate direct usage of the liquid gas from the cylinders. A vaporizer expands and heats up the expanding gas to prevent freezing of the gas supply system while the burner is in operation. The maximum rated fuel mass flow rate for the burner is 30 kg/hour. The location of the burner in the flow line can be seen in Figure 3.9.

3.4.4 Fan

A centrifugal blower with a closed impeller was identified as the most suitable blower for the application of this TES prototype facility. Relative low flow rates and high pressure are required as described in section 3.2.4. The blower is equipped with a 5.5 kW_e 3-phase induction motor. Mass flow rate of the system is controlled by making use of a variable speed drive. Frequency control of the fan motor enables the user to maintain the required mass flow rate through the system. Refer to Appendix D.5 for the complete fan specifications.

3.4.5 Ducting

Stainless steel grade 409 is used for the high temperature application where there is a significant mechanical load on the structure. Corrosion resistance of this grade stainless steel, manufacturability of the steel and the low cost make this the most suitable available material for manufacturing of the hot air ducting. Due to the high cost of stainless steel compared to the low cost of normal galvanised mild steel sheet metal, all the ducting on the cold side of the cycle is made of galvanised mild steel.

Thermal expansion and contraction of the ducting due to the heating and cooling of the stainless steel pipe wall causes a displacement in the free hanging end of the ducting which is connected to the burner box. Thermal expansion is calculated using the thermal expansion coefficient, α_s , as found in the technical brochure of a steel supplier in South Africa (Columbus Stainless, 2017). A thermal expansion value used for α_s is $12.4 \mu\text{m}/\text{m}$. The simple formula to calculate the change in length of the stainless steel ducting is given by equation 3.5, where d_l is the change in length of the material (expansion) and the L_0 is the original length of the ducting section. A temperature difference of 600°C is used to calculate the displacement for the worst case scenario.

$$d_l = L_0\alpha_s(\Delta T) \quad (3.5)$$

3.4.6 Air Outlet Distribution

For cost reduction on the material which is exposed to high temperatures, the design is adapted to make use of the most suitable materials. Steel with sufficient mechanical properties at elevated temperatures is used for the construction of the the air outlet distribution box at the bottom of the rock pile. Static load from the packed rocks at the bottom of the packed bed exerts a force on the air distribution box. A steel structure made of 25 mm reinforcement steel is used to distribute the air at the center of the packed rock bed. Figure 3.10 displays a photo taken through the stainless steel woven wire mesh during the construction phase of the air distribution structure. An increased outlet surface is required to expand the flow and to decrease the outlet velocity of the air exiting the hot air ducting.

3.5 Experimental Procedure and Results

3.5.1 Gas Burner Operation during Testing

Operation of the gas burner at a set point is achieved by temperature feedback to an automated controller. The operating temperature is selected and the hysteresis value is set on the controller of the burner. Burner operation is only allowed when the fan is running to ensure safe operation of the system. After



Figure 3.10: Inner view of the air outlet distribution structure

the gas supply is enabled and checked and the fan is running at the start up speed, the burner is simply started by switching it on once. In case of burner lockout or failure to start, a remote reset button on the control panel can be used to reset the burner and it can be started again after the cause of failure or error is identified and the problem is solved. Safe operation of the gas burner must be ensured at all times. Refer to subsection 3.2.2 and subsection 3.3.3 for more detail on the burner specification and burner control details respectively.

3.5.2 Fan Operation during Testing

The fan is controlled during operation by making use of a variable frequency drive. Mass flow rate through the TES system is governed by changing the frequency of the fan and monitoring the flow measurement at the bellmouth. Control of the fan is done manually during a typical test, since the mass flow through the system stays constant for both the charging and the discharging periods. Fan speed is reduced when the burner is started up for the first time. Once the system is operating in charging mode, the fan frequency is increased to acquire the operating mass flow rate.

When switching to discharging mode, the insulation box over the inspection hole is removed and the inspection hole is opened. Cool air is rushed through the combustion chamber at an increased flow rate to cool down the wall of the combustion chamber. Cooling of the metal is required to prevent conduction of heat back to the burner box while the system is in discharging mode.

Table 3.5: Design parameters of the prototype, rated values and commissioning values

Design parameter	Rated	Commissioned	Units
Heating capacity	400	318	kW _{th}
Charging time	5 – 8	4.5	hours
Total energy storage	1.5 – 2.5	1.43	MWh _{th}
Fan power	5.5	0.9	kW _e
Fan pressure	6	1.4	kPa
Rocks weight	70 000	65 000	kg
Maximum charging temperature	550 – 650	642	°C
Maximum outlet air temperature	40 – 60	51	°C
Mass flow	0.60	0.48	kg/s

3.5.3 Commissioning

The commissioning test required that the system was operated well within the specified operating envelope to ensure safe operation of the TES facility. The commissioning test consisted of a single charging experiment of the open system without the cover installed. The rock bed was charged up to where the TES was fully charged. A fully charged system is defined when the average air outlet temperature on the free surface of the rock pile measures a constant temperature of higher than 50 °C. See the comparison between the design specifications and the commissioned values in Table 3.5. This first test without the cover was done to see what effect the ambient wind conditions and buoyancy of hot air internally would have on the temperature distribution in the rock bed. Buoyancy of the hot air plays a significant role in the distribution of the stored energy in the rock bed while the system is in storage idling mode. Storage idling mode is defined when the airflow at both the inlet and outlet of the rock bed is shut off. During the storage idling mode, natural convection induced by the hot air rising through the porous medium will cause the hot air to move upwards, leave the rock bed at the top and is lost to the environment. Results of what is happening with the thermal distribution over a period of time is discussed in the section 6.1. After successful commissioning of the system, further tests were done to measure how effective the stored heat can be retrieved from the TES.

3.5.4 Full Charge — Discharge Test

A full thermal energy storage cycle was performed to obtain the thermal performance of the TES on a system level. Temperature distribution through the storage medium was measured during the charging cycle to measure how the heat front propagates in the storage medium. Pressure drop of the air was measured at the throat of a bellmouth on the inlet side of the fan. A pressure

difference relative to ambient pressure is measured at the throat of the bellmouth at the inlet side of the fan. An average mass flow rate of 0.48 kg/s and 0.53 kg/s were maintained for the complete duration of the charging and the discharging cycles respectively.

3.5.5 Uncertainty Analysis

Accuracy of experimental results is directly dependent on correctness and the accuracy of measuring instrumentation. Measured experimental results are acquired by logging data with an Agilent 34972A LXI data acquisition switch unit. The accuracy for measurements with a data logger operating in ambient conditions in the range of -18°C to 28°C is listed in a Technical Overview document from the manufacturer (Agilent Technologies, 2012). Temperature measurement with a type-K thermocouple has an accuracy specified as a percentage of the reading plus percent of the range. The reading is defined as the actual measurement and the range is defined as the value of the scale in which the current measurement is categorized.

Combining elemental errors in the data logging system was done in a manner that larger error values have a bigger influence on the overall uncertainty of the results. The root-sum-squares method was used to sum the elemental errors as described by Figliola and Beasley (2006). Equation 3.6 describes the relation between the individual elemental uncertainty factors e_k , and the overall uncertainty in the measurement, u_x . The minimum DC reading measured during experimental testing is used for calculation of the percentage error measured by the pressure transducer at the throat of the bellmouth. Calibration of the pressure transducer relative to a Betz micromanometer is discussed in Appendix E. A general acceptable probability of uncertainty can be taken as 95% as shown in equation 3.6.

$$u_x = \pm \sqrt{e_1^2 + e_2^2 + e_3^2 + \dots + e_K^2} u_x = \pm \sqrt{\sum_{k=1}^K e_k^2} \cdot (P\%) \quad (3.6)$$

Mass flow measurement in this study is dependent on the ambient inlet temperature, ambient pressure and the pressure reading at the bellmouth throat. Air density used in mass flow equation 3.2 is a function of the ambient temp and the ambient pressure. Accumulative error for the mass flow measurement equates to the root-sum-square of the error in temperature, ambient pressure, measured pressure difference and data logging. A total uncertainty value of $\pm 3.53\%$ had been calculated for the mass flow rate.

Experimental error that might be caused as result of external factors is assumed to be insignificantly small. Since the charging and the discharging cycles are done with the same flow measurement equipment, any potential inherent fault is consistent in both the charging and discharging cycles. Any

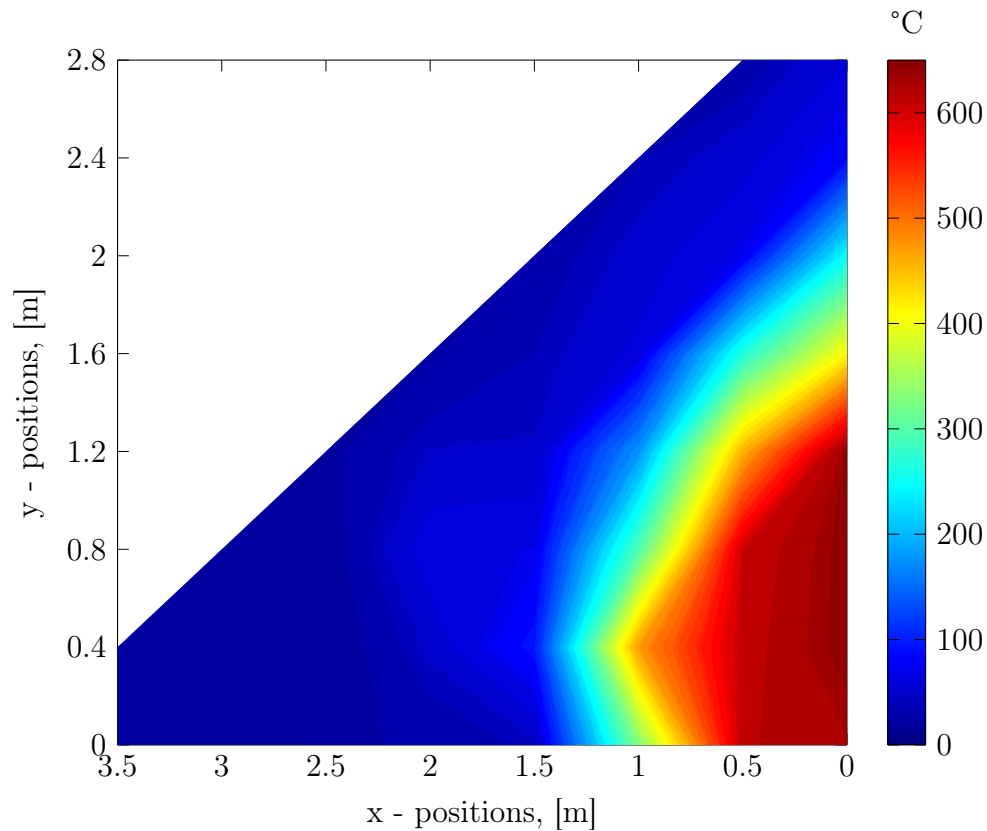


Figure 3.11: Thermal image taken during commissioning test while in idling mode

offset caused by experimental error as results of a consistent fault would have the same offset incorporated in the results.

Temperature measurement is done by using type-K thermocouples which are rated for temperatures up to 1370 °C. Uncertainty of the thermocouples is calculated to be less than $\pm 3.91\%$ for the range in which the useful energy is measured. Energy flow through the system is defined as a function of the mass flow rate and the air temperature at the inlet or outlet of the TES. A total uncertainty of $\pm 5.27\%$ was calculated for the energy flow through the system.

Table 3.6: Storage material volume efficiency

Packed bed property	Value	Units
Total rock mass	65	tons
Heated rock mass	21.5	tons
Thermally active rock mass	43.5	tons
Volume efficiency	33	%

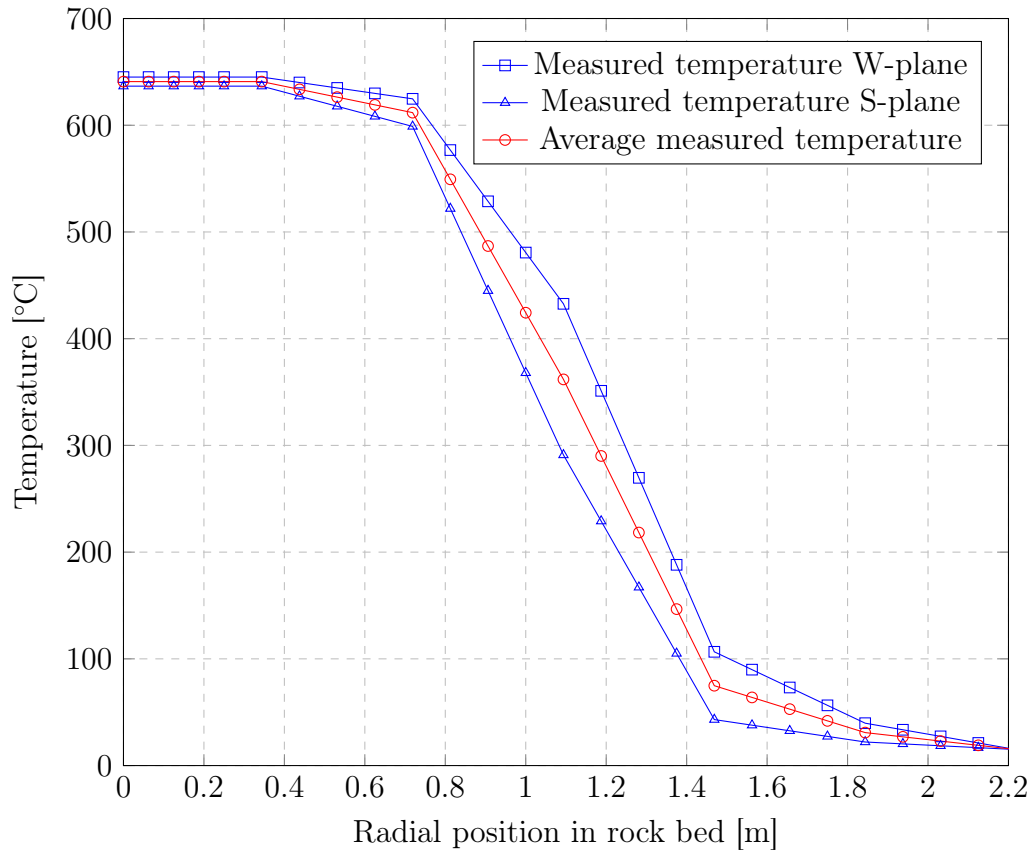


Figure 3.12: Radial air temperature comparison between measured thermoclines for the West-plane and South-plane at a charged state during the commissioning test

3.5.6 Experimental Results

Energy stored in the storage material was calculated for the TES at a charged state. Stored energy in the packed bed was calculated by using the effective volume of rocks at elevated temperatures. Specific heat capacity of the rocks is defined as a function of temperature and is incorporated in the calculation of the total energy in the rocks at a charged state. Effective thermal usage of the packed bed is listed in Table 3.6. Only 33% of the total rock mass reaches a temperature above 50°C when the TES is fully charged. A low volumetric efficiency can typically be expected for a TES of the scale as the facility built for this project, because the thermocline profile only occupies the centre bottom part of the TES facility.

A contour plot of the temperature distribution of a fully charged TES system can be seen in Figure 3.11. The core of the packed bed is the region with the highest temperature directly after the system had been fully charged for 4.5 hours. The outer lower region of the conical packed bed does not participate in the thermodynamics of the system, but only serves as structural mass.

Table 3.7: Thermal performance and efficiencies of the TES calculated from experimental measurements

Fraction of total energy input	Value [%]
Useful energy recovery	60
Total energy recovery	92
Thermal losses to soil	2.2
Thermal losses, blown through	1.6
Miscellaneous thermal losses	4.2

Figure 3.11 is plotted from data gathered during the commissioning test on the 15th of June 2017. A temperature line profile is plotted to compare the two temperature measurement planes and can be seen in Figure 3.12.

Useful thermal energy recovery was calculated to be 60 % of the total thermal energy pumped into the TES. Energy input and output of the system was calculated from the measured temperature of the air entering or exiting the TES as well as the mass flow rate of air. The useful thermal energy recovery efficiency of 60 % accounts for thermal losses to the soil, thermal losses to the environment and the energy that could not be retrieved from the TES. Due to the nature of the experimental facility, it is required to discharge the TES immediately after each charging cycle. By discharging all the attainable energy from the TES (includes air temperature below 327 °C), output energy yielded a total thermal energy retrieval of 92 %. Thus, the TES discharges effectively given that the TES is discharged directly after a fully charged state is reached. Thermal performance parameters are summarized in Table 3.7.

Buoyancy has a significant effect on the thermal distribution and the high temperature zone in the packed bed over a short period of time after the TES was fully charged (4 hours). Recoverability of the heat stored in the TES is directly dependent on the location of the high temperature zone. In this particular concept under investigation, the heat is introduced to the packed bed at the bottom and is extracted at the same location. Therefore, if the high temperature zone diffuse to a higher region, the heat cannot effectively be extracted through the perforated opening at the bottom of the packed bed any more.

Pressure drop measured over the whole system while the system was in operation was 1400 Pa. Refer to Table 3.8 for the parasitic power consumption of the fan. Thermal images taken during the commissioning test can be seen in Figure 3.13 and Figure 3.14. Figure 3.14 shows the low outer surface temperature of the TES while the TES was charged with air at 642 °C. High thermal capacity of the rocks absorb and store the thermal energy to ensure that the outlet temperature at the free surface of the packed bed stays below 50 °C.

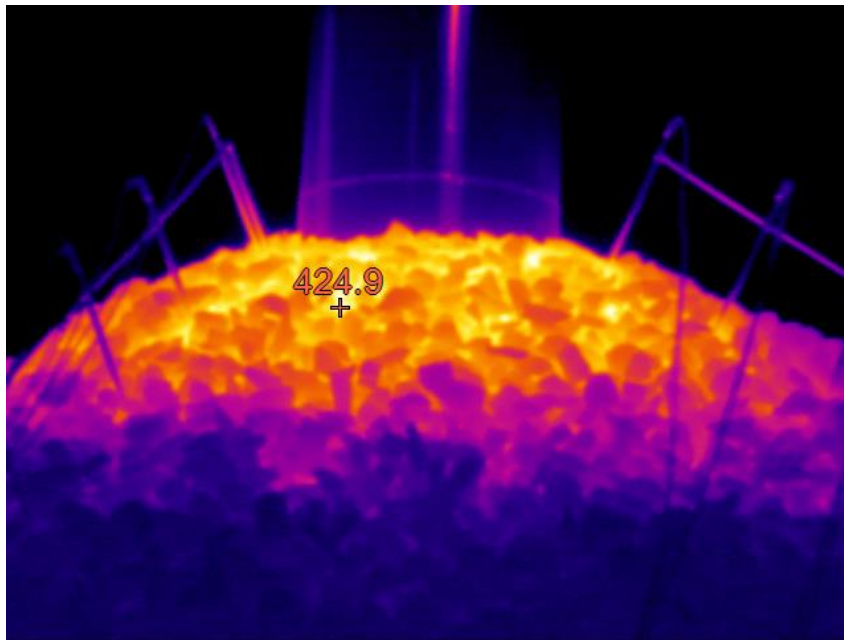


Figure 3.13: Thermal image taken during commissioning test while in idling mode, 8 hours after end of charging cycle

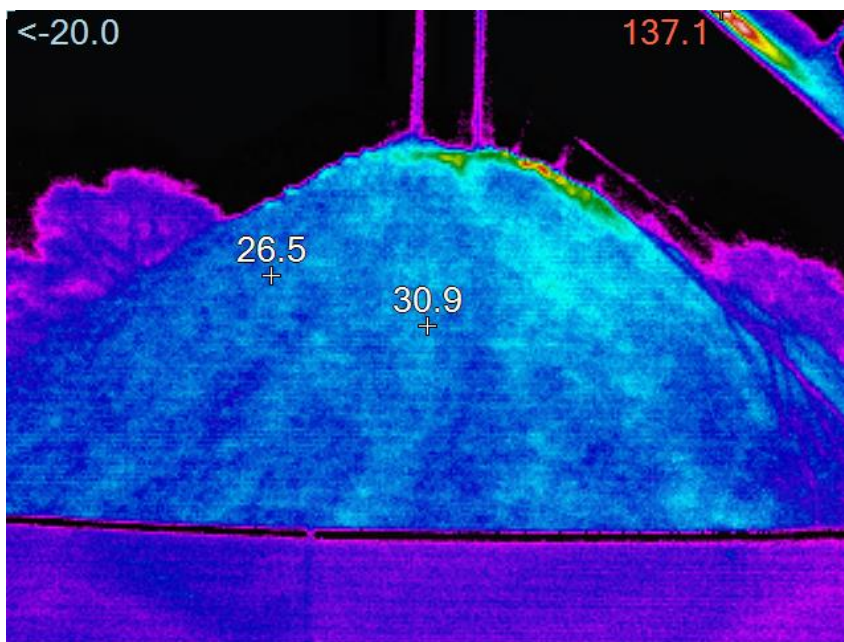


Figure 3.14: Thermal image taken during commissioning test while charging at 642°C

Table 3.8: Pressure performance characteristics of the fan during experimental testing

Pumping pressure parameter	Value	Units
Pumping power	0.9	kW _e
Max pressure	1400	Pa
Pressure drop measured over packed bed	318	Pa
Pumping power fraction	±0.3	%

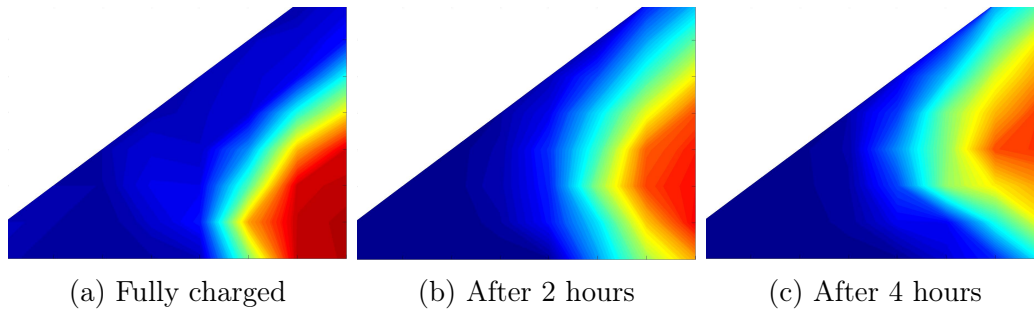


Figure 3.15: Temperature distribution of the system in idling mode

3.6 Observations during Testing

Observations during testing showed that buoyant forces had a significant effect on the temperature distribution throughout the rock bed. Figure 3.15 illustrates an idling time lapse of three consecutive images and shows the effect of buoyancy of hot air over a time period of 4 hours. The pressure gradient in the rock bed dictates the flow direction of the fluid. Absolute pressure difference in the rock bed was mainly caused by the hot air at the bottom center of the rock bed which has a density difference from ambient temperature air by a factor of three. Due to the dependence on the flow velocity, the maximum heat transfer takes place where the most turbulent flow is present and where the temperature difference between fluid and particle temperature is the largest.

Outlet maximum average air temperature on the free surface of the rock bed soon reaches a level of approximately 45 °C during the charging cycle. The outlet air temperature stays consistent at this temperature level until the end of the charging cycle is reached.

Notes were taken during the experimental testing of the thermal storage facility for later use in the data analysis. Information on the behaviour of the TES system can also be used for future research in this field of study. Observations of how the immediate environment has affected the results of the tests are discussed in this document to ensure that the lessons learnt during this study can be used by future researchers for planning on the operational strategies and design layout of a TES.

Chapter 4

Construction of Experimental TES Facility

Construction of an experimental test facility was done in parallel with development of a numerical model. A test facility to deliver experimental results that covers the experimental objectives of this project did not exist for use prior to this project, therefore a TES facility was built for this purpose. Design and construction of the TES facility is based on the preliminary simulated results obtained from the numerical model.

For construction of the experimental thermal energy storage facility, it was required to have all the necessary preparation on site done before the construction was started. The experimental facility requires a gas (LPG) supply and a source of electricity to be operational. Since the installation site is located outside of the residential area on the agricultural test farm of Stellenbosch University, the existing infrastructure was limited to the available electrical power sources and water points. No existing gas supply line is locally available and therefore a new gas supply system was installed. Construction on site mainly involve assembling of prefabricated parts. Most of the assembly work could be done by two engineering students.

4.1 Methodology

A construction methodology was developed around the available resources in the research group for this project. Since the focus of the project is on the cost effective development of a TES, it is applicable to make use of the best design to keep the cost low, which is also fully functional. The design procedure is an iterative process which is a product of the availability and cost of the materials and equipment. Various designs for the respective subsystems were generated and developed into one working system which is made up of all the subsystems. Operating temperatures, operating pressure and the mass flow rate of air in the system are three variable parameters that must be accommodated throughout

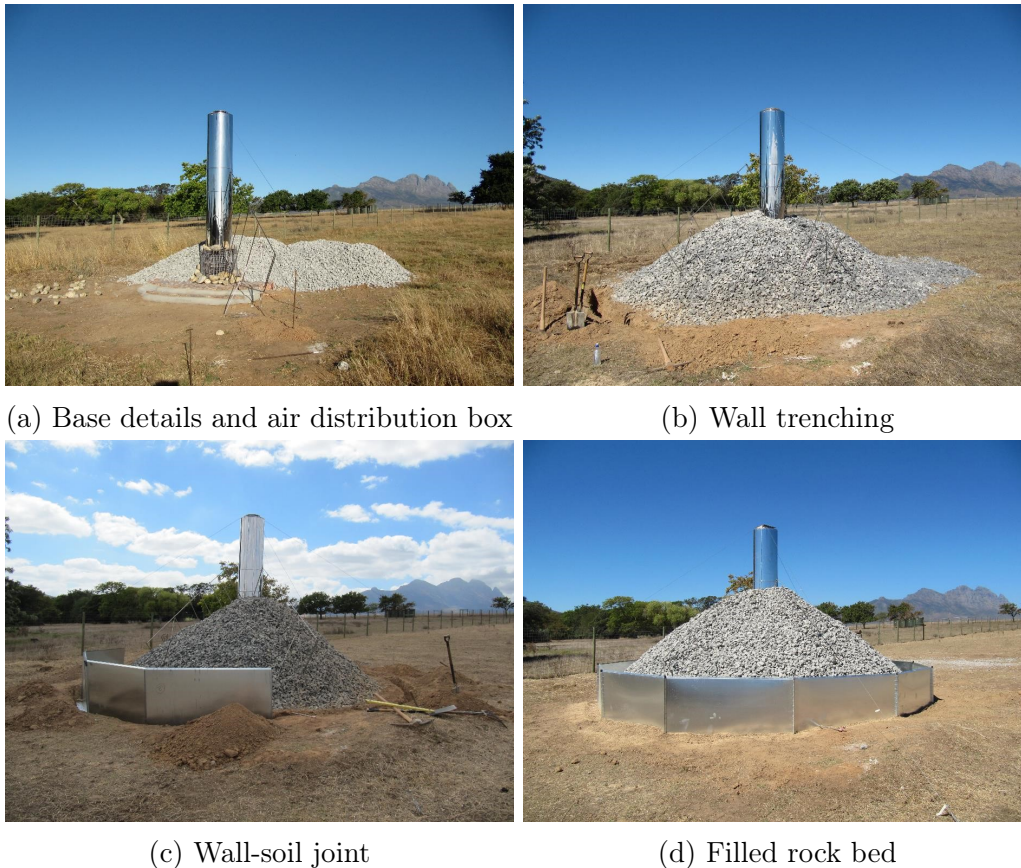


Figure 4.1: Rock bed Construction Progress Photos

the system design. Airtight joints at high temperatures require more expensive gasket material, such as ceramic fibre, that can last at high temperatures. Joints in the assembly of the airtight containment structure for the TES on the ambient temperature side are sealed off with rubber gaskets that are not expensive.

4.2 Installation Progress Record

Construction progress was recorded by means of engineering drawings and photos taken during the course of the construction phase. Various phases of the TES experimental facility initial construction can be seen in Figure 4.1(a) to Figure 4.1(d). The construction period was from October 2016 to July 2017. As the construction made progress, a series of photos were taken from the same angle to get a perspective of the real hardware developing into the final TES facility.

The first construction progress of the TES facility as shown in Figure 4.1 shows the installation of the base, air distribution box at the bottom of the vertical pipe, walls, central heating pipe and the filled conical pile of rocks.

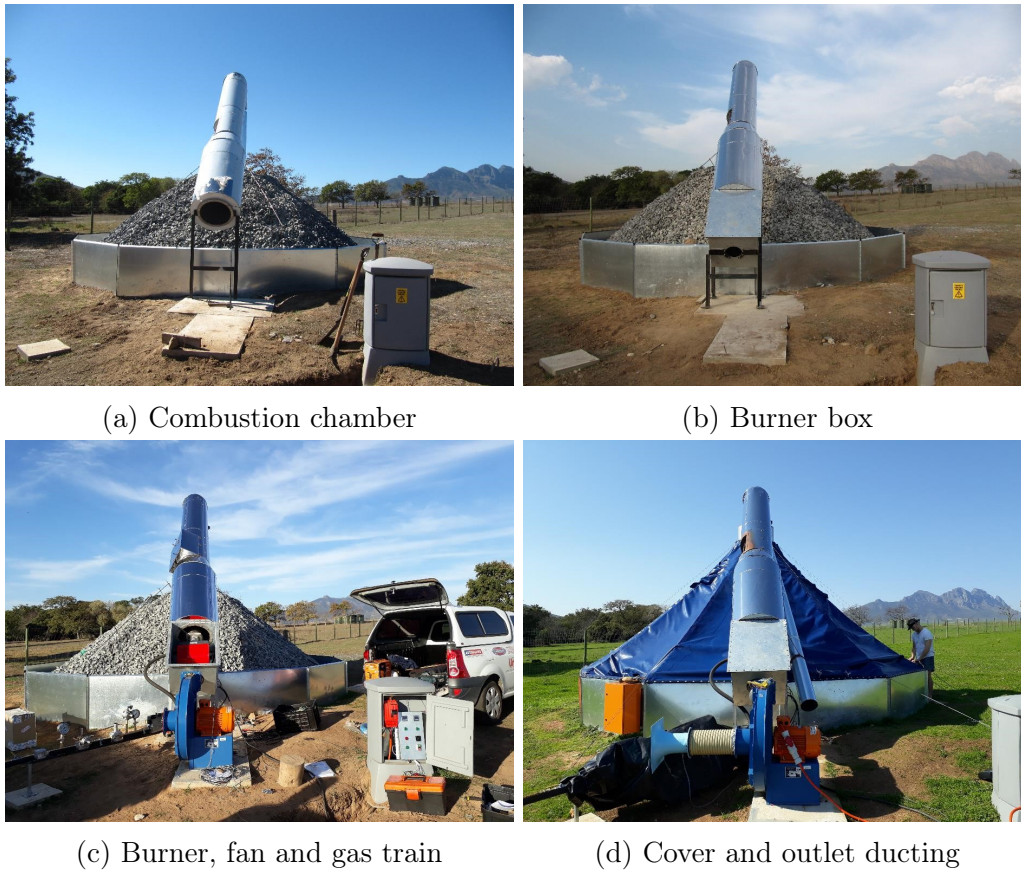


Figure 4.2: Rock bed heating system construction progress photos

The installation of the hot air ducting, combustion chamber, burner box and the fan can be seen in Figures 4.2(a) to 4.2(c). An inflatable cover installed over the rock bed with tensioned cabling keeping the cover in place is depicted in Figure 4.2(d). As seen in Figure 4.2(d), the inflatable cover is deflated and supported by tensioned cabling from below. An operating TES experimental facility is illustrated in Figure 4.3 where the cover is inflated while operating in charging mode.

4.3 Subsystem Installation

4.3.1 Insulation and Base

The base below the thermal energy storage was levelled and insulated only in the area where the storage medium is calculated to be at the highest temperature during operation. Material for the base insulation is calcium silicate in the form of boards that are 50 mm thick. Two layers of clay bricks were paved on top of the insulation boards to serve as additional low cost insulation and as a protective layer for the brittle and soft ceramic fibre boards.



Figure 4.3: Operating TES in a charging state



(a) Air distribution box



(b) Hot air ducting

Figure 4.4: Air distribution box and insulated ducting

4.3.2 Air Distribution Box

A distribution box for expanding the airflow is installed at the bottom of the vertical hot air ducting. A stainless steel woven wire mesh wrapped around the steel frame ensures that the rocks do not fall into the expansion chamber. The expansion chamber with the wire mesh installed below the vertical ducting section can be seen in Figure 4.4(a).



Figure 4.5: Installation of the walls in trenches

4.3.3 Hot Air Ducting

Ducting containing the hot air during operation is insulated with mineral wool and covered with a polished stainless steel cladding. An insulating box is placed over the inspection hole in the ducting to minimize thermal losses while the system is in charging mode. The hot air ducting which is fully insulated is shown in Figure 4.4(b). The section of the ducting to the right of Figure 4.4(b) with the enlarged diameter is the combustion chamber that houses the gas flame when in operation.

4.3.4 Wall Installation

Figure 4.5 shows a picture of the wall installation in trenches. Connection between the soil and the wall sections is achieved by filling back the soil after the wall sections are connected level relative to the neighbouring wall sections. A 12 sided trench shape was prepared to accommodate the wall assembly. Each corner has an angular change of 30° in order to achieve a dodecagon shaped wall assembly.

4.3.5 Stacking of Rocks

The stacking of rocks requires some machinery for bulk handling of materials. To minimize the moving of a large mass of rocks after delivery and therefore saving on labour costs, a stacking strategy was planned. The strategy involves piling up the first loads of rocks on the exact location where it must be placed in the storage system layout. After the rocks were poured around on the base, it was moved into a neat conical pile with ground moving machinery. All preparation work on the base of the TES system thus needs to be done before the first rocks were delivered.



Figure 4.6: Stacking of the rocks by using a conveyor belt and a small excavator



Figure 4.7: Accumulator box connected to the cover

After the footprint of the pile of rocks reached the boundary where the wall sections are to be installed, the stacking of rocks was paused temporarily until the 12 sided wall sections were installed. The remaining rocks were filled after all wall sections were fixed in position. A conveyor belt was used to pile up the remaining rocks as seen in Figure 4.6.

4.3.6 Cover and Accumulator Installation

For assembly of the inflatable cover, it is required to fix the accumulator on top of the vertical ducting before the tarpaulin cover is fixed to the accumulator box. A flange connection between the tarpaulin cover and the accumulator box ensures an airtight connection between the steel flange and the polymer cover. Figure 4.7 shows the connection between the accumulator box and the tarpaulin cover. Support cabling for the inflatable cover is connected to the accumulator box and the wall sections to give structure to the inflatable dome

as depicted in Figure 4.3. An airtight cover is installed over the rock bed to enable the system to be discharged.

4.4 Safety During Construction

Safety on a construction site is always a main concern for the site manager and the owner of the hardware under construction. The experimental test facility constructed during this project covers a large range of safety issues. Gas handling and installation of an industrial scale gas train, electrical installation, handling heavy equipment, working at heights and also working with dangerous and hazardous power tools are all covered during the construction phase of this project as well as the operational phase. All personal protective equipment (PPE) must be used in the particular cases where it is applicable. PPE used during construction includes the following: Safety glasses and hearing protection while grinding work is done, gloves and a welding helmet when welding is done and hard nose shoes when working with heavy objects in general.

For the gas train installation and the complementary gas storage as well as installation of the gas burner, it is required by law to meet all the standards and specifications set out by the regulations for industrial scale gas installations. A process must be followed to ensure that the gas plans are drawn up according to the applicable regulations (As stipulated by the Occupational Health and Safety Act of 1993) The procedure begins with specifying the gas supply system and the drawing of the plans for the gas supply line. Specifications of the gas train must take into account the consumer side of the gas supply line (burner specifications). Specification of the burner includes the heating capacity as well as the typical description of the operations (fuel mass flow rate, total fuel consumption, type of fuel and time required for refilling). The site boundary acquired from a local municipal site plan and the existing infrastructure in the environment where the new gas installation is planned are factors taken into consideration when the gas plans are drawn up. All the necessary information that is site specific was obtained by the compliance officer during a site visit to the actual planned site of installation.

4.5 Safety During Operation

During operation of any power plant, provision must be made for what to do in case of emergency. Some unforeseen circumstances such as a power outage or failure of equipment can cause damage to other equipment (equipment downstream of the fault in the system). If it is not properly managed or according to a set out plan from the manufacturer of the plant, damage may occur. In case of failure of critical equipment required for safe operation of a facility,

it is required to have some backup strategy to help mitigate the potential consequences. When circulation of a cooling fluid in a nuclear reactor fails, overheating could occur and cause serious consequences to the totality of the power plant. Similarly, in the TES facility constructed, the cover requires a constant flow of cool air to protect the material from overheating. The TES system is inherently safe only during charging or discharging cycles when there is a constant flow of air.

With no air flow present in a charged or semi-charged state, the hot air rising in the rock bed due to buoyancy will accumulate in the top part and potentially overheat the tarpaulin cover damaging it permanently.

Due to the conical shape of the cover, the height difference between the lower part of the cover and the top part of the cover can be exploited to make use of natural convection. The natural convection is caused by the buoyancy effect of the hot air and the temperature difference that will occur between the air inside the containment structure and the ambient air temperature.

In case of a power cut or failure of the blower, a mitigation strategy is used to open up the holes in the canvas cover to let cool air in at the bottom and give access for the hot air to escape at the top. The holes are located axis symmetrically around the cover to ensure equal distribution of air when all are open. A drawing of the tarpaulin cover indicating the location of the ventilation holes can be seen in Figure B.2 in Appendix B.

Chapter 5

Numerical Simulation of TES Performance

5.1 Introduction

Numerical simulation of a TES system using a 1 D mathematical model is a simple and effective way of predicting the heat transfer characteristics, pressure drop and cycle performance of the TES under investigation. This chapter focuses on the development of a mathematical model that is based on heat transfer and pressure drop correlations that had been experimentally validated and developed for heat transfer in a packed bed of rocks (Allen, 2014).

5.2 Heat Transfer

A one dimensional numerical model is developed to describe the heat transfer and flow characteristics of air in a conical shaped rock bed. The geometry (as described in more detail in Chapter 4) is a conical pile of rocks at the natural angle of repose. Due to the non-constant cross-sectional area of the flow domain, a 1 D numerical model is only an approximation to a potential solution for the numerical model. Modelling in only one dimension restricts the nature of the solution to include all the effects of buoyancy in the packed rock bed.

Characteristics of the buoyancy of the high temperature air can thus not be calculated or predicted accurately by the 1 D numerical model. The numerical model does not make provision for a gravitational term to calculate the affect of buoyancy when the TES is in an idling mode. Another limitation of the numerical model is that the actual geometry of the particles is only described by a spherical equivalent volumetric diameter and not by the actual size of the particles (Allen *et al.*, 2013). This approximation is considered because the actual area measurement of a pile of rocks is practically impossible to achieve.

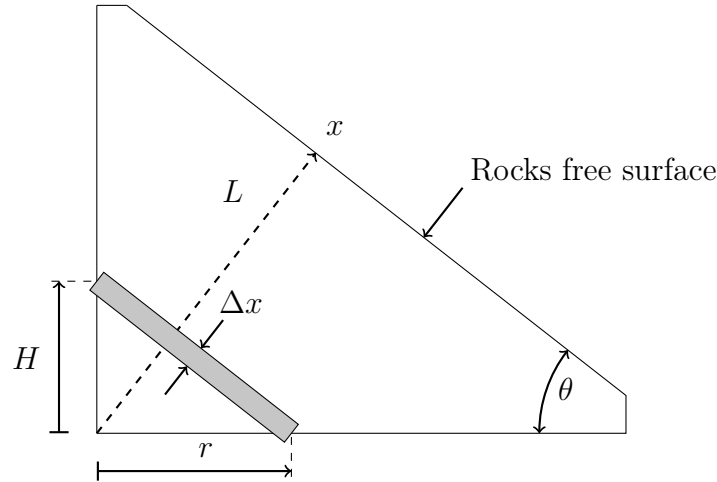


Figure 5.1: Diagram of the computational domain for the 1 D numerical model showing half the section of a cone

Two variations of a cross-sectional area for the computational domain is chosen in the development of the 1 D numerical model. A conical heat front approximation and a hemispherical heat front approximation are the two assumptions which are used to predict the profile of the heat propagation through the conical packed bed of rocks. The two respective formulations of the computational domain are described in Figure 5.1 and Figure 5.2.

In the first assumption, a conical surface cross-sectional area is the assumption made for developing the 1 D model. Cross-sectional area of the calculation domain varies from the center outward as a function of the radius of the conical rock bed. Formulation of the cross-sectional area function is the simple formula for a circular cone. Equation 5.1 describes the average outer area of the cone as a function of the height and the radius of the circular cone. Equation 5.2 define the computational spherical surface area as a function of radius. As the area varies through the computational domain, the larger cross-sectional area towards the free surface of the rocks causes the flow velocity to decrease significantly. An illustration of the computational domain and the variables used in equation 5.1 are described in Figure 5.1. The single dimension in which the flow domain is divided is the direction indicated by the radial line x , with has a total length of L and a segment size of Δx . A similar calculation procedure is done for the hemispherical computational domain approximation. The only difference is the formula for the calculation of the cross-sectional area.

$$A_{\text{cone}} = \pi \cdot r(\sqrt{H^2 + r^2}) \quad (5.1)$$

$$A_{\text{sph}} = 2 \cdot \pi \cdot r^2 \quad (5.2)$$

Heat transfer and flow calculations in a high temperature packed bed of rocks had been investigated and studied in previous work done by Allen *et al.*

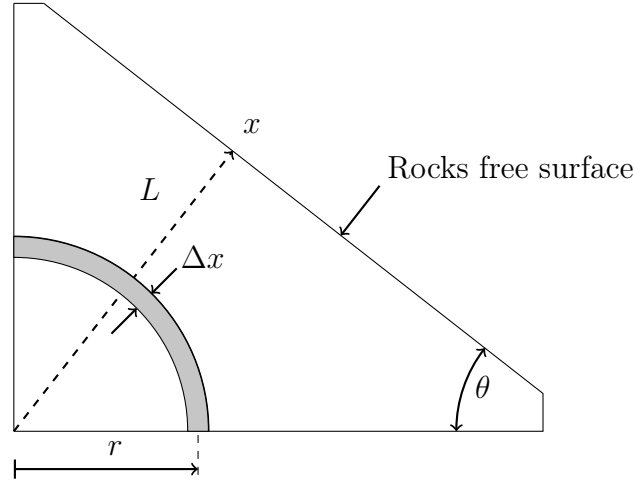


Figure 5.2: Diagram of the computational domain for the 1 D numerical model showing half the section of the hemisphere

(2015). The Effectiveness Number of Transfer Units (E-NTU) method as developed by Hughes *et al.* (1976), Duffie and Beckman (1991), prove to be a simple and effective method of predicting a 1 D temperature profile. This is a numerical approximation of the Schumann equations (Schumann, 1929).

In the charging cycle, forced convection is the dominating factor for heat transfer. Radiation and conduction between particles and between air and particles does not have a significant effect. The effect of radiation and conduction as means of heat transfer between particles is disregarded in the calculations of the system performance.

5.2.1 Governing Equations For Heat Transfer

The (E-NTU) model neglects the influence of radiation and conduction heat transfer through the rock bed (Duffie and Beckman, 1991; Hughes, 1975). Therefore the flow velocity of the fluid in the porous packed bed has a significant influence in the local volumetric heat transfer coefficient. Equation 5.3 describes the E-NTU method as a function of the mass flux G , the volumetric heat transfer coefficient h_v , the rock bed length L and the specific heat capacity of air $c_{p,a}$. Formulas and numerical methods to predict the temperature profile for the geometry described in this study is based on verified correlations developed by Allen *et al.* (2015).

$$NTU = \frac{h_v A_{cs} L}{(\dot{m} c_{p,a})} = \frac{h_v L}{G c_{p,a}} \quad (5.3)$$

The E-NTU method makes use of an NTU-constant which is given in equation 5.4. The test geometry with length L is divided into discrete segments, each defined by Δx . A varying cross-sectional area describes the flow domain in the direction of the flow. Transient heat transfer governed by the heat

transfer equations is dependent on a time constant to make the solution time dependent. Equation 5.5 presents the time constant with mass flow rate of air the only time dependent term in the equation. Fluid temperature for each segment in the computational domain is calculated by the use of equation 5.6. Iteration through the positions in the rock bed with length L is achieved by looping through the position segments of the rock bed for each time step. The subscript i denotes the index of the position in the rock bed which start at $0m$ and end at the full length, L of the packed bed.

$$\eta = 1 - e^{-NTU(\Delta x/L)} \quad (5.4)$$

$$\tau = \rho_r(1 - \varepsilon)A_{cs}Lc_{p,r}/(\dot{m}c_{p,a}) \quad (5.5)$$

$$T_{f(i+1)} = T_{f(i)} - (T_{f(i)} - T_{p(i)})(1 - e^{-NTU(\Delta x/L)}) \quad (5.6)$$

Particle temperature calculation in the model is time dependent by including the time constant in equation 5.7. The new particle temperature for the next time step is indicated by the '+' in the particle temperature $T_{p(i)}^+$ term. Current position fluid temperature includes a particle temperature in the formula to calculate the fluid temperature for the next position segment. In this way, both the fluid temperature and the particle temperature are time dependent. Interdependence of equation 5.6 and equation 5.7 requires that the solution is seeded with initial values for the particle temperatures throughout the complete computational domain. Only a vector of initial values representing the charging temperature of the inlet fluid is required for each first cell in each time step. Values for the remaining fluid temperatures are populated as the model is run over the first time step.

$$T_{p(i)}^+ = \frac{T_{p(i)}(1 - \frac{\Delta t}{2\tau} \frac{L}{\Delta x} \eta) + T_{f(i)}(\frac{\Delta t}{\tau} \frac{L}{\Delta x} \eta)}{1 + \frac{\Delta t}{2\tau} \frac{L}{\Delta x} \eta} \quad (5.7)$$

The one dimensional approach has a dual cell method of storing the particle and fluid temperature values individually for each position segment in the computational domain. The temperature difference between particle temperature and fluid temperature is the driver for convective heat transfer in the numerical model. Recursive formulas described in equation 5.6 and equation 5.7 loop through the position segments and the time steps respectively to yield a transient thermodynamic solution that can be used as a prediction of the temperature distribution in a packed bed of rocks.

5.2.2 Dimensionless Parameters

The simplified Nusselt number and Reynolds number correlation used in the E-NTU method is given in equation 5.8 and equation 5.10 (Allen *et al.*, 2015).

Dimensionless parameters such as the Reynolds number and the Nusselt number are implemented to calculate the surface to air heat transfer coefficient. A representative volumetric heat transfer coefficient is produced by coupling the equivalent particle diameter D_v , surface to air heat transfer coefficient h_s , and void fraction as given in equation 5.9.

$$Nu_v = \frac{h_s D_v}{k_a} = Re_{pv}^{0.6} \quad (5.8)$$

$$h_v = h_s(1 - \varepsilon)(6/D_v) \quad (5.9)$$

$$Re_{pv} = Re_v(1 - \varepsilon) = \frac{GD_v}{\mu} \quad (5.10)$$

5.2.3 Biot Number Description

The Biot number is a definition which describes the relative importance of the convective heat transfer to/from a particle in a packed bed and conductive heat transfer in a particle. Equation 5.11 defines the Biot number as a combined function of the surface heat transfer coefficient, particle diameter and the heat conduction coefficient of the particle (Incropera *et al.*, 2007). The thermal gradient within the particle is usually considered to negligible when the Biot number is smaller than a certain threshold. Experimental work done by Allen *et al.* (2015) shows that the heat transfer correlations are valid for the particle size used in this project.

$$Bi = \frac{h_s D}{2k_r} \quad (5.11)$$

5.2.4 Energy Calculation

For energy calculations in a TES system, there must be a clear definition of how the input energy is calculated. With heat transfer in a porous medium, there are two sets of energy balances that must be considered. The energy balance of the fluid and the energy balance of the solid material involved must be in equilibrium. The solid (rock) in this case is a stationary control mass which can be seen as a closed system with no mass crossing the control boundary; however, energy can cross the control boundary in the form of an energy carrier. The fluid (air) is represented by a control volume and can be described as an open system. Being the energy carrier, the active fluid for energy calculation is seen as the fluid which is in the porous control volume of the porous medium.

Heating power of the system is defined by the amount of energy the air is putting into the porous control volume. The effective heat transfer to the rocks is defined in detail in subsection 5.2.1. The heating rate can be calculated in two ways with the available formulas used in the literature. Internal

energy and thermal energy in a fluid can be defined by the heat capacity or the enthalpy of the fluid for a specific temperature. Calculation of the heating rate for the two above mentioned methods are shown by equation 5.12 and equation 5.13. The temperature difference denoted by ΔT_f in equation 5.12 is the temperature difference between the ambient temperature and the maximum charging temperature. Enthalpy difference denoted by Δh in equation 5.13 is defined as the difference between the enthalpy value at the ambient temperature and the maximum charging temperature respectively. Heat capacity of the fluid (air) denoted by $c_{p,a}$ is taken at the average temperature between ambient conditions and the maximum charging temperature at the rock bed inlet. In the enthalpy based calculation, the different enthalpy values are taken at the maximum temperature and ambient temperature respectively.

$$\dot{Q} = \dot{m}c_{p,a}\Delta T_f \quad (5.12)$$

$$\dot{Q} = \dot{m}\Delta h \quad (5.13)$$

The energy input from the heating fluid is calculated by accumulating the energy per time step at the inlet of the packed bed. The heat capacity of the air is taken at the same temperature as the heat capacity term in equation 5.12. A constant heating rate is assumed over the charging period for the numerical model. See equation 5.14 for the description of how the energy input is calculated.

$$E_{in} = \sum_{i=0}^t \dot{m}c_{p,a(i)}\Delta T_{f(i)}\Delta t \quad (5.14)$$

The temperature distribution in the packed bed, for each computational cell is used for the energy calculation of the rock bed in a charged state. The heat transfer efficiency is defined by the amount of heat transferred from the heat transfer fluid to the rock bed in the charging period. Equation 5.16 shows the formula by which the efficiency of the heat transfer is described. The heat capacity of the rocks — $c_{p,r}$ — is defined by a temperature dependent function, where the $c_{p,r}$ value ranges between 820 J/kgK and 1190 J/kgK in the operating temperature range up to 650 °C. Energy stored in the rocks is calculated by integrating the temperature dependent function of $c_{p,r}$ to obtain the specific energy of the rocks. Heat capacity of rock as a function of temperature is given in equation 5.15, where particle temperature, T_p , is in °C (Allen *et al.*, 2015). Specific energy for each of the segments in the rock bed is multiplied with the respective mass of each segment to obtain the total stored energy when the rock bed is charged. Stored energy in the rock bed for the charged state is calculated with equation 5.17.

$$c_{p,r}(T_p) = -0.00129T_p^2 + 1.518T_p + 748 \quad (5.15)$$

$$\eta_{ht} = E_{\text{stored}}/E_{\text{in}} \quad (5.16)$$

$$E_{\text{stored}} = \sum_{i=0}^x m_{(i)} \int_{T_{\text{amb}}}^{T_{f,i}} c_{p,r}(T_{p(i)}) dT \quad (5.17)$$

Retrieval of thermal energy for the TES while the system is discharged is calculated by summing the energy in the fluid at one position at the rock bed outlet. The total thermal energy output is calculated similarly to charging energy input. This is achieved by taking the temperature difference between maximum discharging temperature and ambient conditions. The thermal properties of air is taken at the respective temperatures for calculating the total energy output. Equation 5.18

$$E_{\text{out}} = \sum_{i=0}^t \dot{m} c_{p,a(i)} \Delta T_{(i)} \Delta t \quad (5.18)$$

5.2.5 Energy Efficiency Definition

Thermal energy storage efficiency can be defined in various ways. The classical method of defining thermal efficiency of an experimental TES setup would be energy output over energy input as described in equation 5.19. For application of steam generation for a Rankine cycle, the minimum outlet temperature must remain between 327 °C and 627 °C (Hänchen *et al.*, 2011).

In a real life scenario, the usable energy is the defining factor of the system efficiency. Only the outlet air at a temperature above 327 °C is used in calculation of output energy. Equation 5.20 describes how the usable energy efficiency of this TES is defined. Figure 5.3 shows the power of the charging and discharging periods. The area below the charging part of the graph indicates the total energy input to the TES. Usable energy retrieved from the TES during discharging is indicated by the area under the discharging period of the power graph.

Stability of the thermocline in a packed bed is only achieved after the specified number of thermal cycles, depending on the geometry of the packed bed (Zavattoni *et al.*, 2015). Stability and thermal stratification is still unknown for the concept investigated in this project as partial charge—discharge experimental testing is not dealt with in the scope of this study. Energy in the TES below the temperature of 327 °C is seen as redundant energy in the TES. This redundant energy would not ideally be lost if a series of thermal storage cycles are performed. Thermal energy at a level below the temperature threshold for generating steam for a Rankine cycle would form part of the permanent thermocline in the packed bed. The number of cycles to reach a thermally stable condition is dependent on the specific geometry of the rock bed. In the case investigated in this project, the inverted thermocline has problems

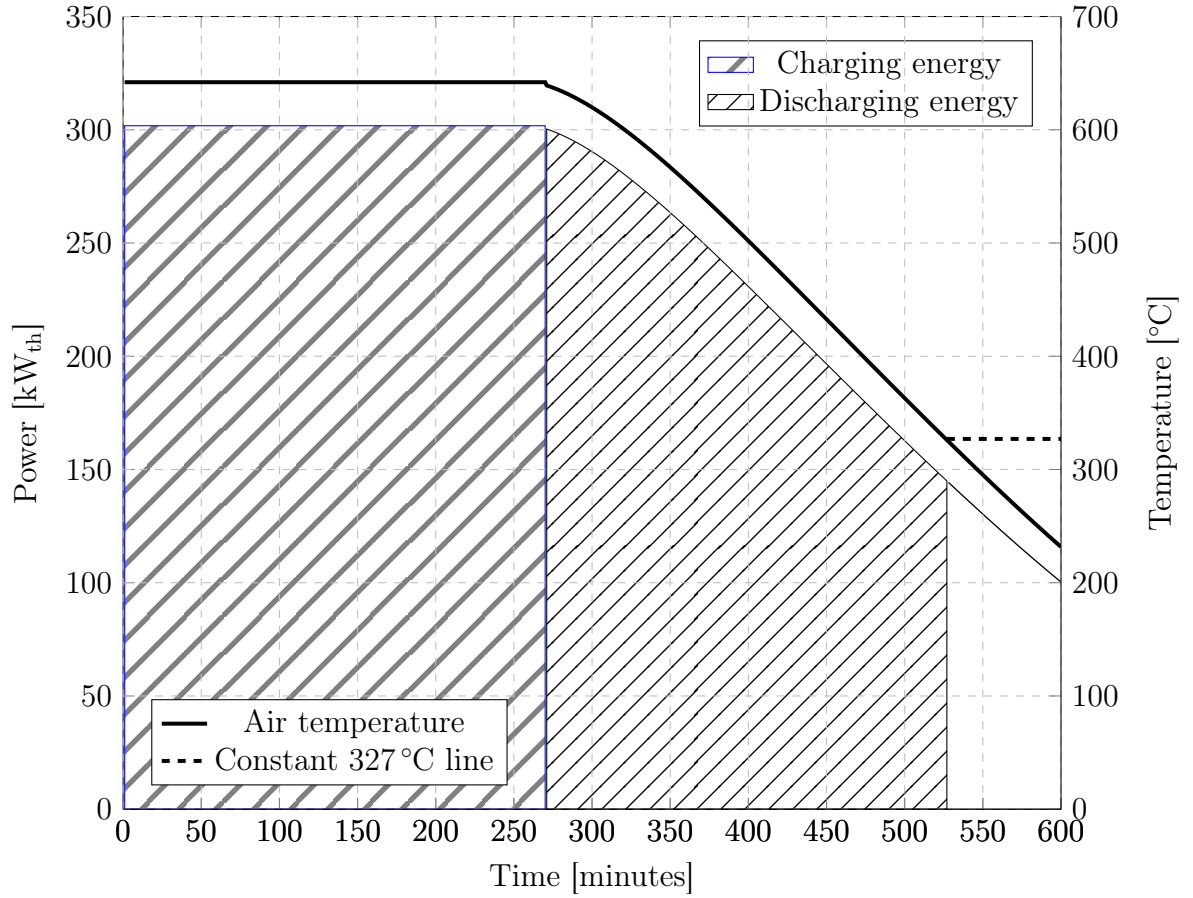


Figure 5.3: Energy distribution graph of energy stored in the rock bed over time

in maintaining a high temperature zone at the bottom centre of the rock pile while the storage is in idling mode. Buoyancy effects of the hot air cause an upward draft by means of natural convection and the stored heat in the TES is lost to the environment within a 24 hour period after a fully charged state.

$$\eta_{th,total} = E_{out}/E_{in} \quad (5.19)$$

$$\eta_{th,usable} = E_{out,usable}/E_{in} \quad (5.20)$$

5.3 Pressure Drop through Porous Media

Pressure drop in a fluid through a porous medium is dependent on various factors and the pumping power required to overcome the pressured drop is very important for this study. Correlations for calculating the pressure drop over a packed bed of rocks had been established in previous studies and the following

correlations are used to calculate the pressure drop over the test section in this project. The flow is characterized by a non-dimensional parameter, the duct Reynolds number in equation 5.21. The Reynolds number, Re_v , is directly proportional to the density of the fluid, ρ_a , and the superficial velocity of the fluid, v_s .

$$Re_v = \frac{\rho_a v_s D_v}{\mu(1 - \varepsilon)} \quad (5.21)$$

$$f_v = \frac{620}{Re_v} + \frac{13.7}{Re_v^{0.08}} \quad (5.22)$$

$$f_v = \frac{\Delta p}{\Delta x (\rho_a v_s^2 / 2)} \frac{\varepsilon^3}{(1 - \varepsilon)} D_v = f(Re_v) \quad (5.23)$$

A friction factor is calculated as a function of the Reynolds number for a particle size in the range of $0.009 < D_v < 0.049$ and a void fraction in the range of $0.38 < \varepsilon < 0.46$. Both the particle size and the void fraction ranges are applicable for the packed bed investigated in this project. Equation 5.22 is a correlation which had been established via experimental testing found in literature. The result of the friction factor from equation 5.22 is substituted in equation 5.23 and the pressure drop, Δp , for each of the sections can be calculated accordingly (Allen *et al.*, 2015). Total pressure drop over the test section is calculated by summing all the pressure drop values for all the computational segments that are in series as indicated in equation 5.24.

$$\Delta P = \sum_{i=0}^N \Delta p_{(i)} \quad (5.24)$$

5.3.1 Velocity and Density Dependence on Pressure Drop

As the cross-sectional area of the computational domain enlarges towards the outer boundary of the conical shape, the temperature decreases from the maximum charging temperature in the center of the rock pile to ambient temperature on the outer boundary. Decreasing fluid temperature causes the density of the fluid to increase and consequently the volumetric flow rate to decrease. As the volumetric flow rate decreases, the superficial velocity decreases as result of a lower volumetric flow rate and an increased cross-sectional flow area. The density and velocity terms in equation 5.21 are thus inversely proportional in the temperature domain. In previous experiments done at Stellenbosch University, it showed that for a constant cross-sectional test section, the overall pressure drop increases slightly over the charging period. This phenomenon

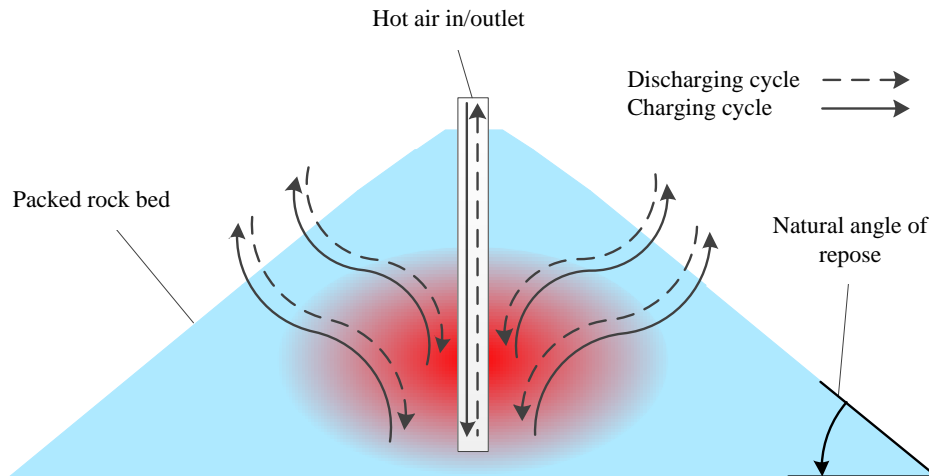


Figure 5.4: Flow diagram of the packed bed layout showing the flow direction of the fluid and the geometry of the rock bed

indicates that the effect of the increased flow velocity dominates that of the decreased density at high temperatures. This experimental facility is thoroughly described in a PhD thesis (Allen, 2014).

As the air is heated with the gas burner, the density difference between the high temperature air — at $650\text{ }^{\circ}\text{C}$ — and the air at ambient temperature causes the volumetric flow rate of the air to be at a maximum where the air is introduced into the rock bed. The smallest surface area in the porous storage media is coincident with the section in the flow where the volumetric flow rate is the highest. Refer to Figure 5.4 for the illustration of the hot spot in the bottom center of the rock bed and the conical shape of the packed bed. Here it is clear to identify the most turbulent zone in the packed bed when the system is either in charging or in discharging mode.

5.3.2 Pressure Drop Profile Over Test Section

Pressure drop in the x -direction of the test section is depicted in Figure 5.5. As shown in the pressure drop graph, the largest pressure drop occurs at the center of the packed bed. Pressure drop per segment over the positions in the rock bed is plotted to demonstrate how fast the pressure drop per segment decreases as the cross-sectional area is increasing towards the outside of the conical rock pile. The spike in pressure drop can be improved by adding larger rocks close to the center where the air is introduced to the packed bed. Increased flow area would reduce the velocity and the effective resistance of the flow through the packed bed. Another method of reducing the pressure drop would be to increase the distribution chamber to bring the overall flow velocity down.

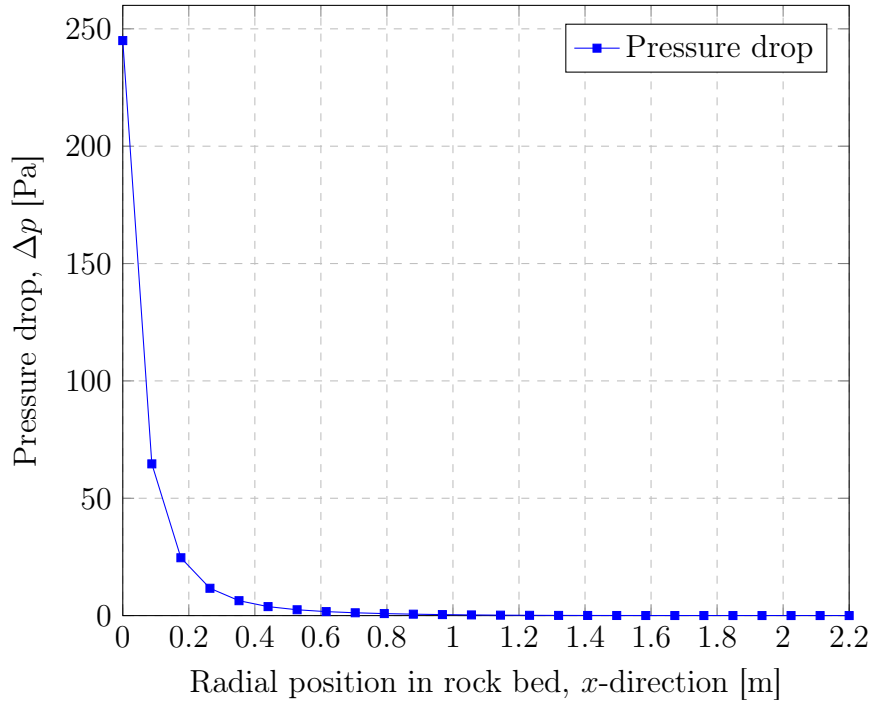


Figure 5.5: Radial pressure drop plotted for each segment at a charged state

5.4 Numerical Simulation Results

5.4.1 Heat Transfer Dimensionless Parameters

The heat transfer coefficient through the rock bed compared to the relative position can be seen in Figure 5.6. A correlation between the radial position and the heat transfer coefficient can clearly be observed. Heat transfer at the start of the charging cycle and heat transfer at the end of the charging cycle are compared in Figure 5.6. The overall heat transfer decreases as the rock bed heats up during a charging cycle. A decrease in Reynolds number, is the main reason for the decrease in the overall heat transfer coefficient as the TES heats up.

The surface heat transfer coefficient, h_s , is calculated with equation 5.8. The Reynolds number is dependent on the dynamic viscosity of the fluid, therefore a larger viscosity at higher temperatures will cause the heat transfer coefficient to decrease at elevated temperatures. The mass flux, G , is dependent on the density of the and the flow velocity in the rock bed. Heat transfer is directly proportional to the mass flux in the flow domain thus, a smaller mass flux will cause the heat transfer coefficient to decrease when the rock bed is in charging mode.

Nusselt numbers describing the flow characteristics are plotted over the radial distance of the rock bed. The dimensionless parameter provides a representative indication of how the heat transfer coefficient varies over the com-

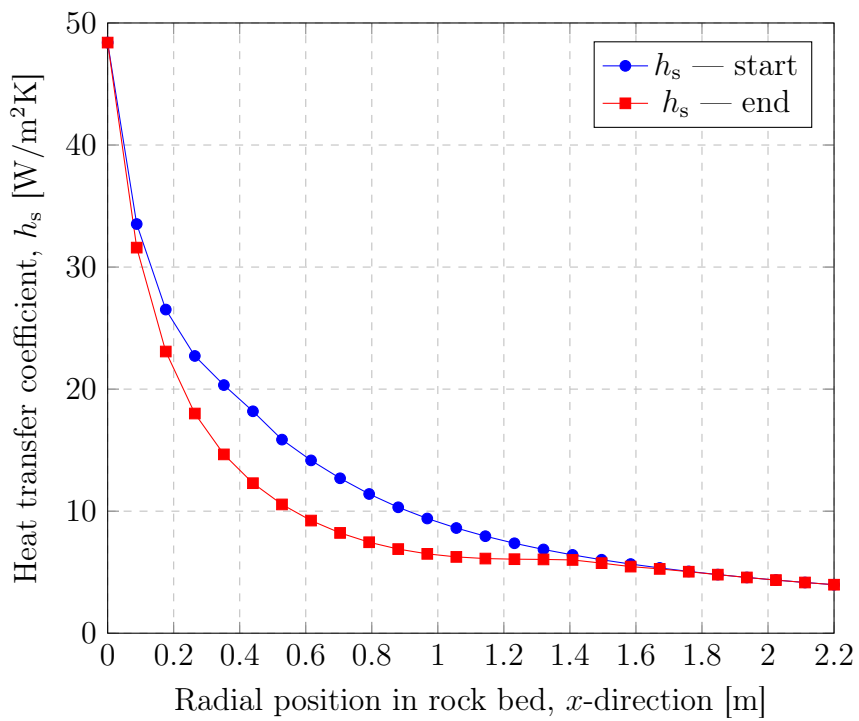


Figure 5.6: Surface heat transfer coefficient

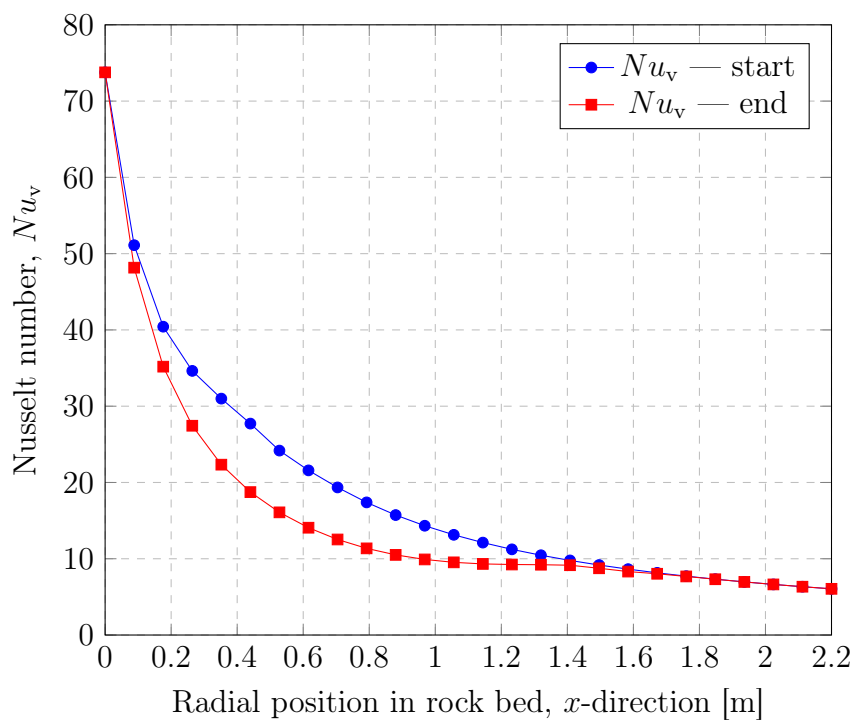


Figure 5.7: Nusselt numbers for the start and end of the charging cycle

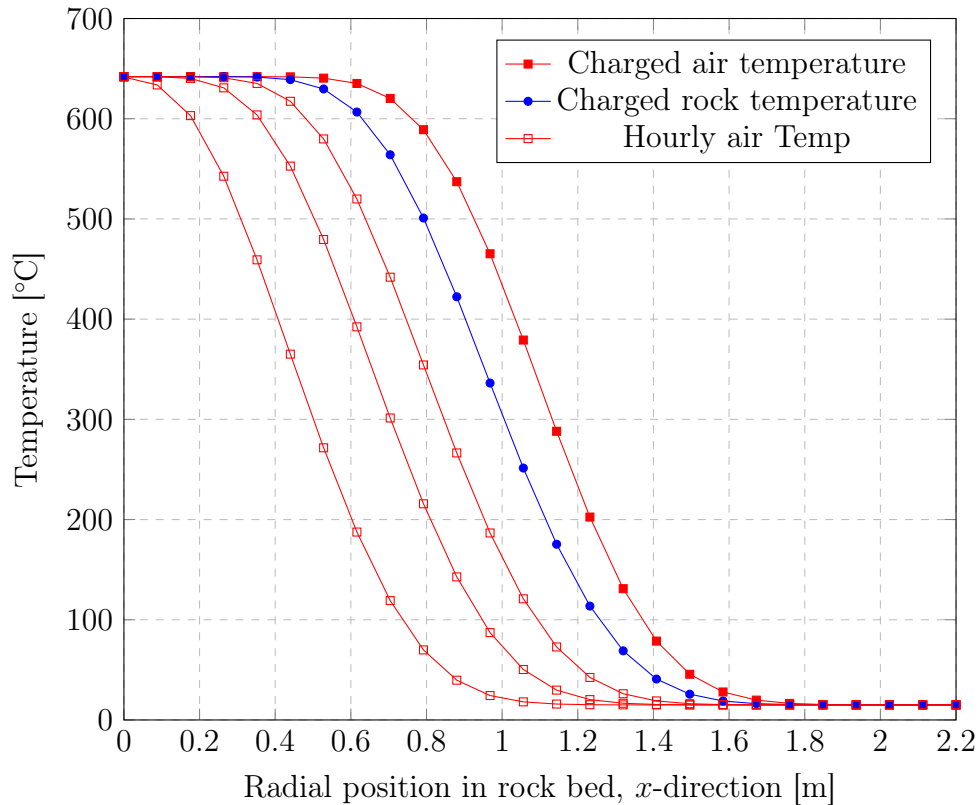


Figure 5.8: Air and rock temperatures through the rock bed

putational domain of the 1 D numerical model.

5.4.2 Temperature Distribution

The temperature distribution over the rock bed can be seen at the end of the charging cycle in Figure 5.8. The rock and air temperatures for a charged TES are plotted respectively. An hour early charging air temperature is added to show the progression of the thermocline in the TES over time. The initial state of the rocks in the TES is at ambient temperature conditions. As shown on the graph, the air outlet temperature does not exceed ambient temperature at the outlet of the rock bed at a radial distance of 2.2m. The volume of rocks up to a radial position of 0.5m in the rock bed is at a charged state of the maximum charging temperature, 642 °C.

5.4.3 Simulation Results Summary

A summary of the numerical results is presented in Table 5.1. The charging and discharging times for numerical simulation is given in hours. Energy stored in the rocks and energy recovered from the TES is given in kWh_{th}, since this is the most common units to indicate the amount of thermal energy stored in

Table 5.1: Summary of simulation results for the commissioning test

Parameter	Value	Units
Charging time	4.5	hours
Discharging time	4.28	hours
Charging capacity	318	kW _{th}
Total pressure drop over packed bed	237	Pa
Energy input	1429	kWh _{th}
Energy output	1035	kWh _{th}
Inlet air temperature	642	°C
Discharging air temperature	327 – 642	°C
Heat recovery, $\eta_{th,usable}$	72.5	%

the CSP environment. Only the usable heat recovery efficiency is given in this results section. Numerical simulation results for a thermal charge-discharge cycle based on the commissioning test charging time is presented in Table 5.1. The commissioning test was done to see how the TES performs in storing thermal energy for an extended period of time. Experimental data is therefore not available to compare to the numerical results presented in Table 5.1. Total heat retrieval efficiency from the TES is effectively 100 % for an ideal numerical model given that enough discharging time is allowed. Thermal energy in the form of hot air in the temperature range of 15 °C to 327 °C is energy that has a low exergy value. Hot air at too low temperatures cannot effectively be used and is therefore classified as redundant energy that is captured in the TES material.

Results summary for a full TES cycle with a shorter charge time period than the commissioning test is presented in Table 5.2. Heat recovery efficiency for a TES with a shorter charging period is smaller than for a TES that is charged for a longer period. Charging conditions from both simulations presented in Table 5.1 and Table 5.2 are kept constant and the only varying factor is the charging time. Ambient conditions do have an effect on the results however, for the numerical simulations, the effect of any thermal losses to the environment is omitted. Simulation results for a full TES cycle are used at a later stage to compare with the experimental results therefore, similar parameters are used for the final simulation to be comparable with the experimental results.

Table 5.2: Summary of simulation results for a full charge-discharge test

Parameter	Value	Units
Charging time	3.5	hours
Discharging time	3.27	hours
Charging capacity	318	kW _{th}
Total pressure drop over packed bed	236.5	Pa
Energy input	1112	kWh _{th}
Energy output	773	kWh _{th}
Inlet air temperature	642	°C
Discharging air temperature	327 – 642	°C
Heat recovery, $\eta_{th,usable}$	69.5	%

Chapter 6

Results and Discussion

6.1 Results

During the experimental testing data was processed and compared with the theoretical results. Figure 6.1 shows the graphs of the numerical results compared to the average experimental values. The numerically simulated temperature profile indicates that the numerical model predicts a thermocline with a slightly steeper gradient than the actual measured results. Averaged thermal gradients of experimental, numerical and CFD thermoclines are $364\text{ }^{\circ}\text{C}/\text{m}$, $474\text{ }^{\circ}\text{C}/\text{m}$ and $279\text{ }^{\circ}\text{C}/\text{m}$ respectively.

In general, the TES test facility proved to be a well functioning thermal energy storage system. The control system and all system components functioned as intended. The system behaves predictably, proved to be valuable in this project and provided valuable insight for future projects.

6.1.1 HTF Pumping Power

Pressure drop over the packed bed is a large concern for identifying the parasitic power consumption of TES in a packed bed. A total pressure drop of 236.5 Pa was numerically calculated and a measured pressure drop of 280 Pa was recorded over the packed bed during experimental testing. A summary of the pumping power consumption during testing is given in Table 6.1.

Pressure drop over the packed bed is only a small fraction, 20% of the total pressure drop in the TES system. Pumping power makes up 0.3% of the total thermal charging power of the TES, therefore the parasitic power to overcome the pressure drop is insignificantly small for this experimental test facility. The small parasitic power fraction is also a result of the simplified system layout of this experimental test facility. No heat exchangers or long air ducting are used in the system and this decreases the pressure drop of the whole system significantly. An industrial application for a TES would have resulted in much more pressure drop in the air ducting system in comparison with the experimental facility described in this thesis.

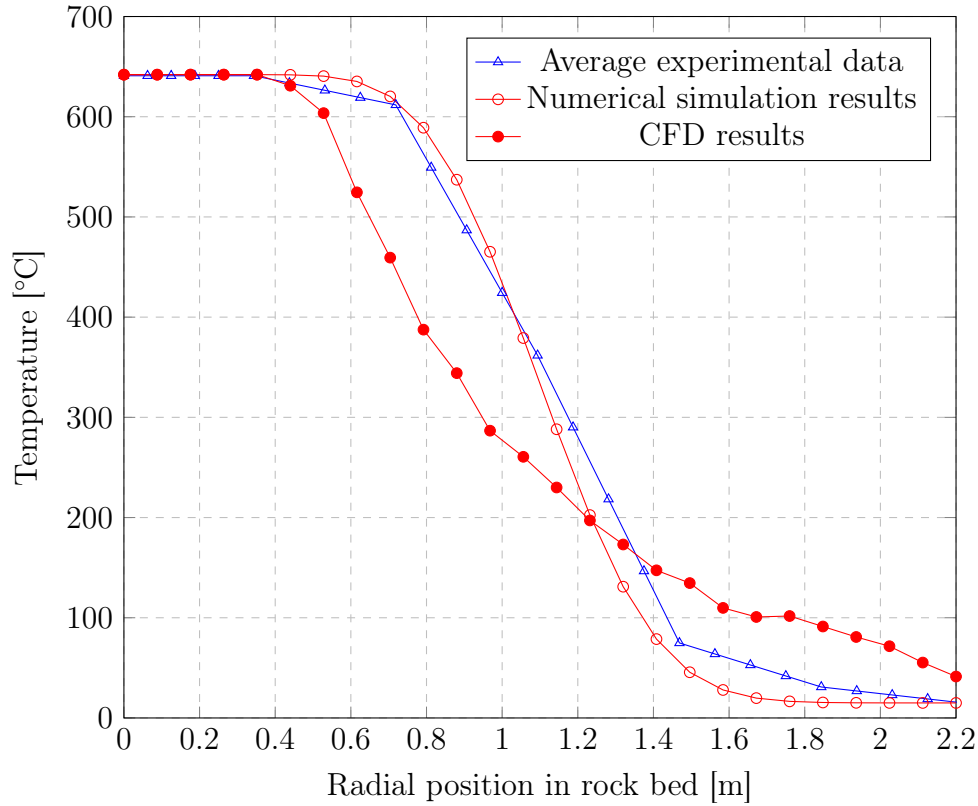


Figure 6.1: Radial air temperature; comparison between simulated and measured thermocline for the West-plane and South-plane at a charged state

Table 6.1: Pressure performance characteristics of the fan during experimental testing

Pumping performance parameter	Value	Units
Pumping power	0.9	kW_e
Max pressure	1400	Pa
Packed bed pressure drop	280	Pa
Heating power	318	kW_{th}
Packed bed pressure drop fraction	20	%
Pumping power fraction	± 0.3	%

6.1.2 Thermal Energy Distribution

Energy distribution is coincident with the temperature distribution in the rock bed. Energy stored in the rock bed at the end of the charging cycle is defined by calculating the amount of rock mass with a high thermal energy value. Temperature distribution during an idling TES move upwards in the TES and buoyancy forces are identified to be the dominating factor in the characterisation of the temperature profile when no forced convection is present. The

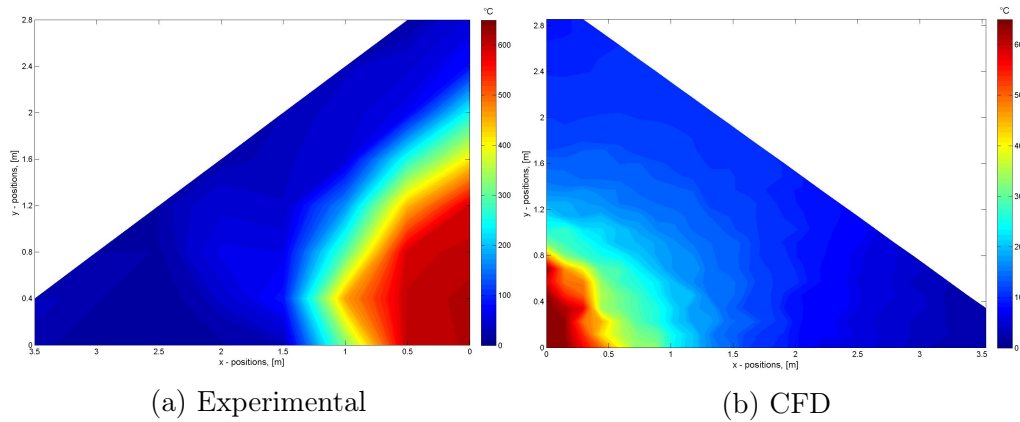


Figure 6.2: Temperature distribution contour plots for comparison of CFD and experimental results

temperature distribution that was measured during experimental testing of the TES facility and the initial predicted temperature distribution predicted by a simple CFD model can be viewed for comparison in Figure 6.2.

Modelling by means of CFD was used as a design tool and proves to offer a good prediction of the temperature distribution at the base of the packed bed for design purposes. Energy distribution in the temperature contour plot is not a good representation of the actual measured temperature distribution in the rock bed. The CFD parameters were calculated from the equivalent spherical diameter approximation as described in Appendix F. Heat transfer characteristics of the particles in an equivalent control porous volume is under predicted by making the equivalent spherical diameter approximation in the CFD model. Viscous and inertial resistance coefficients are both a function of the equivalent spherical particle diameter and is thus an approximation for calculation of resistance coefficients to use in Fluent. The approximation is based on the assumption that all the particles are uniform spherical particles and in the case investigated in this project, the particles vary in size as well as geometry. This approximation is not an accurate representation of the practical scenario described in this project, since the particle variation is too diverse to quantify accurately with a simple spherical approximation.

6.1.3 Mass Flow and Continuity

It is observed that the mass flow during a charging cycle slightly decreases for a constant frequency setting on the fan controller, as the rock bed heats up. The overall effect of the hot air with a smaller density and higher viscosity cause the flow resistance through the rock bed to increase over time as the rock bed is charged. This phenomenon indicates that the increased velocity as results of the lower density of hot air cause more turbulence in a larger effective volume of the packed bed. Higher viscosity of air at high temperatures also increase

the effective resistance of flow through the porous medium. It was observed that the overall permeability of a packed bed decreases as the TES is charging due to more turbulence in the packed bed.

6.2 Energy Recovery

Experimental results showed that the useful thermal energy recovery for the specific thermal energy storage system was 60%. Simulation results show a higher useful thermal energy recovery of 69.5%, than experimental results for the same operating conditions. The energy recovery efficiency was specifically calculated for useful energy retrieval above 327°C. The energy which was lost through thermal loss to the environment is already equated for in the experimental energy recovery efficiency number. The thermal losses should be subtracted from the simulated energy recovery efficiency to obtain a more realistic simulated number.

All energy retrieved from the TES system below a temperature of 327°C was disregarded in the energy calculation and is seen as losses in experimental work done for this project. In a utility power plant, the TES would not be fully discharged for a 24 hour cycle. For repeatable TES cycles, the low level heat (below 327°C) would typically be stored in the TES as redundant heat for the current cycle and would contribute to the energy balance of the following thermal storage cycle. The usable thermal energy recovery efficiency will increase for a system operation that makes provision for repeated charging and discharging.

6.2.1 Simulation and Experimental Results Comparison

The total of the thermal conduction losses to the soil for experimental testing is 2.2% of the total input energy, therefore 67.3% is a more realistic number to compare with experimental results. A 7.3% difference in the results obtained from experiments and simulations show that the numerical model is a good tool for predicting the thermal behaviour of a packed bed TES for this geometry. A summary of the results obtained in both the experiments and numerical simulation are listed in Table 6.2.

6.2.2 Environmental Energy Losses

Energy losses to the environment includes heat loss to the soil beneath the thermal energy storage and energy blowing through the packed bed while operating in charging mode. Thermal losses due to thermal energy lost to the soil was calculated to be less than 2.2%. The temperature distribution on the inside of the base and the measured temperature underneath the insulated base was used to calculate the thermal losses to the soil. An insignificant fraction of

Table 6.2: Results summary of the simulation and experimental results for full charge-discharge test

Design parameter	Simulated	Experimental	Units
Heating capacity	318	318	kW _{th}
Charging time	3.5	3.5	hours
Discharging time	3.27	2.75	hours
Total energy input	1112	1031	kWh _{th}
Total energy output	773	619	kWh _{th}
Heat recovery, $\eta_{th,usable}$	69.5	60	%
Packed bed pressure drop	236.5	280	Pa
Charging inlet temperature	642	638	°C
Packed bed surface temperature	15	51	°C
Minimum discharging temperature	327	327	°C
Mass flow rate	0.48	0.48	kg/s

the total energy input was conducted to the soil beneath the TES which acts as an infinite heat sink. A small amount of energy is blown through the packed bed when the system is in charging mode. According to the numerical model, no blow-through losses were calculated, as the outlet temperature of the air during charging do not go above ambient temperature. The numerical model did not make provision for thermal losses to the soil below the TES, therefore it was developed to focus solely on the heat transfer characteristics of the packed bed. The 1 D numerical model, with the same input parameters as for the experimental testing of the TES, yielded heat transfer characteristics that overestimates the heat transfer between the particles and air. The experimental testing generated results that shows the actual heat transfer characteristics are not as good as predicted by the numerical model.

6.2.3 Volume Efficiency

Overall volume efficiency of the storage material is approximately 33% of the total rock mass. This small fraction of active storage material is mainly as result of the scale of the TES constructed in this project. A much larger scale TES could yield a better volume efficiency of the storage medium in the packed bed. The TES investigated by Louw (2014) for a conical rock bed with a diameter of 150 m has a volume efficiency of up to 48.53%. The large scale TES with a 150 m diameter footprint has a similar system configuration as the TES built in this study and thus makes it a comparable reference.

The scale of the thermocline relative to the scale of the total size of the packed bed in a small scale TES facility approaches unity. In a large scale TES, the scale of the thermocline would only make out a small fraction of the total length scale of the packed bed. This is the reason why Louw found a significantly higher volume efficiency for a TES with a similar configuration.

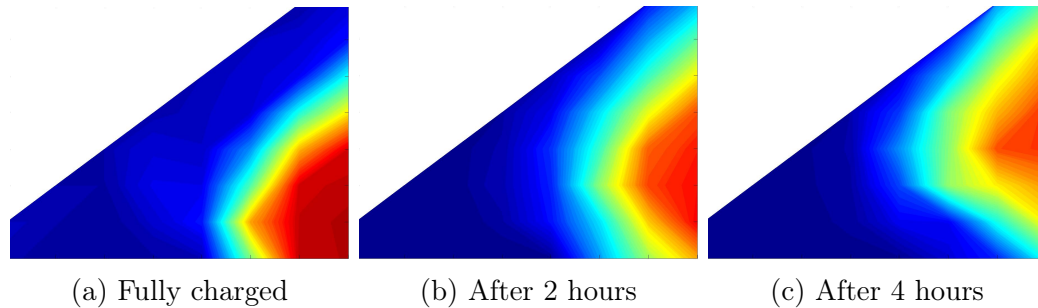


Figure 6.3: Temperature distribution of the system in idling mode

Volume efficiency of the rocks used is listed in Table 6.3. For larger concepts, the volume efficiency is predicted to increase. Better volume efficiencies can therefore be expected if a larger scale TES of this particular concept is being constructed.

6.3 System Performance Observations

6.3.1 Idling Characteristics

The concept of TES under investigation do not have a long term energy storage capability. When the TES is fully charged, it cannot stand idling for longer time periods without eventually losing all the energy to the environment, because the system is not thermally insulated. The buoyancy effect induced by the density difference between density of ambient temperature and that of hot air at approximately $600\text{ }^{\circ}\text{C}$ is the dominating factor that drives the natural convection when no forced convection is present. Idling characteristics of the TES are given in Figure 6.3. The conical rock bed concept has large thermal inertia because of the large mass of rocks. The combined effect of conduction, radiation and natural convection within the rock bed is responsible for transmitting all the energy in the bottom center of the TES to the top and escaping to the environment within a period of 24 hours.

The buoyancy effect of the hot air disqualifies this TES system to store heat for long periods and also creates a potential challenge with repeated thermal storage cycling. Longer idling was not possible, because the heat disappeared after a while due to the buoyancy effect. This is a major issue with this design.

6.3.2 Cost Effectiveness

The TES built in this project was done in the academic environment and available resources were used as far as possible. Construction labour and using of data logging equipment from Stellenbosch University are not included in the summarized cost of this TES experimental facility. A list of the various cost for capital expenditure on components is presented in Appendix G. The

Table 6.3: Storage material volume efficiency

Packed bed property	Value	Units
Total rock mass	65	tons
Heated rock mass	21.5	tons
Thermally active rock mass	43.5	tons
Volume efficiency	33	%

experimental test facility built in this study has a total cost of approximately ZAR 461 575. The rated storage capacity for this specific setup is $1.5 \text{ MWh}_{\text{th}}$. The TES test facility thus has a specific material cost of $22 \text{ USD/kWh}_{\text{th}}$. (taken that $1 \text{ USD} = 14 \text{ ZAR}$). The real cost effectiveness of the TES investigated in this study is the initial choice of the cost effective layout of a TES without insulation with an inverted thermocline.

Chapter 7

Conclusion

7.1 Conclusions

The main aim of this research project was to investigate the feasibility of a cost effective concept for TES at 600 °C that does not involve thermal insulation of the bulk storage material. A low-cost containment option is plausible, because the outer surface of the packed bed does not reach high temperatures and the containment can be constructed of inexpensive material. Numerical simulation of the TES gave results that compare well with the experimental data measured during testing. Temperature distribution through the rock bed was measured with a relative good resolution to observe the effect of buoyancy when the storage is in idling mode.

Operational strategies were designed and executed which include charging the system until the outlet air temperature goes above 50 °C and immediately discharging it. This specific experimental TES facility is inherently safe to operate only when the system is in charging or in discharging mode. An observation was made that all the energy escapes out the top of the conical rock bed when the system is in idling mode. The heat distribution at the bottom core of the TES seem to be relative stable when forced convection is the main driver for heat transfer. The moment the fan and burner are switched off, the heat front starts to plume upward and escape to the environment.

Immediate discharging of a charged system yielded a usable energy recovery efficiency of 60 %. This is a low number for usable energy recovery from a TES, taken into account this is for a single charge-discharge TES cycle. The behaviour of this packed bed TES for repeated cycles has not been tested in this study. The volume efficiency of the rocks in this TES concept is 33 % and the rest of the rock mass only serves as effective insulation and structural purpose.

Numerical simulation of the TES overall performance prove to show a good correlation with the experimentally measured results. A 7.3 % difference in the usable energy recovery efficiency for both the experimental and simulated

results shows that the model is a good representation of the experimental setup. This efficiency is a good parameter to compare as it take a lot of different factors into account. Experimental and simulated thermoclines show very good similarity over the radial direction perpendicular to the free surface of the conical pile. Experimental and numerical thermal gradients are $364\text{ }^{\circ}\text{C}/\text{m}$ and $474\text{ }^{\circ}\text{C}/\text{m}$ respectively.

Pressure drop over the packed bed is 20% of the total pressure drop in the system and pumping power is 0.3% of the total thermal charging power. Parasitic power to overcome the pressure drop in the porous medium is therefore insignificantly small.

This concept cannot be used in the CSP industry for a reliable and effective TES system, because the operations in the CSP environment sometimes require the energy to be stored for longer time periods with high thermal energy recovery. Although this is a low-cost TES concept, the low useful thermal recovery efficiency makes this a more expensive TES concept from an operations point of view and is paid for in energy.

7.2 Future Recommendations

Future research on the inverted thermocline, high temperature TES concept without insulation as described and experimentally tested in this project, is not recommended.

Due to the ineffective long term energy storage capability of this concept, an alternative system layout is recommended. Future CFD work for the packed bed concept (heat stored at the top) is recommended to obtain more accurate simulation results. Elementary CFD modelling in this project indicated that the standard porous model in Fluent under predicts the heat transfer from air to rocks. An equivalent spherical diameter approximation to characterise the non-uniform rock geometry, was identified to be part of the reason of the poor heat transfer correlations of the CFD simulations. The effect of radiation as means of heat transfer should be included in future numerical simulation for high temperature TES in a packed bed.

An adaptation of the existing TES concept to yield a more energy efficient TES option is recommended for future research. The inverted thermocline is unstable at a charged state and the heat does not remain in the TES medium. Storing the heat under an insulated roof in the top part of the TES is recommended as a design change. This would be a representation of the concept proposed by Kröger (2013).

A disadvantage of a fully insulated TES is that the capital expenditure increases, but the advantage is that thermal losses to the environment are minimized over the lifetime of the TES facility. A better thermal recovery from an insulated TES would constantly make up for the certain energy loss of a uninsulated TES, therefore, a fully insulated TES would be the better

investment in hardware. Capital expenditure on insulation would be paid once off and can be seen as a long term investment. A more expensive insulated TES could be more cost effective on the long run than a cheaper, uninsulated TES. An insulated TES would also introduce long term energy storage possibility that is not possible in the concept covered in this project. The main drive for energy storage in general in the renewable energy sector is the availability of the energy when there is a peak in demand. An insulated TES would ensure significantly more energy supply flexibility to meet fluctuating demand.

7.3 Proposed Future Design Changes

A new design concept that is similar to the layout proposed by Kröger (2013) is proposed for future research on this TES test facility. The test facility constructed in this study can be modified during follow up research to obtain a TES system layout that covers the shortcomings of the existing TES system layout.

It is proposed that insulation is installed at the top part of the TES. This adaptation to the concept would do away with the inverted thermocline and the thermal energy will thus be stored in the top region of the TES, which is fully insulated.

For an industrial scale TES, the rock bed would typically be an elongated bed that resembles an extrusion of a conical rock bed. For industrial application there would not be the constraint of having the fan strictly on the cold side of the flow, therefore an airtight containment structure is not required. Insulation does require a protective layer that would prevent the rock wool from getting wet in rainy conditions. Water degrades the rock wool material and would consequently shorten the lifetime of the insulation layer if not properly covered. A simple corrugated sheet metal roof can be installed that is both lightweight and cost effective. A lightweight structure to hold down the roof from wind loading can be simply anchored to the soil via making use of steel cabling fixed to linear concrete plinths in the soil. Due to the low cost potential, it is strongly advised to consider this adapted concept for cost effective TES in the industrial application.

Appendices

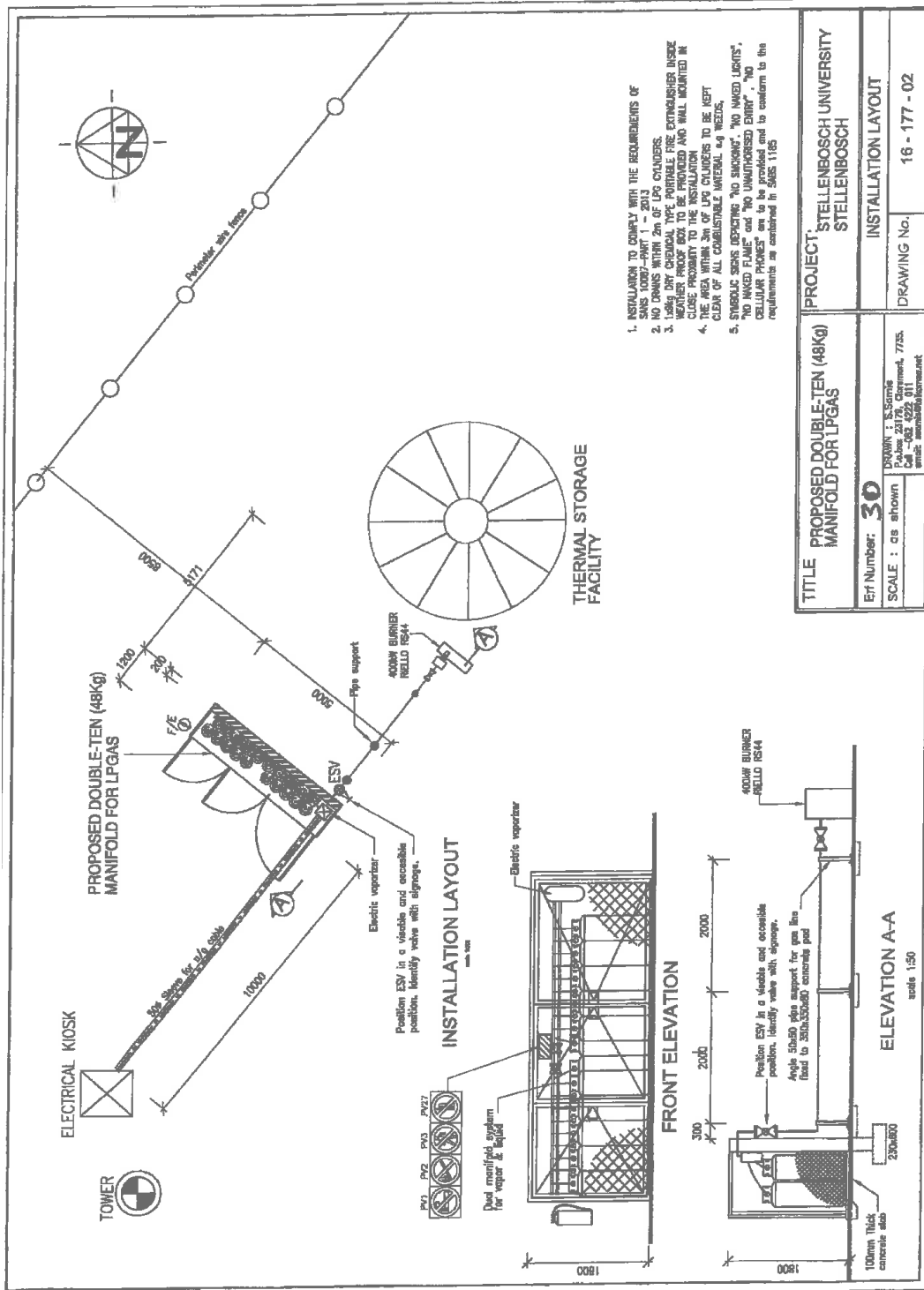
Appendix A

Official documents

Official documents for the gas installation such as gas plans, the title deeds of the construction site and approval from the local municipality are approved for the gas installation required for running the gas burner.

A certificate of compliance was issued for each of the subsystems installed. The gas train, electrical connection of the vaporizer, gas manifold, and the burner installation are all done by qualified personnel. Each service was signed off by a registered representative of the gas-supply company and all documentation is filed for future reference.

The gas plans and an overview of the hardware on site is given in the drawing following in this Appendix.



Appendix B

Material Specification

B.1 Roof Tarpaulin

Product Dimensions:

		Value	Unit	Test Method
Width	+/- 0.01	1.50	m	–
Overall Mass	+/- 20	800	g/m ²	BS 3424.5
Roll length		50	m	–

Product Properties:

			Value	Unit	Test Method
Tensile WMD		min	3200	N/50mm	BS 3424 Part 4 Method 6
AMD		min	2800		
Tear WMD		min	800	N	BS 3424 Part 5 Method 7c
AMD		min	600		
Weld Tear Strength		min	80	N/50mm	BS 3424 Part 7 Method 9b
Fusion	Acetone	min	5	min	BS 3424:22
	Ethyl Acetate	min	10	min	
Flex Cracking		min	250000	Cycles	SABS 411

Base Fabric Properties:

Composition	Polyester	100%		
Fabric mass per unit area	min.	230		SANS 79
Linear Density (Warp)		1100d/dTex		BS 3424
Linear Density (Weft)		1100d/dTex		BS 3424
Thread per centimetre (Warp)	min.	11		SANS 86
Thread per centimetre (Weft)	min.	12		SANS 86
Weave				

Figure B.1: Tarpaulin cover material specifications

B.2 Tarpaulin Cover Drawing

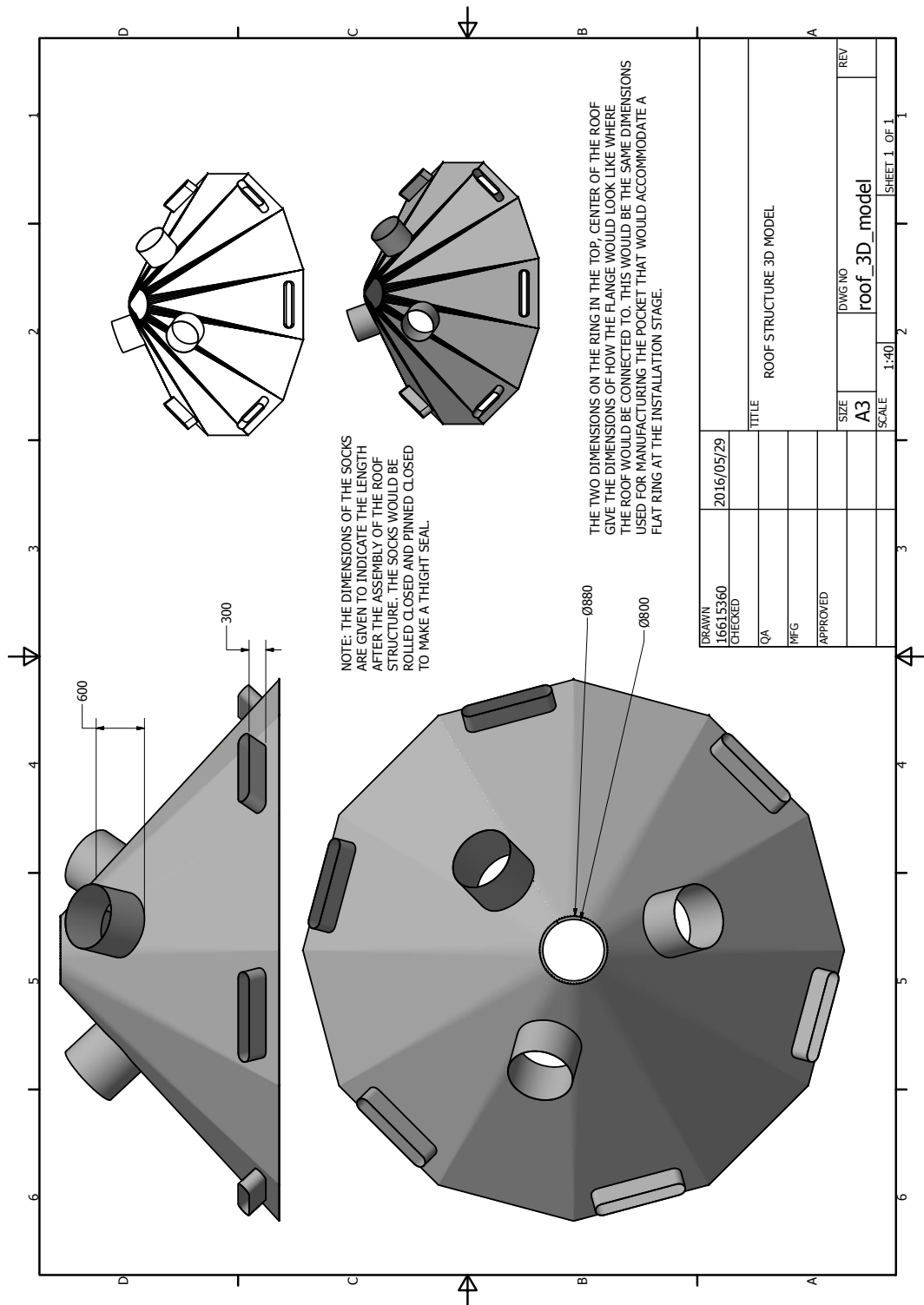


Figure B.2: Tarpaulin cover drawing indicating the position of the ventilation holes

B.3 Ducting Stainless Steel Specification

P R O D U C T D A T A S H E E T

409

STAINLESS STEEL

UNS S40920



AK Steel

AK Steel 409 Stainless Steels are especially useful for applications where oxidation or corrosion protection beyond the capacity of carbon steel and some coated steels is needed. Current applications include automotive and truck exhaust systems, including tubular manifolds; agricultural spreaders, gas turbine exhaust silencers, and heat exchangers. AK Steel 409 Stainless Steels are also useful for "difficult-to-form" hardware such as fuel filters.

COMPOSITION

	ASTM A 240 UNS S40920 %	AK Steel 409 %
Carbon	0.03 max	0.02 max
Manganese	1.00 max	0.75 max
Phosphorus	0.040 max	0.040 max
Sulfur	0.02 max	0.020 max
Silicon	1.00 max	1.00 max
Chromium	10.50 - 11.70 max	10.50 - 11.70
Nickel	0.50 max	0.50 max
Nitrogen	0.03 max	0.02 max
Titanium	8x(C+N) min 0.15 - .50	8x(C+N) min 0.15 - .50

AVAILABLE FORMS

AK Steel produces 409 stainless in coils and cut lengths in thicknesses 0.015" to 0.250" in widths up to and including 48". For welded applications over 0.120" thick, AK Steel Type 409 Ni Stainless Steel will provide improved toughness and weldability.

MECHANICAL PROPERTIES

Typical Mechanical Properties (Annealed Condition)

	ASTM A 240 UNS S40920	AK Steel 409 0.040" - 0.070"
Ultimate Tensile Strength, ksi	55 min	60-68
0.2% Yield Strength, ksi	25 min	35-41
Elongation, % in 2"	20 min	31-39
Hardness, Rockwell	B88 max	B66-B72

Properties Acceptable for Material Specification 0.041" to 0.075"

UTS, ksi	55 min
0.2% YS, ksi	30 min
Elongation, % in 2"	25 min
Hardness, Rockwell	B76 max

PHYSICAL PROPERTIES

Density, lb/in ³	0.280
Specific Electrical Resistance microhm-cm	60.0
Modulus of Elasticity in Tension psi	30.2 x 10 ⁶

CORROSION RESISTANCE

In general, the corrosion resistance of 409 stainless is about the same as Type 410 stainless steel. This is confirmed by standard and special corrosion tests, as well as extensive service experience. Tests also have been conducted to simulate exhaust system conditions. The results show 409 to be better than coated carbon steels, but worse than 18 Cr stainless steels in these engine condensate tests.

Corrosion resistance of welds and weld areas is nearly comparable to that of the base metal. In this respect, AK Steel

409 stainless is superior to Type 410 stainless steel because welding does not greatly impair the corrosion resistance of weld areas prone to chromium carbide sensitization.

AK Steel 409 Stainless Steels contain a certain number of surface inclusions which are the normal result of titanium stabilization additions to improve the steel. Occasionally, rusting may occur at these inclusion sites and lead to problems with cosmetic appearance. As a result, these steels are not suggested for applications where surface appearance is a factor. In cases where surface appearance is important, 400 stainless steels should be considered.

OXIDATION RESISTANCE

The temperature at which 409 starts to exhibit destructive scaling in air is approximately 1450°F (789°C). This is considered the general maximum service temperature for continuous exposure in air. However, maximum service temperatures will vary appreciably, depending on the atmospheres involved.

FABRICATION

409 stainless provides good fabricating characteristics and can be cut, blanked and formed without difficulty. Stainless steels provide fabricating characteristics that are much improved when compared to standard ASTM A 240 Type 409 stainless steel. Brakes and presses used normally on carbon steel can be used on 409 stainless.

409-S-8-01-07

Figure B.3: Stainless steel 409 engineering specifications

AK STEEL

409 STAINLESS STEEL DATA SHEET

Forming practices indicate that sheet 0.050" to 0.187" requires a minimum bend radius equal to the metal thickness, 1T; and material over 0.187", a radius of 1-1/2 T.

Standard forming tests show a typical Olsen Cup Height value of 0.400" and a Limiting Draw Ratio of 2.20 for AK Steel 409 Stainless Steels.

At times, the ability to form 409 stainless has been affected by temperature – in particular ductile-to-brittle transition temperatures (DBTT). AK Steel 409 Ni Stainless Steel offers improved resistance to brittle impact fractures at lower temperatures. The DBTT for hot-rolled 0.200" thick material is below -20°F, while after cold rolling to 0.075" thick material and annealing, the DBTT is below -75°F.

These steels offer benefits in tubing applications. Using an AK Steel 409 Stainless Steels analysis notably improved levels of formability in exhaust tubing in the as-high frequency welded condition.

The plastic strain ratio or r_m (\bar{r}) value may be thought of as a material's resistance to thinning during drawing or tube bending operations. The higher the value, the greater the resistance to tearing or thinning. AK Steel 409 Stainless Steels have a typical r_m (\bar{r}) value of 1.1 to 1.7.

WELDING

AK Steel 409 Stainless Steels are readily welded by arc welding processes. When gauge thickness and weld joint

geometry permit the use of gas shielded metal-arc welding, joints having good properties are easily obtained. The electrode wire most often suggested is an AWS ER309 or ER308L austenitic stainless steel when the applications do not include exposure to high temperatures. AWS ER309 or ER308L stainless wire may also be employed for joining 409 stainless to mild steel. Thin wall components for elevated-temperature service should be weld fabricated with a matching weld filler such as 409 Cb. AWS ER430 and W18 Cr-Cb filler wires are suitable alternatives.

Guidelines for the Shielded Metal-Arc (SMA) process and selection of electrodes are about the same as those employed for GMA and GTA welding, except that matching fillers for thermal application are not available in covered electrode form. Suitable substitutes are E410NiMo and E360.

409 stainless is readily adaptable to resistance spot and seam welding.

TEMPERATURE PROPERTIES

Elevated-Temperature Fatigue Strength (Tension/Tension R=0.1)

Temperature °F	°C	Fatigue Strength to Surpass 10 ⁷ Cycles ksi (MPa)
70	21	47 (324)
700	371	45 (310)
1100	593	17.0 (117)
1300	704	5.0 (34)
1500	816	1.5 (10)

Stress Rupture Properties
0.045" – 0.060" (1.14 – 152 mm)

Temperature	Maximum Stress to Failure, ksi (MPa)	
	°F	°C
1300	704	4.1 (27.5)
1500	816	1.5 (10.3)
		1000 HRS
		1000 HRS

SPECIFICATIONS

AK Steel 409 Stainless Steels are covered by specification ASTM A 240/A 240M. It is suggested that the issuing agency be contacted for the latest revision of the specification.

METRIC CONVERSION

Data in this publication are presented in U. S. customary units. Approximate metric equivalents may be obtained by performing the following calculations:

Length (inches to millimeters) –
Multiply by 25.4

Strength (ksi to megapascals or
meganewtons per square meter) –
Multiply by 6.8948

Temperature (Fahrenheit to Celsius) –
(°Fahrenheit - 32) Multiply by 0.5556

Density (pounds per cubic inch to
kilograms per cubic meter) –
Multiply by 27,670

The information and data in this product bulletin are accurate to the best of our knowledge and belief, but are intended for general information only. Applications suggested for the materials are described only to help readers make their own evaluations and decisions, and are neither guarantees nor to be construed as express or implied warranties of suitability for these or other applications.

Data referring to mechanical properties and chemical analyses are the result of tests performed on specimens obtained from specific locations of the products in accordance with prescribed sampling procedures; any warranty thereof is limited to the values obtained at such locations and by such procedures. There is no warranty with respect to values of the materials at other locations.

AK Steel and the AK Steel logo are registered trademarks of AK Steel Corporation.



Customer Service 800-331-5050

AK Steel Corporation
9227 Centre Pointe Drive
West Chester, OH 45069

www.aksteel.com



7100-0096 PDF 7/07

© 2007 AK Steel Corporation

Figure B.4: Stainless steel 409 engineering specifications, continued

B.4 High Temperature Gasket Material



Cape Refractory Industries

a division of National Refractory Industries (Pty) Ltd

Reg. No. 71/05877/07

CAPE TOWN:
34 Gemini Street, Brackenfell, 7560
P.O. Box 213, CapeGate, 7562
Tel: (021) 982 7484 Fax: (021) 982 7477
E-mail: cri@mweb.co.za

DURBAN:
74 Hime Lane, Jacobs
P.O. Box 12314, Jacobs 4026
Tel: (031) 468 1474 Fax: (031) 468 5458
E-mail: nrdbn@iafrica.com

RICHARDS BAY:
7 Ohmzone, Alton
P.O. Box 1570, Richards Bay 3900
Tel: (035) 797 3366 Fax: (035) 797 3957
E-mail: nrb@iafrica.com

Ceramic Fiber Board

Product name		Ceramic fiber machine-process board			Ceramic fiber flame shield board	
Classification temperature (°C)		1260		1400	1260	1400
Product code		QDSD-234	QDSD-334	QDSD-534	QDSD-364D	QDSD-464D
Shrinkage on heating (%)		1000°C × 24h ≤ -3	1100°C × 24h ≤ -3	1350°C × 24h ≤ -3	1100°C × 24h ≤ -3	1200°C × 24h ≤ -3
Thermal conductivity (W/mK)	@ 200°C	0.065-0.085		0.070-0.090	0.103	
	@ 400°C	0.095-0.112		0.110-0.125	0.125	
	@ 600°C	0.145-0.165		0.155-0.175	0.151	
dampish rate (%)		≤ 1				
Organic Content (%)		≤ 5				
Density (kg/m ³)		300/320/340			320	
specification (mm)		1200/900 × 1000/500 × 13/20/25/50			800/900 × 600/700 × 25/30/40/50	
Package		Plastic bag inside, paper carton outside				
Quality and environmental system authentication		ISO9001-2000 ,ISO14001-1996				

Figure B.5: Ceramic fibre board specifications

B.5 Wall Sections

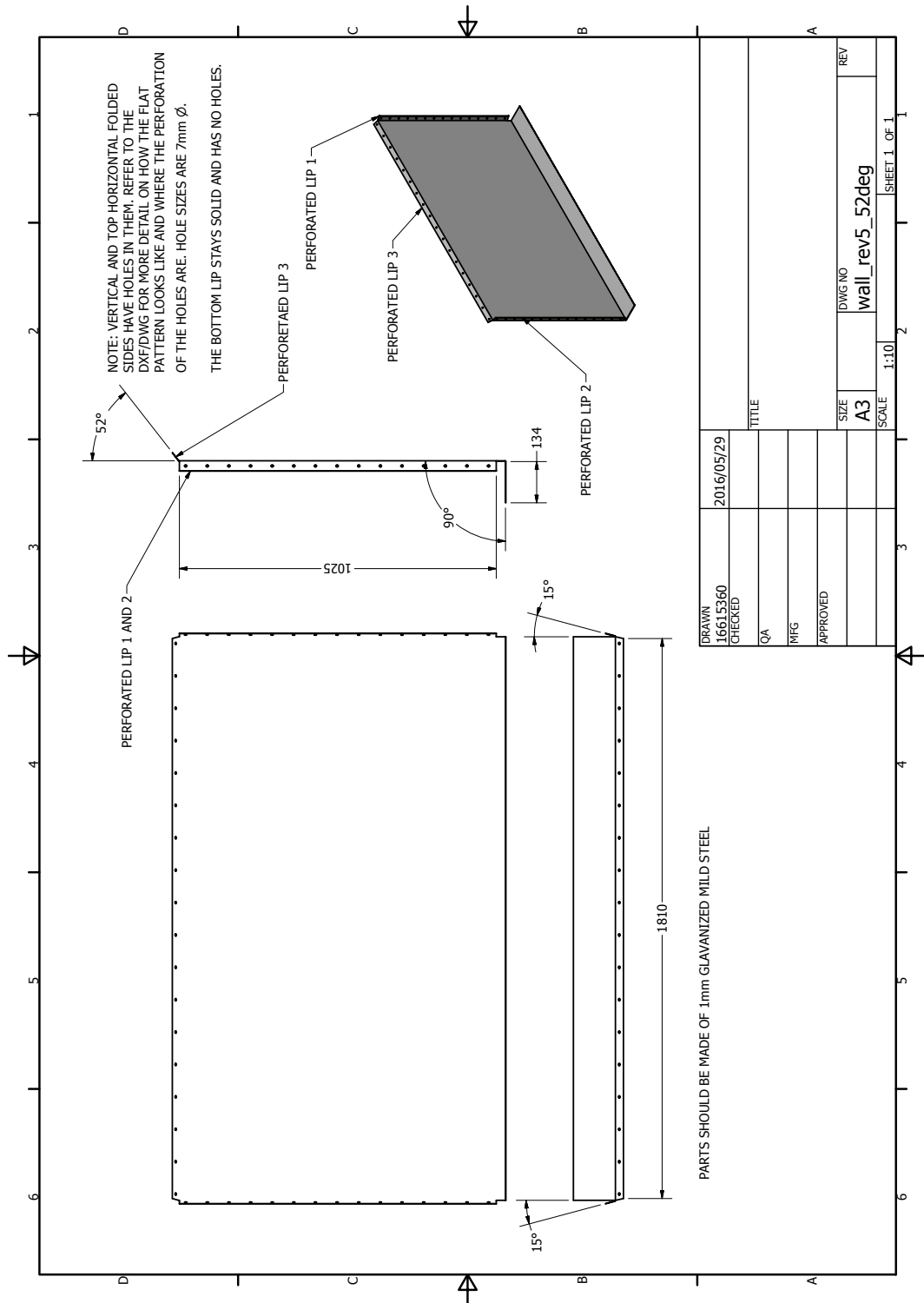


Figure B.6: CAD drawing of a sheet metal wall section

Appendix C

Ducting Pressure Drop Calculations

Hot air ducting pressure drop

$$\text{pipe_length} := 7.5 \text{ m}$$

$$L_{p_250} := \text{pipe_length} = 7.5 \text{ m}$$

total length of piping at high 650 °C

$$\rho_{\text{air_650}} := 0.3829 \frac{\text{kg}}{\text{m}^3}$$

density of at the hottest scenario, 650 °C

$$\varepsilon_{\text{surface}} := 0.15 \text{ mm}$$

$$D_{250} := 0.25 \text{ m}$$

hot ducting diameter

$$\text{Vol}_{\text{hot}} := 1.5 \frac{\text{m}^3}{\text{s}}$$

rated volume flow rate for hot side

$$A_{250\text{mm}} := \pi \cdot \left(\frac{D_{250}}{2} \right)^2 = 0.0491 \text{ m}^2$$

$$V_{\text{avg_250}} := \frac{\text{Vol}_{\text{hot}}}{A_{250\text{mm}}} = 30.5577 \frac{\text{m}}{\text{s}}$$

$$\mu_{\text{air_650}} := \left(3.956 \cdot 10^{-5} \right) \frac{\text{kg}}{\text{m s}}$$

$$\text{Re}_{250} := \frac{\left(V_{\text{avg_250}} \cdot D_{250} \right)}{\frac{\mu_{\text{air_650}}}{\rho_{\text{air_650}}}} = 73941.8739$$

$f_{250} := 0.0216$ initial friction factor guess

```

for j ∈ 1..500
  LH := 1 / sqrt(f_250)
  RH := -2 * log_10 ( ( 2.51 / ( Re_250 * sqrt(f_250) ) + ( epsilon_surface / D_250 ) / 3.7 ) )
  if LH > RH
    f_250 := f_250 + 0.000001
  else
    f_250 := f_250 - 0.000001

```

from Colebrook equation, Cengel & Cimbala page : 361 and 934

$f_{250} = 0.0216$ $RH = 6.8104$ $LH = 6.8106$

$$\Delta P_{250_hot} := \frac{f_{250} \cdot L_{p_250} \cdot \rho_{air_650} (V_{avg_250})^2}{(D_{250})^2} = 115.6294 \text{ Pa}$$

Pressure drop for the straight pipe sections 250 mm diameter.

$L_{p_450} := 1.5 \text{ m}$ combustion chamber length

$D_{450} := 0.45 \text{ m}$ combustion chamber length

$$A_{450mm} := \pi \cdot \left(\frac{D_{450}}{2} \right)^2 = 0.159 \text{ m}^2$$

$$V_{avg_450} := \frac{Vol_{hot}}{A_{450mm}} = 9.4314 \frac{\text{m}}{\text{s}}$$

$$Re_{450} := \frac{(V_{avg_450} \cdot D_{450})}{\frac{\mu_{air_650}}{\rho_{air_650}}} = 41078.8188$$

$f_{450} := 0.022$ $f_{450} =$ initial friction factor guess

```

for j ∈ 1..500
  LH := 1 / sqrt(f_450)
  RH := -2 * log_10 ( ( 2.51 / ( Re_450 * sqrt(f_450) ) + ( epsilon_surface / D_450 ) / 3.7 ) )
  if LH > RH
    f_450 := f_450 + 0.00001
  else
    f_450 := (f_450 - 0.00001)

```

For loop iteration to find the friction factor in the implicit Colebrook equation.

$f_{450} = 0.0229$ $RH = 6.6123$ $LH = 6.6125$

$$\Delta P_{450_hot} := \frac{f_{450} \cdot L_{p_450} \cdot \rho_{air_650} (V_{avg_450})^2}{(D_{450})^2} = 1.2988 \text{ Pa}$$

Reducing, hot ducting

$$K_{L_cone} := 0.02 \quad \text{loss coefficient for reducing with } 30^\circ \text{ total angle}$$

$$\Delta P_{\text{reducing}} := \frac{K_{L_cone} \cdot V_{\text{avg_250}}^2 \cdot \rho_{\text{air_650}}}{2} = 3.5754 \text{ Pa}$$

Crabtail bend losses

$$K_{45} := 0.4$$

$$K_{\text{bend}} := K_{45} \cdot 3 = 1.2$$

$$\Delta P_{\text{bend}} := \frac{K_{\text{bend}} \cdot V_{\text{avg_250}}^2 \cdot \rho_{\text{air_650}}}{2} = 214.5257 \text{ Pa}$$

$$\Delta P_{\text{hot}} := \Delta P_{450 \text{ hot}} + \Delta P_{250 \text{ hot}} + \Delta P_{\text{reducing}} + \Delta P_{\text{bend}} = 335.0293 \text{ Pa}$$

hot pipe pressure losses

Cold air ducting pressure dropOutlet straight pipe

$$L_{p_200} := 4.6 \text{ m}$$

geometry parameters of 200 mm diameter cold ducting

$$D_{200} := 0.2 \text{ m}$$

$$Vol_{\text{cold}} := 0.5 \frac{\text{m}^3}{\text{s}}$$

Volumetric flow rate at the cold side of the ducting

$$\mu_{\text{air_20}} := 1.9137 \cdot 10^{-5} \frac{\text{kg}}{\text{m s}}$$

air properties at 20 °C

$$\rho_{\text{air_20}} := 1.2104 \frac{\text{kg}}{\text{m}^3}$$

$$A_{200\text{mm}} := \pi \cdot \left(\frac{D_{200}}{2} \right)^2 = 0.0314 \text{ m}^2$$

$$V_{\text{avg_200}} := \frac{Vol_{\text{cold}}}{A_{200\text{mm}}} = 15.9155 \frac{\text{m}}{\text{s}}$$

$$Re_{200} := \frac{(V_{\text{avg_200}} \cdot D_{200})}{\frac{\mu_{\text{air_20}}}{\rho_{\text{air_20}}}} = 2.0133 \cdot 10^5$$

$$f_{200} := 0.018$$

f₂₀₀ = initial friction factor guess

```

for j ∈ 1..500
  LH := 1 / sqrt(f_200)
  RH := -2 * log10( ( (epsilon_surface / D_450) / (Re_200 * sqrt(f_200)) ) )
  if LH > RH
    f_200 := f_200 + 0.000002
  else
    f_200 := (f_200 - 0.000002)

```

$$f_{200} = 0.0179 \quad RH = 7.4738 \quad LH = 7.4739$$

$$\Delta P_{200_cold} := \frac{\left(f_{200} \cdot L_{p_200} \cdot \rho_{air_20} \cdot (V_{avg_200})^2 \right)}{(D_{200})^2} = 63.1273 \text{ Pa}$$

Pressure drop at the accumulator

$$K_{accumulator} := 0.5$$

Cengel & Cimbala p.367

$$\Delta P_{acc} := \frac{K_{accumulator} \cdot V_{avg_200}^2 \cdot \rho_{air_20}}{2} = 76.6495 \text{ Pa} \quad \text{minor loss at accumulator}$$

Valve losses

$$K_{valve} := 2$$

$$\Delta P_{valve} := \frac{K_{valve} \cdot V_{avg_200}^2 \cdot \rho_{air_20}}{2} = 306.5979 \text{ Pa}$$

$$\Delta P_{valves} := \Delta P_{valve} \cdot 2 = 613.1958 \text{ Pa}$$

Burner box inlet and outlet pressure losses

$$K_{in} := 1.05 \quad K_{out} := 0.5$$

$$V_{avg_450} = 9.4314 \frac{m}{s}$$

$$\Delta P_{bbox_in} := \frac{K_{in} \cdot V_{avg_200}^2 \cdot \rho_{air_20}}{2} = 160.9639 \text{ Pa}$$

$$\Delta P_{bbox_out} := \frac{K_{out} \cdot (V_{avg_450})^2 \cdot \rho_{air_20}}{2} = 26.9167 \text{ Pa}$$

$$\Delta P_{bbox} := \Delta P_{bbox_out} + \Delta P_{bbox_in} = 187.8806 \text{ Pa}$$

$$\Delta P_{cold} := \Delta P_{acc} + \Delta P_{valves} + \Delta P_{bbox} = 877.7259 \text{ Pa}$$

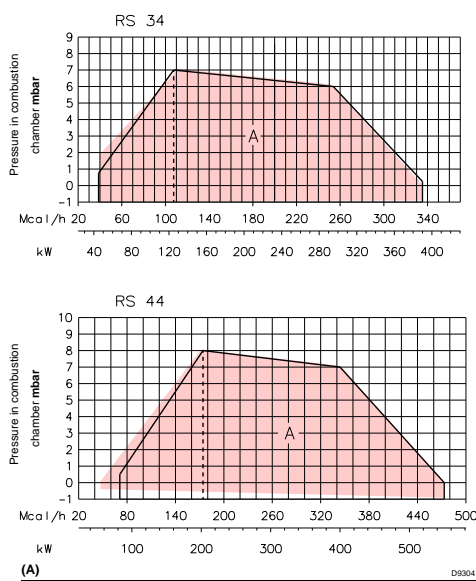
cold pipe pressure losses

$$\Delta P_{total} := \Delta P_{hot} + \Delta P_{cold} = 1212.7552 \text{ Pa}$$

Appendix D

Equipment

D.1 Burner Combustion Chamber Sizing



FIRING RATES (A)

During operation, burner output varies between:

- a **MAXIMUM OUTPUT**, selected within area A.
- and a **MINIMUM OUTPUT**, which must not be lower than the minimum limit in the diagram.

RS 34 MZ = 45 kW
RS 44 MZ = 80 kW

Attention

The FIRING RATE values have been obtained considering an ambient temperature of 20 °C, a barometric pressure of 1013 mbar (approx.0m above sea level) and with the combustion head adjusted as shown on page 8.

TEST BOILER (B)

The firing rates were set in relation to special test boilers, according to EN 676 regulations. Figure (B) indicates the diameter and length of the test combustion chamber.

Example

Output 350 Mcal/h:
diameter = 50 cm; length = 1.5 m.

COMMERCIAL BOILERS

The burner/boiler combination does not pose any problems if the boiler is CE type-approved and its combustion chamber dimensions are similar to those indicated in diagram (B). If the burner must be combined with a commercial boiler that has not been CE approved and/or its combustion chamber dimensions are clearly smaller than those indicated in diagram (B), consult the manufacturer.

In addition, for inversion boilers you are advised to check the length of the combustion head, as indicated by the boiler manufacturer.

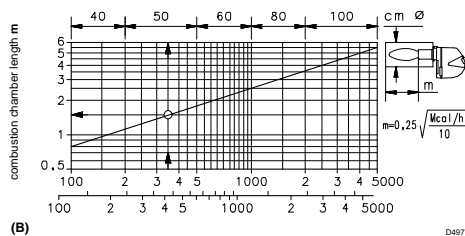


Figure D.1: Combustion chamber sizing specification sheet

D.2 Burner Heating Capacity

TECHNICAL DATA



MODEL		RS 34/M MZ	RS 44/M MZ	RS 44/M MZ	
TYPE		874 T		875 T	
OUTPUT (1)	MAX.	125 - 390 108 - 336		203 - 550 175 - 473	
	MIN.	45 39		80 69	
FUEL		NATURAL GAS: G20 - G21 - G22 - G23 - G25			
		G20	G25	G20	G25
- net calorific value	kWh/Sm ³	9.45	8.13	9.45	8.13
	Mcal/Sm ³	8.2	7.0	8.2	7.0
- absolute density	kg/Sm ³	0.71	0.78	0.71	0.78
- max. delivery	Sm ³ /h	41	48	58	67.6
- pressure at max. delivery (2)	mbar	13.1	18.4	16.7	23.2
OPERATION		<ul style="list-style-type: none"> On-Off (1 stop min each 24 hours). Progressive two-stage or modulating by kit (see ACCESSOIRES). 			
STANDARD APPLICATIONS		Boilers: water, steam, diathermic oil			
AMBIENT TEMPERATURE		0 - 40 °C			
COMBUSTION AIR TEMPERATURE		°C max 60			
ELECTRICAL SUPPLY		230 ~ +/-10% 50/60 - single-phase		230 - 400 with neutral ~ +/-10% 50/60 - three-phase	
ELECTRIC MOTOR	rpm	2800		2780	
	W	300		450	
		220 - 240		220/240-380/415	
ACCELERATION CURRENT		15 A		17 A	
WORKING CURRENT		3.2 A		3.5 A	
MOTOR CAPACITOR		12.5/260 µF/V		12.5/420 µF/V	
IGNITION TRANSFORMER		V1 - V2 230 V - 1 x 15kV I1 - I2 1 A - 25mA			
ELECTRICAL POWER CONSUMPTION		W max 600		700	
ELECTRICAL PROTECTION		IP40			
IN CONFORMITY WITH EEC DIRECTIVES		90/396 - 89/336 - 2004/108 - 73/23 - 2006/95 - 2006/42			
NOISE (3)	SOUND PRESSURE	68 dBA		70 dBA	
	SOUND POWER	79 dBA		81 dBA	
APPROVAL		EC 0085BR0378		0085BR0378	

(1) Reference conditions: Room temperature 20°C - Gas temperature 15°C - Barometric pressure 1013 mbar - Altitude 0m above sea level.

(2) Socket pressure 7)(A)p.4 with zero pressure in the combustion chamber.

(3) Noise emission tests carried out as specified in EN 15036-1 with measurement accuracy $\sigma = \pm 1.5$ dB, in the manufacturer's combustion chamber with burner operating on test boiler at maximum output.

STRUCTURAL VERSIONS

Model	ELECTRICAL POWER SUPPLY	BLAST TUBE LENGTH mm
RS 34/M MZ	single-phase	216
	single-phase	351
RS 44/M MZ	single-phase	216
	single-phase	351
	three-phase	216
	three-phase	351

GAS CATEGORIES

COUNTRY	CATEGORY
IT - AT - GR - DK - FI - SE	I ₂ H3B/P
ES - GB - IE - PT	I ₂ H3P
NL	I ₂ L3B/P
FR	I ₂ E3P
DE	I ₂ ELL3B/P
BE	I ₂ E(R)B, I ₃ P
LU	I ₂ E 3B/P

Figure D.2: Riello burner technical data

D.3 Burner Control Diagram

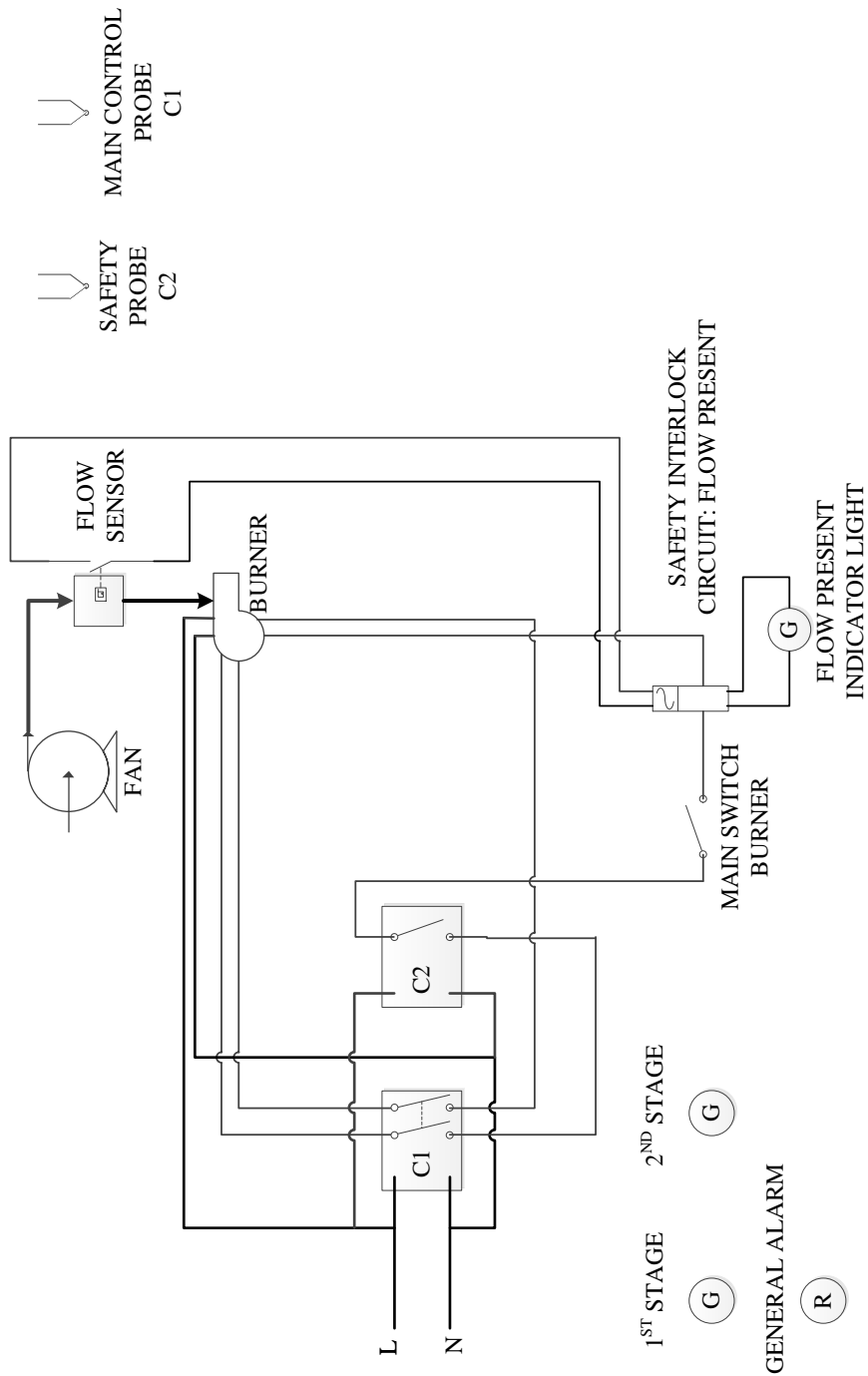


Figure D.3: Burner control circuit diagram

D.4 Flame Containing Nozzle Design

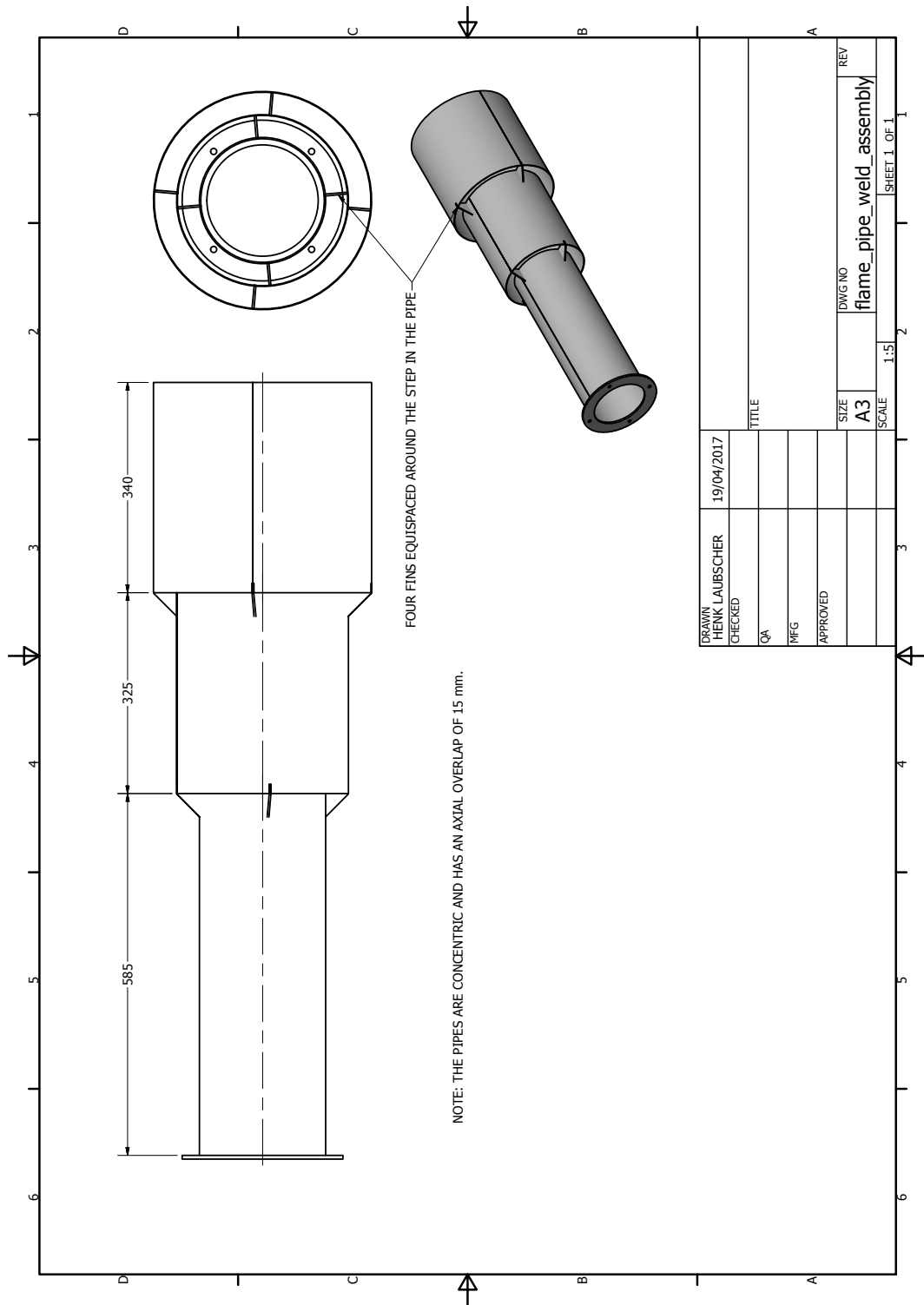


Figure D.4: Air cooled flame containing nozzle layout

D.5 Fan Specifications

CFW INDUSTRIES (Pty) Ltd			OUR REF: B135-063		
Head Office Cape Town			PROJECT: Stellenbosch University		
Tel: +27 21 931 8331			COMPANY: Henk Laubscher		
Fax: +27 21 931 3165			ATTENTION:		
email: sales@cfw.co.za			DATE: 13.11.2015		
CFW FANS <small>LAUBSCHER FAN TECHNOLOGY</small>			PAGE 1		
Fan Reference	A				
Application	CLEAN AIR				
Quantity	1				
Volume (m³/sec)	0.5				
Static pressure (Pa) (1.2kg/m³)	5500				
Static pressure (Pa) (@ site @ temp)	5500				
Altitude (m)	0				
Temperature (°C)	20				
Environment	INDUSTRIAL				
Density (kg/m³)	1.2				
Fan size	630 (1.0)				
Fan type	TBC-CZ				
Class	1				
RPM	2875				
Drive	DIRECT				
Sound level (dBA @ 3m)	78.3				
Discharge velocity (m/s)	26.4				
Efficiency (%) (Total)	76.2				
BkW @site at operating temp	4.18				
BkW @ site @20°C	4.18				
BkW (1.2kg/m³) STP	4.18				
Motor (kW / poles / v /PHz / Hz / IP)	ACTOM 5.5/2/400/3/50/55				
Motor mounting	FOOT				
Motor enclosure	CAST IRON				
FAN FINISH	CFW BLUE ENAMEL				
Total Price (each) (ex works Cape Town)	R 24 465				
EXTRAS					
Inlet Screen	R 389				
Attenuator	R 788				
<p>Price includes: Bare fan, motor and inlet-flange. Delivery: 4 working weeks from date of order (subject to final technical and drawing approval being received within 3 days of submission to client). Validity: 30 days. Prices exclude Value Added Tax. Our standard conditions of sale apply, a copy of which is available upon request.</p>					
			Representative: J. Robertson		

Figure D.5: Fan specification sheet with rated values

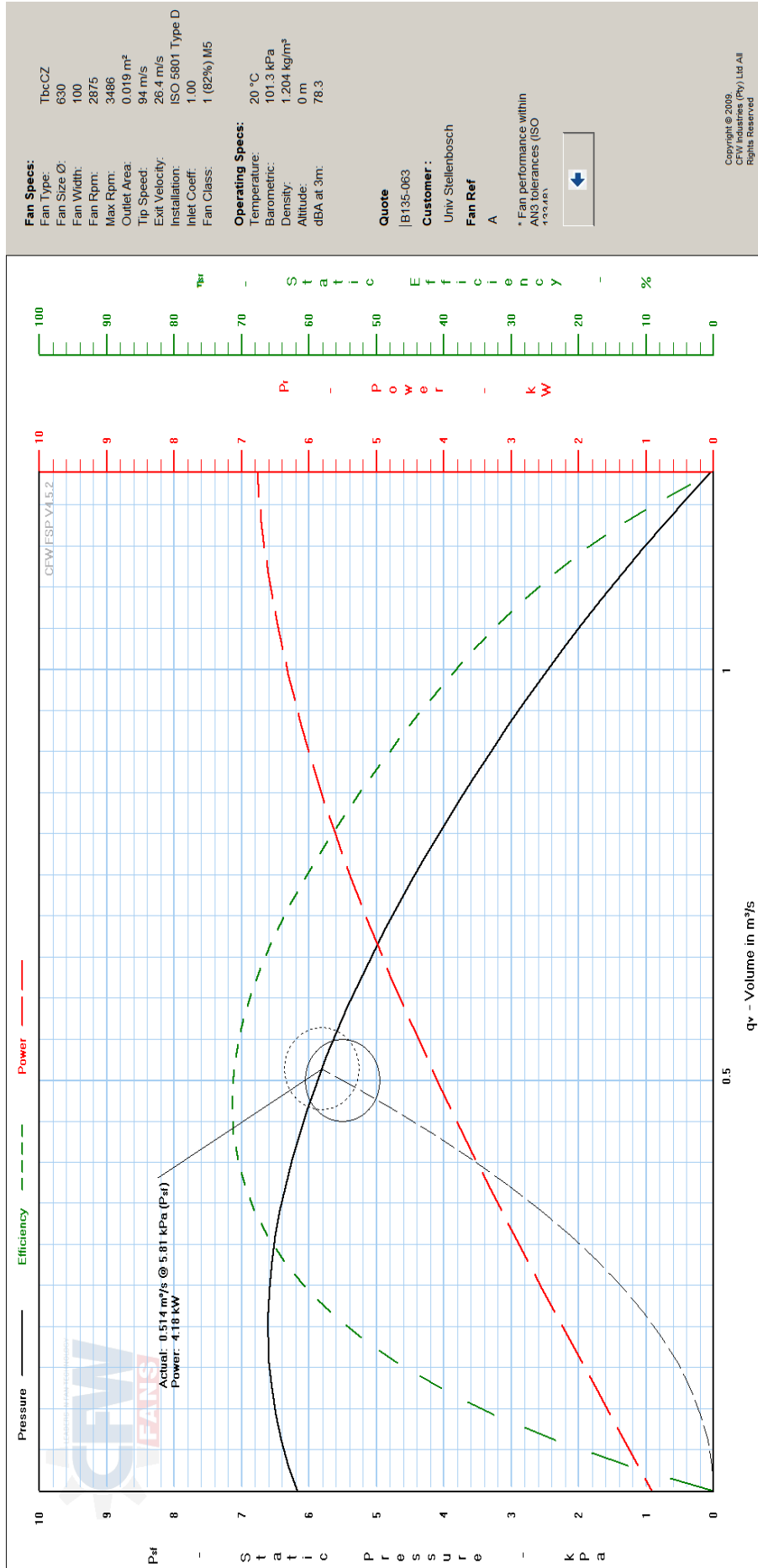


Figure D.6: Fan performance curve

Appendix E

Pressure Transducer Calibration

E.1 Calibration Procedure

Calibration of the pressure transducer used in this project was done by making use of a Betz micromanometer (ACIN, 2016). Six different pressure points in the pressure measurement range were selected and data at each pressure reading was recorded. The high pressure side of both the Betz micromanometer and the Endress and Hauser PMD75 pressure transducer was connected in parallel to measure the same pressure. An output signal in mADC was recorded with an Agilent 34972A LXI data acquisition switch unit. The details on the name plate of the pressure transducer can be seen in Figure E.1.

The zero reading of the pressure transducer when no pressure difference was measured was recorded and it was ensured that the same zero reading is displayed on the face of the pressure transducer during experimental testing. Due to the experimental setup located far away from Stellenbosch University, calibration could not be done on site because of logistical reasons of transporting the Betz micromanometer.

E.2 Calibration Results

A set of pressure readings with the corresponding output signals were used to create a pressure—DC-current curve to derive a polynomial function. A scatter plot of the measured points are given in Figure E.2 and a linear trend line fitted on the scattered data produce the linear function with an R^2 value of 0.9999. The y in the equation E.1 is the variable for the DC output signal in mA and the P is the measured pressure relative to ambient pressure in Pa.

$$P = 193.34y - 848.18 \quad (\text{E.1})$$

The function derived from the calibration data is used in the calculation of the pressure difference from the measured mADC output signal during ex-



Figure E.1: Name plate of the Endress and Hauser pressure transducer

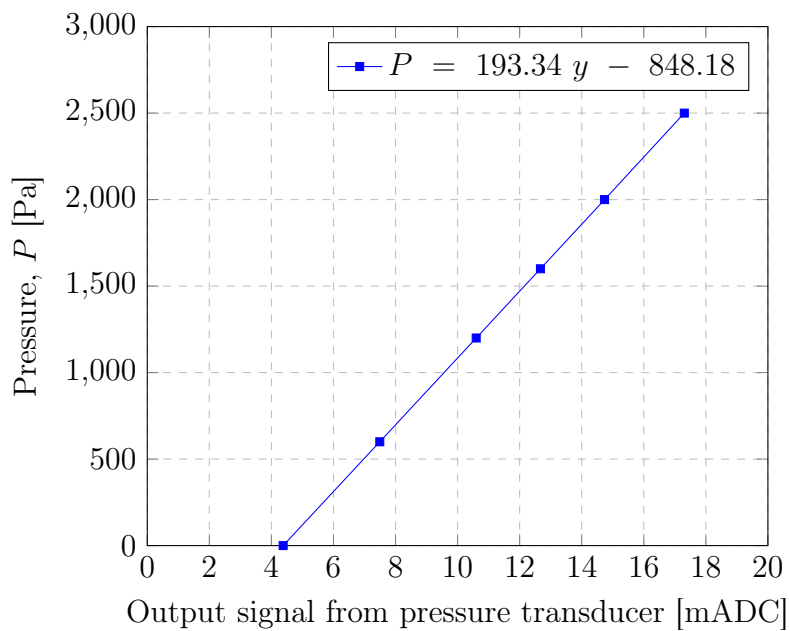


Figure E.2: Calibration curve showing the pressure for the corresponding mADC reading

perimental testing. The pressure difference measured at the throat of the bellmouth is used to calculate the mass flow rate through the system.

Appendix F

Computational Fluid Dynamics

F.1 Introduction to Numerical Analysis

Computational fluid dynamics (CFD) was used to simulate the preliminary performance of the thermal energy storage facility. The preliminary results, produced with the available software from the Fluent package of ANSYS, was used as a design tool for the layout of the experimental design. Parameters such as the temperature distribution, pressure drop and flow characteristics of the specific geometry gave an indication of the material selection for the design.

All CFD analyses for flow in a porous media is done with ANSYS Fluent. Two basic methods of defining the flow through a porous medium were investigated in this study. One method makes use of the built-in model that computes the flow in cells with specified porous properties. The second method takes the actual geometry into account of the porous media and is computationally intensive. Therefore, the built-in porous model option was investigated further in this study to produce numerical simulation results.

The built-in porous model has the option to calculate the computational domain with either a thermal equilibrium model or a thermal non-equilibrium model. The thermal equilibrium model can be used when the assumption is valid that the solid temperature and the fluid temperature in the porous model are the same. In a steady state situation, the particle and the fluid temperature will eventually reach the same temperature, but for the transient solution, the temperature difference between the particle temperature and the fluid temperature is the main driver for heat transfer. With no temperature difference, there will be no heat transfer from the fluid to the particles or from the particles to the fluid.

A thermal non-equilibrium model is more applicable in the case where there must be a distinction between the particle temperature and the fluid temperature. Heat transfer coefficient properties in a porous CFD model are based on the temperature difference between the solid and the fluid. Results from the

Table F.1: Physical properties of packed bed of rocks

Rock Properties (Hornfels, Schist)	Value	Units	Symbol
Density	2700	kg/m ³	ρ_r
Thermal conductivity	1.5	W/m·K	k_r
Heat Capacity	820	J/kg·K	$c_{p,r}$
Void fraction	0.45	–	ε
Volume equivalent diameter	40	mm	D_v
Natural angle of repose (degrees)	38	°	θ
Average size	53	mm	S

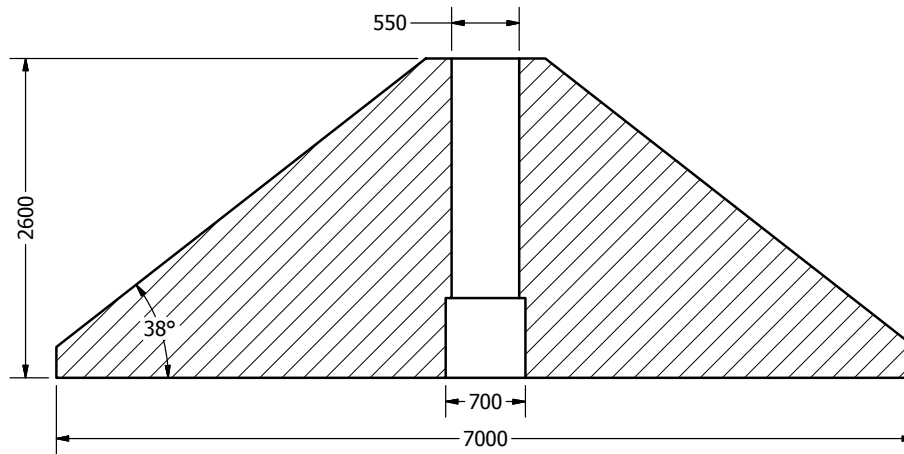


Figure F.1: Dimensions of the porous medium geometry

numerical model that is based on correlations from Allen *et al.* (2015) were used for the specification of a user defined heat transfer function in the CFD model. Numerical correlations are covered in more detail in Chapter 5. A dual cell approach is followed for meshing the computational domain. The thermal non-equilibrium model creates an additional mesh to enable the simulation software to store the temperatures of the particles in a different mesh for calculation in the time and space domain. Calculation for the constants and parameters used in the CFD simulation model are all done by using the actual particle characteristics that are listed in Table F.1 (Allen *et al.*, 2015).

F.2 Process of Numerical Simulation

F.2.1 Geometry Definition

The three dimensional geometry as depicted in Figure F.2 describes the physical layout of the packed rock bed. The computational domain is defined by a solid 30° section of the conical shape as seen in Figure F.3. Due to the axis symmetric properties of a conical shape and the assumption that the pac-

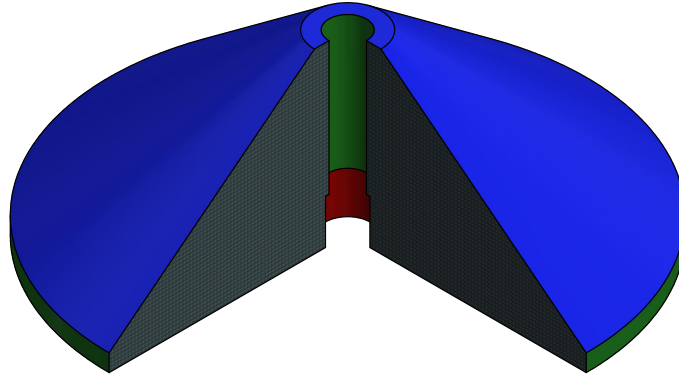


Figure F.2: Geometry of the rock conical rock pile with a cut-out to expose the detail

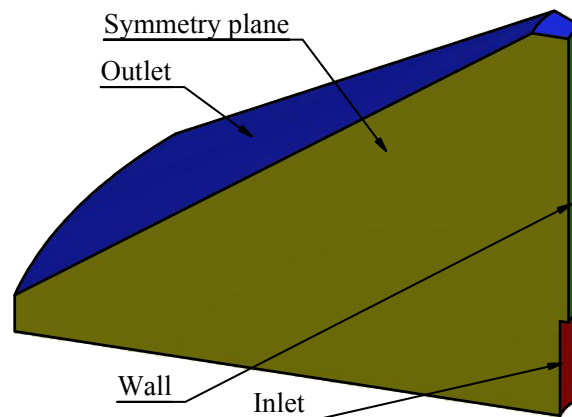


Figure F.3: Computational domain section showing a 30 vector of the real geometry

ked bed medium is isotropic, it is sufficient to simulate a section of the real packed bed geometry. Symmetry planes are defined for the area where the computational domain is sectioned.

Figure F.1 contains the dimensions of the complete packed bed geometry. Descriptive geometry of the computational domain is created as a CAD model and exported to the Fluent package of ANSYS Workbench 17. The inlet plane is marked in red for the charging cycle while the outlet is marked in blue. Areas that are marked in green represent the wall boundary conditions. Inlet and outlet boundary conditions change places when the system is in discharging mode. Axis-symmetric behaviour of the flow characterisation can be identified by using a 3 D geometry.

Table F.2: Mesh statistics for simulation

Computational cell properties	Value
Number of nodes	6088
Number of elements	4907
Type of elements	hexahedral

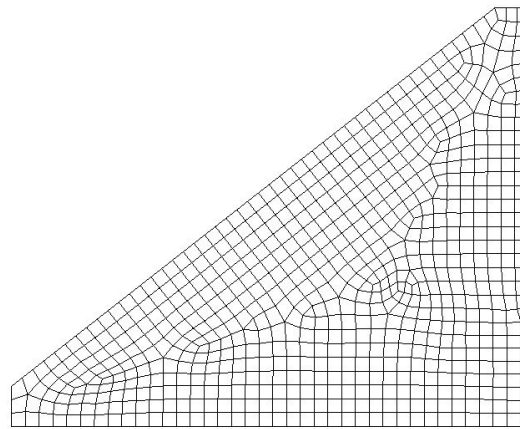


Figure F.4: Cross-sectional plane showing meshing in the computational domain

F.2.2 Mesh

The meshing of the computational domain is done by making use of a structured three dimensional (3 D) mesh. A plane cross-section of the 3 D mesh is presented in Figure F.4. Three dimensional elements are used to mesh the 3 D volume by applying a hexahedral geometry to all the computational cells. Statistics of the meshing is listed in Table F.2

F.2.3 Solution Setup

The solution setup for the CFD model is set up in a way to replicate reality in the best practical way possible. In the general setup section, the energy model should be selected as 'on' and the viscous model is chosen to be the k- ϵ with standard wall function. Materials are defined for the porous media model, air with ideal gas properties and rock as the solid material. Properties for air are defined as temperature dependent parameters in a polynomial function. Rock properties and general parameters for defining the porous medium is given in Table F.1. Control of the solution was done by using a fixed time stepping method. A time step of 120 s was iteratively identified to give good results and minimise the calculating time for the transient solution.

F.2.4 Cell Zone Conditions

A built-in isotropic function in ANSYS fluent was used for simulating the packed bed thermal energy storage. The porous model is activated in the cell zone conditions setup by ticking the box of porous media. Two direction vectors are given to identify the location and geometry of the computational domain. The option of relative velocity resistance formulation is enabled to specify the resistance terms in the porous media. A viscous resistance coefficient and inertial resistance coefficient are calculated to represent the porous medium flow resistance. The viscous resistance coefficient is given by the inverse of α in equation F.1. Therefore, the viscous resistance coefficient is given by $1/\alpha$. The inertial resistance coefficient, C_2 , is given by equation F.2. Definition of the respective resistance coefficients used in the porous media model in ANSYS are given in the user's guide of ANSYS Fluent (ANSYS, 2013).

A thermal non-equilibrium model is enabled and the interfacial area density is defined by the amount of particle surface area per volume. The interfacial area density is calculated by using an equivalent spherical diameter approximation for the particles in the porous zone. Total surface area of the spherical particles in one cubic meter is calculated. A surface heat transfer coefficient is taken from the calculations done in Chapter 5.

$$\alpha = \frac{D_v^2}{150} \frac{\varepsilon^3}{(1 - \varepsilon)^2} \quad (\text{F.1})$$

$$C_2 = \frac{3.5(1 - \varepsilon)}{D_v} \frac{1}{\varepsilon^3} \quad (\text{F.2})$$

Superficial velocity is enabled in the cell zone conditions. Operating conditions for the numerical model is defined by setting the operating pressure as 101 325 Pa, reference temperature location as zero for all three direction vectors and the ambient temperature as 288.15 K. Gravity is enabled and the negative scalar for gravitational acceleration is entered for the vertical direction vector.

F.2.5 Boundary Conditions

The inlet condition is specified as a mass flow inlet with the air velocity set to be 0.04 kg/s (one 12_{th} of the total geometry requires a 12_{th} of the total mass flow). Air inlet temperature is set to be 915 K. The outlet is specified as a pressure outlet which has a gauge pressure of 0 Pa. The pressure drop through the porous medium is thus calculated relative to the ambient pressure. Boundary conditions for the computational domain are chosen to simulate real life boundary conditions and factors from the environment. Symmetry planes as shown in Figure F.3 are assigned to the planes where the computational domain has interaction with the rest of the packed bed. Axis symmetric properties of the computational domain dictates that there is only flow in a radial

direction outwards from the center therefore, the symmetry plane assumption is valid in this case.

F.3 Porous Media Models

A porous medium is computationally intensive if the actual geometry of the particles or porous medium is investigated on a fine scale including all the minor details. In most cases, it is physically impossible or simply impractical to measure and define the geometry of a rock pile consisting of a non-uniform rock particles. Each particle is unique in geometry and size therefore, an equivalent spherical diameter is defined to quantify the properties of a packed bed consisting of non-uniform particles.

F.3.1 Built-in Porous Model

The built-in porous model in the Fluent package of ANSYS was chosen in this study for simulating the TES system. Due to the complexity of heat transfer and flow simulation in a porous medium, the choice was made to do a simplified CFD simulation on the TES layout as described in this project.

F.3.2 Porous Media Geometry

Another method to do numerical simulation on a porous medium is to define the actual geometry for a group of particles that forms a porous medium. This option was not pursued in this study, as previous work on this topic was conducted for this specific TES layout and showed that discrete CFD models of packed beds had several difficulties to perform. Discrete CFD is computationally more intensive than using the porous model in ANSYS Fluent (Louw, 2014).

F.4 CFD Results

Thermal distribution results from a simulated TES can be seen in the contour temperature profile in Figure F.5. The first results produced with the CFD porous model show that the temperature distribution is affected by buoyancy effects of the rising hot air. A heat plume can be observed in Figure F.5 which shows how the effect of buoyancy from the hot air does have an effect on the heat flow during the charging cycle of the TES. The predicted temperature distribution in the packed rock bed obtained from the CFD simulation is used as a guideline for the design of the operational strategies and the physical layout of the high temperature region in the rock bed. Charging time, identification of high temperature zones and pressure drop over the packed bed in charging

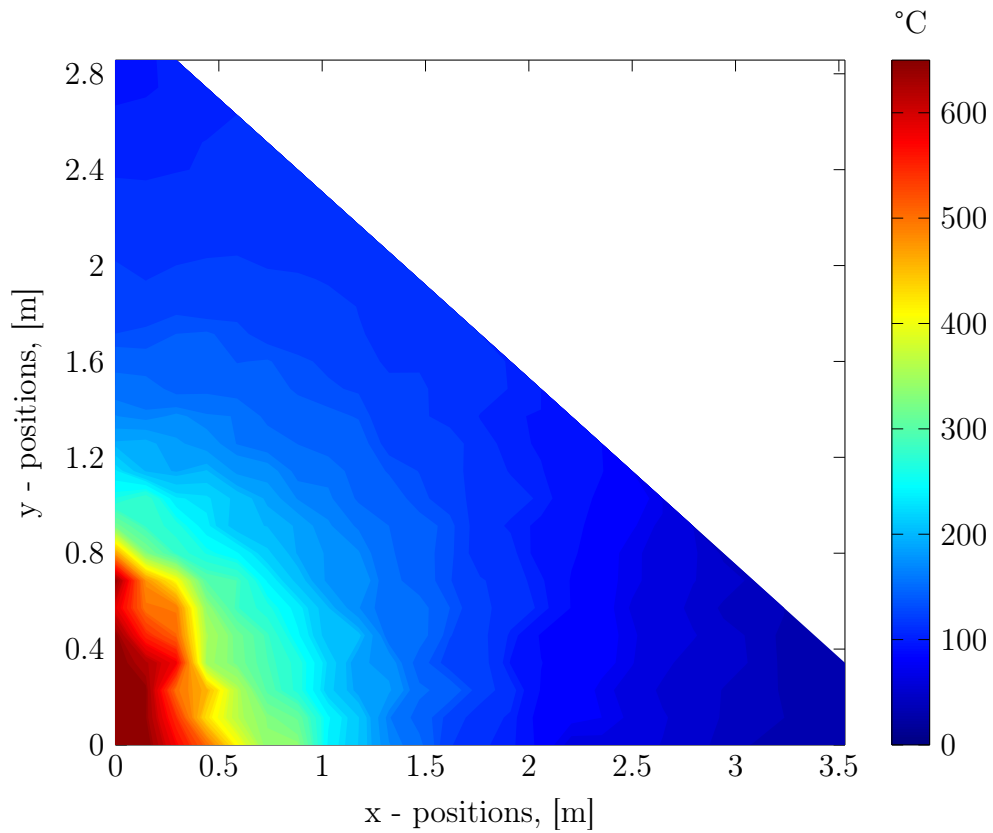


Figure F.5: Temperature distribution of the simulated TES after 4.5 hours of charging (Results reworked in Matlab to have same colour contour scale as the measured temperature distribution results)

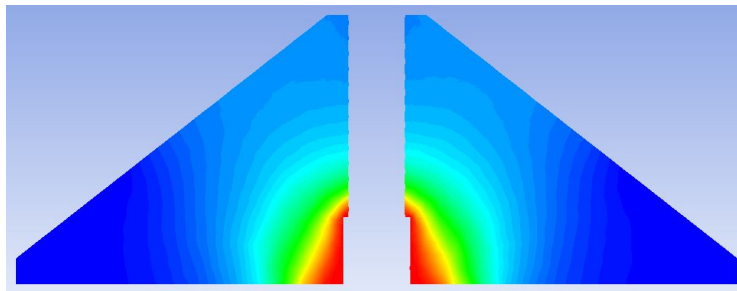


Figure F.6: Temperature distribution of CFD simulated TES results after 4.5 hours of charging

mode are all results from the initial CFD results that was used as a tool in the design specifications of the TES system.

Appendix G

Experimental Facility Capital Expenditure

The expenses listed in Table G.1 are only the material and equipment cost of the TES experimental facility that had been built for this study. No labour expenses for construction of the facility are documented during this study, since all the construction work was supervised and done by Mr H.F. Laubscher and a fellow engineering student.

A virtual cost of construction was calculated by using the total number of man hours. A total of 960 man hours was spent on the construction site at ZAR 250 /hour bringing the total labour cost to ZAR 240 000.

Table G.1: Capital asset items

Asset items	Cost, ZAR
Vaporizer	23 731
Gas burner	43 973
Gas supply line	161 817
Data logging cards	26 745
Thermocouples	20 769
Fan	28 333
Consumable items	
Gas fuel	11 217
Mild steel items	16 218
Stainless steel items	22 232
Rocks	19 330
Stacking of the rocks	7 570
Electricity supply	17 255
Control system	9 423
Tarpaulin cover	8 941
Diverse consumables	10 642
Insulation	33 379
Labour (virtual)	240 000
Total (actual)	461 575
Total (virtual)	701 575

List of References

- ACIN (2016). Betz Micromanometer Manual. <http://www.acin.nl/wp-content/uploads/2016/06/Betz-manual-NL-EN-web.pdf>. Accessed: 2017-09-05.
- Agilent Technologies (2012). Data Acquisition Switch Unit. User's guide, Loveland.
- Airlight Energy (2014). Airlight Energy. <http://www.airlightenergy.com/ait-baha-csp-pilot-plant/>. Accessed: 2016-10-10.
- Allen, K., Von Backström, T.W., Joubert, E. and Gauché, P. (2016). Rock bed thermal storage: Concepts and costs. In: *SolarPACES*, vol. 1734. ISBN 9780735413863. ISSN 15517616.
- Allen, K.G. (2014). *Rock bed thermal storage for concentrating solar power plants*. PhD Dissertation, Stellenbosch University.
- Allen, K.G., Von Backström, T.W. and Kröger, D.G. (2013). Packed bed pressure drop dependence on particle shape, size distribution, packing arrangement and roughness. *Powder Technology*, vol. 246, no. September 2013, pp. 590–600.
- Allen, K.G., Von Backström, T.W. and Kröger, D.G. (2014). Packed rock bed thermal storage in power plants : design considerations. In: *Energy Procedia*, vol. 49, pp. 666–675. Elsevier B.V. ISBN 2721808427. ISSN 1876-6102.
Available at: <http://dx.doi.org/10.1016/j.egypro.2014.03.072>
- Allen, K.G., Von Backström, T.W. and Kröger, D.G. (2015). Rock bed pressure drop and heat transfer : Simple design correlations. *Solar Energy*, vol. 115, pp. 525–536.
- ANSYS (2013). ANSYS FLUENT User's Guide. *ANSYS FLUENT User's Guide*, vol. 15317, no. November 2013, pp. 1–2498. ISSN 19454589. arXiv: 1011.1669v3.
Available at: http://cdlab2.fluid.tuwien.ac.at/LEHRE/TURB/Fluent.Inc/v140/flu{ }_ug.pdf

- Antonio, J., Villaverde, T. and González, I.H. (2012). Behaviour of Structural Carbon Steel at High Temperatures. *Journal of Materials Science and Engineering A*, vol. 2, no. 7, pp. 501–510.
- Bejan, A. (1996). Method of entropy generation minimization, or modeling and optimization based on combined heat transfer and thermodynamics. *Elsevier*, vol. 35, pp. 637–646.
- Bradshaw, R. and Goods, S. (2009). Accelerated Corrosion Testing of a Nickel-Based Alloy in a Molten Salt. Tech. Rep., Sandia National Laboratories, Livermore.
- Cengel, Y.A. and Boles, M.A. (2011). *Thermodynamics an engineering approach*. 7th edn. McGraw-Hill, New York. ISBN 9780073529325.
- Cengel, Y.A. and Cimbala, J.M. (2010). *Fluid mechanics fundamentals and applications*. 2nd edn. McGraw-Hill. ISBN 978-007-128421-9.
- Columbus Stainless (2007). Technical data 3CR12 3CR12L CS410S. Technical data, Middelburg.
- Columbus Stainless (2017). Standard Ferritic Stainless Steels. <https://www.columbus.co.za/files/technical/Ferritics{ }Standard.pdf>.
- DiOrio, N., Dobos, A. and Janzou, S. (2015). Economic Analysis Case Studies of Battery Energy Storage with SAM. Tech. Rep. November, NREL, Denver Colorado.
- Duffie, J.A. and Beckman, W.A. (1991 apr). *Solar Engineering of Thermal Processes*. 2nd edn. John Wiley & Sons, Inc., Hoboken, NJ, USA. ISBN 9781118671603.
Available at: <http://doi.wiley.com/10.1002/9781118671603>
- Figliola, R.S. and Beasley, D.E. (2006). *Theory and Design for Mechanical Measurements*. 4th edn. John Wiley & Sons, Inc., Phoenix. ISBN 0-471-44593-2.
- Gauché, P. and Louw, A.D.R. (2014). Cone rock bed thermal energy storage system. South african provisional patent, 2014/03555, Stellenbosch University.
Available at: <http://www.innovus.co.za/assets/files/TechnologiesEnglish/CONEROCKBEDTHERMALENERGYSTORAGESYSTEM.pdf>
- Hänchen, M., Brückner, S. and Steinfeld, A. (2011). High-temperature thermal storage using a packed bed of rocks — Heat transfer analysis and experimental validation. *Applied Thermal Engineering*, vol. 31, no. 10, pp. 1798–1806. ISSN 13594311.

- Hughes, P.J. (1975). *The Design and Predicted Performance of Arlington House*. Ph.D. thesis, University of Wisconsin-Madison.
- Hughes, P.J., Klein, S.A. and Close, D.J. (1976). Packed Bed Thermal Storage Models for Solar Air Heating and Cooling Systems. *Journal of Heat Transfer*, vol. 98, no. 2, pp. 336–338. ISSN 00221481.
- Incropera, F., DeWitt, D., Bergman, T. and Lavine, A. (2007). *Introduction to heat transfer*. 5th edn. John Wiley & Sons, Inc., Hoboken, NJ, USA.
- Kolb, G.J., Ho, C.K., Mancini, T.R. and Gary, J.A. (2011). Power Tower Technology Roadmap and Cost Reduction Plan. Tech. Rep. April, Sandia National Laboratories.
- Kröger, D.G. (2012). SUNSPOT Cycle.
Available at: <http://sterg.sun.ac.za/wp-content/uploads/2011/05/SUNSPOT-2.pdf>
- Kröger, D.G. (2013). Packed Rock Bed Thermal Storage. South african provisional patent, 2013/03068, Stellenbosch University.
- Louw, A.D.R. (2014). *Discrete and porous computational fluid dynamics modelling of an air-rock bed thermal energy storage system*. PhD Dissertation, Stellenbosch University.
Available at: <http://hdl.handle.net/10019.1/86233>
- Nel, R.G. (2013). *Discrete Element Modelling of packed rock beds for thermal storage applications*. Masters Thesis, Stellenbosch University.
- Schumann, T. (1929). Heat transfer: A liquid flowing through a porous prism. *Journal of the Franklin Institute*, vol. 208, no. 3, pp. 405–416. ISSN 00160032.
- Shinko (2005). Digital Indicating Controller ACS-13A. Catalogue, Shinko Technos co., ltd., Osaka.
- Solargis (2011). Solargis-Africa-and-Middle-East-DNI-solar-resource-map.
Available at: <http://solargis.com/assets/graphic/free-map/DNI/Solargis-Africa-and-Middle-East-DNI-solar-resource-map-en.png>
- Solargis (2013). DNI-Solar-map-World.
Available at: <http://solargis.com/products/maps-and-gis-data/free/download/world>
- Zanganeh, G., Pedretti, A., Zavattoni, S., Barbato, M. and Steinfeld, A. (2012). Packed-bed thermal storage for concentrated solar power - Pilot-scale demonstration and industrial-scale design. *Solar Energy*, vol. 86, no. 10, pp. 3084–3098. ISSN 0038092X.
Available at: <http://dx.doi.org/10.1016/j.solener.2012.07.019>

Zavattoni, S.A., Barbato, M.C., Pedretti, A. and Zanganeh, G. (2015). Single-tank TES System - Transient Evaluation of Thermal Stratification According to the Second-law of Thermodynamics. *Energy Procedia*, vol. 69, pp. 1068–1077. ISSN 18766102.

Available at: <http://dx.doi.org/10.1016/j.egypro.2015.03.213>